Preserving Texture Boundaries for
SAR Sea Ice Segmentation

by

Rishi Jobanputra

A thesis

presented to the University of Waterloo

in fulfillment of the

thesis requirement for the degree of

Master of Applied Science

in

Systems Design Engineering

Waterloo, Ontario, Canada, 2004

I hereby declare that I am the sole author of this thesis. This is a true copy of the thesis, including any required final revisions, as accepted by my examiners.

I understand that my thesis may be made electronically available to the public.

Abstract

Texture analysis has been used extensively in the computer–assisted interpretation of SAR sea ice imagery. Provision of maps which distinguish relevant ice types is significant for monitoring global warming and ship navigation. Due to the abundance of SAR imagery available, there exists a need to develop an automated approach for SAR sea ice interpretation.

Grey level co-occurrence probability ($GLCP$) texture features are very popular for SAR sea ice classification. Although these features are used extensively in the literature, they have a tendency to erode and misclassify texture boundaries. Proposed is an advancement to the $GLCP$ method which will preserve texture boundaries during image segmentation. This method exploits the relationship a pixel has with its closest neighbors and weights the texture measurement accordingly. These texture features are referred to as $WGLCP$ (weighted $GLCP$) texture features.

In this research, the $WGLCP$ and $GLCP$ feature sets are compared in terms of boundary preservation, unsupervised segmentation ability, robustness to increasing boundary density and computation time. The $WGLCP$ method outperforms the $GLCP$ method in all aspects except for computation time, where it suffers. From the comparative analysis, an inconsistency with the $GLCP$ correlation statistic was observed, which motivated an investigative study into using this statistic for image segmentation. As the overall goal of the thesis is to improve SAR sea ice segmentation accuracy, the concepts developed from the study are applied to the image segmentation problem. The results indicate that for images with high contrast boundaries, the $GLCP$ correlation statistical feature decreases segmentation accuracy. When comparing $WGLCP$ and $GLCP$ features for segmentation, the $WGLCP$ features provide higher segmentation accuracy.

Acknowledgements

Firstly, I would like to thank my family (mom, dad and Lina). My success thus far is a reflection of their support and encouragement throughout the years.

I would also like to show appreciation to my supervisors, Professor David A. Clausi and Professor Hamid R. Tizhoosh, their advice and support made this thesis possible. Professor Clausi's efforts and positive criticism have turned otherwise acceptable work to excellent caliber. As well, Professor Tizhoosh's insights and vast knowledge from course lectures have provided a significant impact.

I would also like to express gratitude to my friends and colleagues that helped encourage and challenge me throughout this degree. Special acknowledgements are extended to the VIP lab (past and present), the Systems Design Engineering faculty/staff/students and Priyesh Shukla for their contributions.

Lastly, I would like to thank Soniya Patel. Her patience and unconditional love was motivational in completing this degree.

Table of Contents

List of Tables

List of Figures

Chapter 1

Introduction

1.1 General

The analysis of remotely sensed data remains an important application in the field of computer vision. Remotely sensed images contain an extensive amount of information about objects within a scene (*e.g.* brightness, shape, size, spatial proximity). The role of computer vision is to use this information to segment the relevant objects within an image. Although easily segmented by the human observer, there exists no robust automated machine approach that can consistently separate relevant classes in synthetic aperture radar (SAR) sea ice imagery.

Texture has been used extensively in the interpretation of SAR imagery [35]. There have been many different mathematical representations which define texture, however, there exists no universal definition for texture. Texture measures are used to characterize a particular relationship between a pixel and its neighbors. Interpretation of these texture measures can be applied to the image segmentation problem.

In general, the texture image segmentation problem can be divided into two steps. First, appropriate textural features for each pixel must be calculated. This is called *feature extraction.*

Next, pixels with similar features are grouped together according to some discriminating (or similarity) function. This is referred to as *classification*. Improving the feature extraction to have distinguishable features will increase class separability in the feature space. As well, a clustering methodology that consistently and accurately separates relevant classes within an image is desirable. This thesis will focus on using texture methods to segment relevant ice types in SAR imagery while concentrating on the preservation of texture boundaries.

1.2 Thesis Summary

In this thesis, many issues involving the use of texture features will be discussed. A method for preserving texture boundaries will be presented and analyzed. The following outline will be used:

- Chapter 2 - Background

  This chapter will discuss the motivation for monitoring sea ice and the relevance of using the SAR platform for remotely sensing sea ice. A description of the physical properties of sea ice and the role of texture for segmenting relevant ice types is explained. The chapter concludes by discussing the challenges in SAR sea ice interpretation.

- Chapter 3 - Statistical Texture Analysis

  Chapter 3 will present a description of current techniques used to generate texture features and compare them. A detailed description of the *GLCP* method for texture image segmentation is given. The chapter ends by discussing different segmentation algorithms with focus on k-means clustering.

- Chapter 4 - Proposed Technique: Weighted Co-occurring Texture Features

  This chapter will motivate and present an advancement of the *GLCP* method which will preserve texture boundaries during image segmentation. The method exploits the relation-

ship a pixel has with its closest neighbors and weights the texture measurement accordingly. These texture features will be referred to as *WGLCP* (weighted *GLCP*) texture features.

- Chapter 5 - Experiments and Results Analysis

  Chapter 5 begins by performing a comparative study between the *GLCP* and *WGLCP* texture features with respect to boundary preservation, image segmentation ability, robustness to increasing boundary density and computation time. From the comparative study, a discrepancy in the *GLCP* correlation statistical feature is observed which leads to an investigative study of the *GLCP* statistics. The section concludes by applying the concepts learnt for improved image segmentation.

- Chapter 6 - Conclusion

  The thesis concludes by elaborating the results, stating some of the strengths and limitations of this work, and providing direction for future work in SAR sea ice segmentation.

Chapter 2

Background

This chapter will first present some reasons for monitoring sea ice and how SAR platforms can aid in this process. Some background knowledge of the SAR system and its properties is presented followed by a discussion on the interactions of microwaves with the sea ice surface. Literature review of texture definitions, from an image processing perspective follows. This chapter concludes with some of the inherent challenges involved with SAR sea ice segmentation.

2.1   Motivation

Monitoring of the cryosphere remains a challenge in scientific and operational communities. The cryosphere is defined as the aspect of the earth's climate system consisting of the ice masses and snow deposits. This includes sea ice, ice sheets, lake and river ice, ice caps, glaciers and snow cover [34]. The cryosphere has a fundamental contribution to the global climate system by moderating transfers of energy, moisture and gas flux with the land, atmosphere and oceans. Within Canada and the Northern hemisphere, sea ice covers between approximately 7.5 and 15.0 million square kilometres of the Arctic Ocean with an average thickness of about three metres

[34]. This extensive area is efficient at regulating the global climate by preventing the relatively warm ocean water from heating the atmosphere. As well, sea ice is fairly efficient at reflecting sunlight back into space.

Monitoring of cryospheric activity such as ice floes is necessary to address key scientific questions such as the effect of glacier melt on sea level rise, and for improved representation of climatological models. Also in Canada, there are continuing operational obligations for monitoring sea ice in the east coast, the Gulf of St. Lawrence, all of Hudson Bay and the Canadian Arctic Archipelago [39]. Daily information regarding sea ice patterns is needed for operational decision making (*e.g.* transportation, construction, mining, offshore oil exploration, recreation).

The study and monitoring of sea ice in the cryosphere is difficult and challenging for several reasons. For instance, the Arctic is a sizable and isolated region, making ground monitoring of ice floes a hazardous and impractical task. Within areas such as the St. Lawrence seaway, ice floe information should be daily to navigate ship and ice breaker movements [5]. Obviously, this information can not be acquired through ground measurements. A high–resolution, real–time remote sensing system is needed to capture this information in diverse lighting and weather conditions. Synthetic aperture radar (SAR) meets the requirements of such a system. SAR uses active microwave sensing which is capable of day-night, all weather atmospheric penetration in virtually all conditions [15]. As well, SAR aerial and satellite platforms are capable of regularly capturing information at sufficiently adequate resolutions for the purposes of sea ice discrimination.

Ice investigation continues to this day and is one of the major commercial uses of SAR technology. As SAR research is progressing, platforms are becoming better calibrated, having higher resolution, and are becoming an integral part of sea ice research. With more powerful SAR platforms being deployed, there will be an unprecedented volume of imagery. This large amount of SAR data present could remain unused unless a method for interpreting these images is improved. Computer-aided methods for segmenting sea ice images is a necessary research area

and is the objective of this thesis.

2.2   Introduction to SAR Platforms

Remote sensing is concerned with collecting information about a target without being in physical contact with the object [21]. Both passive and active remote sensing systems are available for imaging. Passive sensors, such as thermal IR (infrared) and visible band cameras, detect electromagnetic energy at certain wavelengths which are reflected or radiated by the target or external energy sources. Active sensors, such as a radar (meaning *radio detection and ranging*), send and receive its own energy.

Most imaging radars operate in the microwave bands of the electromagnetic spectrum, with wavelengths varying from a few centimeters to millimeters in wavelength. The radar system "illuminates" the environment with electromagnetic energy, detects the backscatter energy returning from the target, and interprets it as an image [40]. Figure 2.1 shows the properties of side-looking radar antennas which are mounted on moving platforms (*e.g.* aircraft and satellite). These systems direct their beam to the side of the platform in a direction normal to the flight path and parallel to the horizontal plane of the Earth. This is known as the look direction of the radar. These imaging radars are not affected by lighting and weather conditions, thus, provide day-night, all-weather imaging. Also, as with passive systems, these systems can control their look direction as to enhance the target's features when imaging.

A real aperture radar system operates with a long (about 5-6 meters) antenna [21]. This type produces a beam of noncoherent pulses and uses its antenna length to obtain the desired resolution. The resolution in the azimuth (flight direction) is a function of the ratio of the wavelength to the antenna size [15]. To achieve a high resolution, a short wavelength or an antenna with an unacceptably long physical length must be used. The development of SAR
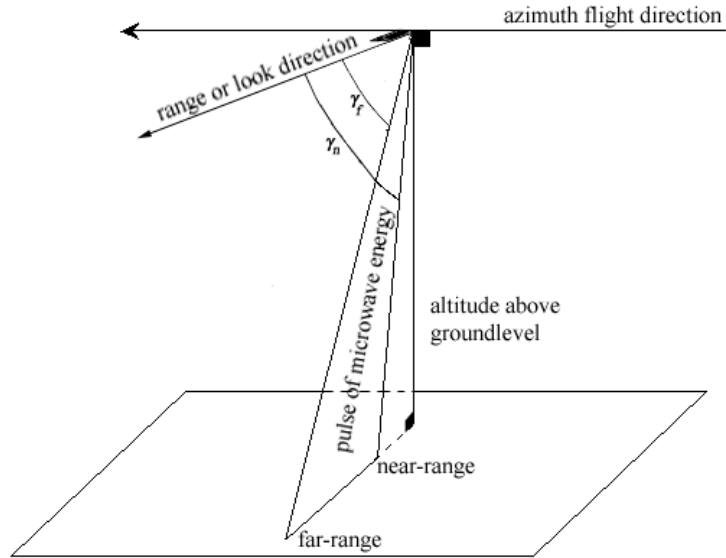
Figure 2.1: Geometric characteristics of a radar image acquired by side-looking radar [40].

alleviated this constraint by synthesizing the effect of a very long antenna using the Doppler history created by the relative velocity between the platform and the ground [5].

As outlined by Sabins in [31], there are two aspects that contribute to the appearance of SAR images: radar system properties and terrain properties. Factors such as wavelength, polarization and spatial resolution determine the radar properties. Terrain properties are defined by their dielectric property, surface roughness and feature orientation.

The wavelength bands used to capture SAR sea ice imagery typically from 1 cm (*e.g.* K-band) up to 30 cm (*e.g.* L-band). Longer wavelengths are attractive because they have higher penetration through objects on the Earth, but will have a lower resolution. Another important SAR system parameter is the polarization of the transmitted and received signals. Generally, the signal is transmitted and received in either horizontal (H) or vertical (V) planes. Considering the sending and receiving directions together, there are four kinds of radar images: HH, VV, HV, VH – the first letter represents the signal transmission and the second letter refers to the signal

reception. Using the image's polarization to aid in segmentation is a relatively new research area that is still under investigation by many scientists. This research area will progress as new SAR satellite platforms (*e.g.* Envisat, Radarsat-2) are being equipped to operate using multiple polarizations.

The spatial resolution of a SAR image is determined by the range and azimuth resolutions of the radar respectively. The range resolution is a function of the radar pulse length and the depression angle (γ), as illustrated in Figure 2.1. The equation for range resolution is:

$$SAR_{range} = \frac{c\tau}{2\cos\gamma} \tag{2.1}$$

where c is the speed of light and τ is the pulse length. Equation 2.1 confirms that the range resolution decreases with the depression angle (γ), that is, the range resolution for a given SAR image will vary across the swath of the image. This problem is partially corrected for using SAR image preprocessing techniques. The azimuth resolution of SAR is:

$$SAR_{azimuth} = N(\frac{D}{2}) \tag{2.2}$$

where D is the antenna length and N is the number of looks. The number of looks (N) refers to the number of times a scene is sampled and averaged. This technique is employed to increase the signal–to–noise ratio (SNR) of the speckle noise caused by the coherent nature of the SAR platform.

Terrain properties affect the backscatter return of the SAR signal. Depending on the properties of the measured surface, the backscatter is a combination of the reflection, scatter and attenuation of the incident signal. The dielectric constant of a material is a dominant factor in determining backscatter. The dielectric constant of an object dramatically increases with its moisture content, resulting in higher scatter. With respect to sea ice, different types will have varying dielectric constants, which can be used to help identify different ice types.

The radar backscatter is also highly dependent on the surface roughness of the terrain. The Rayleigh criterion indicates whether a surface is considered smooth or rough:

$$h < \frac{\lambda}{8 \sin \gamma} \tag{2.3}$$

where h is the root mean square (rms) height of the surface, λ is the signal wavelength, and γ is still the depression angle. If the Rayleigh criterion holds true, then the surface is considered smooth and will reflect most of the signal, thus appearing dark in the image. Similar to Equation 2.1 for range resolution, Equation 2.3 indicates that the backscatter characteristics will vary across the image swath. This will cause differences in the tone and texture of a homogenous object across the image swath.

The feature orientation with respect to the look direction of the radar also influences the radar signature. Features oriented normal to the look direction are augmented by highlights and shadows. Features oriented parallel to the look direction produce no shadowing artefacts in the image and are preferred for segmentation.

The Radarsat–1 platform [21] was used to capture some of the SAR sea ice images used in this thesis. Radarsat is a highly advanced Canadian Earth observation satellite developed to monitor environmental change. Having many different operating modes, Radarsat provides useful information to scientists in the fields of ice studies, agriculture, coastal monitoring, cartography, forestry and hydrology. The Radarsat–1 images used in this thesis were acquired using ScanSAR wide beam mode. This mode operates in C–band frequency, HH polarization, 50×50 meter resolution that is 2×2 block averaged.

2.3   Properties of Sea Ice

According to the World Meteorological Organization (WMO), ice can be generalized into four main types: *new ice*, *young ice*, *first year ice* and *multi–year ice*. This section provides a brief summary of the different ice types and their interactions with SAR.

New ice is formed at the beginning of winter, and is usually less than 10 cm thick. With continuing frigid temperatures, new ice begins transforming to young ice, which is 10 cm to 30 cm in thickness. Near the end of the winter season, ice sheets will accumulate a depth greater than 30 cm and be categorized as first year ice. During the summer season, ice floes undergo dramatic reductions in size and salinity. First year ice that survives the summer season becomes old or multi-year ice.

As discussed in Section 2.2, the orientation, dielectric constant and surface roughness of a material determines its backscattering properties. With respect to sea ice monitoring, the platform look direction and target orientation are usually fixed, and will not vary among different ice types. The dielectric constant of the ice sheet is heavily dependent on the moisture and salinity of the surface and is extremely important to radar return. The surface roughness within and amongst the different ice types varies significantly, hence, ice floes will appear as different "textures" when viewing SAR imagery.

The composition of young and first year *smooth* ice is relatively saline with a loose structure containing many gas bubbles limiting microwave absorption. As a result, most of the energy is reflected by the surface away from the antenna [33]. Surface topography of first year rough ice is sharp and angular with modest relief. This ice will cause unpredictable scattering. Old ice has a low dielectric constant because it has effectively zero brine content which permits significant penetration of microwave energy into the ice. As well, multi–year floes are distinct from first year ridges because they are weathered and rounded, with very little sign of the original block
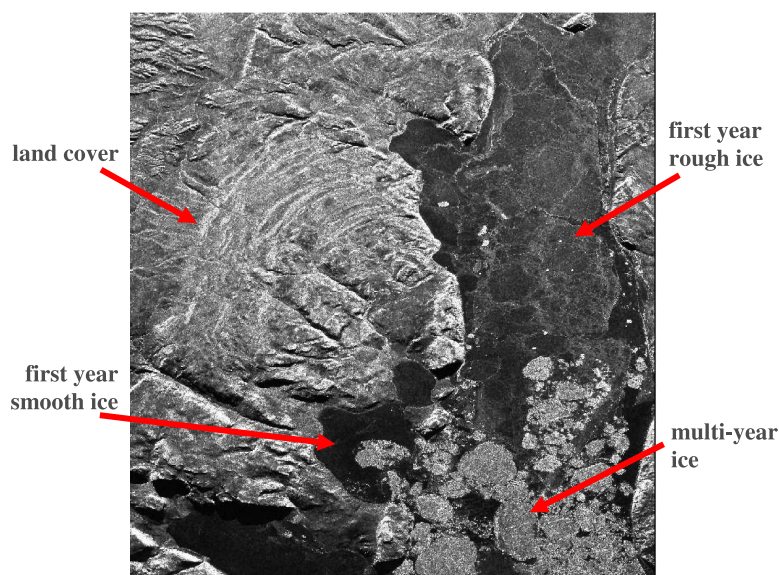
Figure 2.2: SAR image with multiple ice types to illustrate the difference in tone and texture between ice types. Ice types are labelled in the image.

structure present.

Figure 2.2 contains a multi–class SAR sea ice image. The image is extracted from X-band, HH polarization, STAR-1 platform with a six meter resolution. As labelled, this image contains three different ice types and land cover. The first year smooth ice has low variance and dark tone. The first year rough ice has a light grey tone and appears "cloudy". For multi–year ice, it has a bright tone and floes are often rounded and have high frequency "texture" appearance.

2.4 What is Texture and Why Use It?

Most early image segmentation techniques used only the pixel's grey level value as a criteria for discriminating objects within a scene [26]. During the 1970's, the importance of texture features for image segmentation was illustrated [19, 18, 24]. In the original formulation of the grey level co-occurrence probabilities (*GLCP*), developed by Haralick *et al.*[19], texture features

were developed for image classification. Haralick demonstrated more than 80 % classification accuracy for his test sets. To this day, his texture analysis techniques have been referenced in a wide variety of research literature [23].

2.4.1 Texture Interpretations

In the image processing community, there is no universal agreement on the definition for texture. One such definition is by Haralick where he states "Texture is defined as the spatial (statistical) distribution of grey tones [19]." Sabins defines texture as "...the frequency of change and arrangement of tones on an image. Fine, medium, and coarse are some terms used to describe texture [31]." Both of these definitions have similar connotations but differ subtlety in the semantics. According to these definitions, fine textures are those having high frequency grey tone variations while coarse textures are those having low frequency grey tone variations. If there is no variation in grey tone (*i.e.* single grey tone), the object has a very smooth texture.

Figure 2.3 shows two textures from the Brodatz photo album [4] and their corresponding grey level histograms. The first texture is high resolution digital photomicrograph of raiffa, and the second texture is leather. By viewing the histograms, it is apparent that these two images have many common grey levels. When combining these textures to form a bi–partite (*i.e.* two–class) image, the two classes (raiffa and leather) become indistinguishable when using only grey level. This is apparent by viewing the histogram of the bi–partite image. The human observer will use the perceived textural appearance to distinguish these textures. It is apparent that raiffa has a distinct and re-occurring pattern in the horizontal and vertical directions. Leather has a relatively high frequency in the horizontal direction and low frequency in the vertical direction.
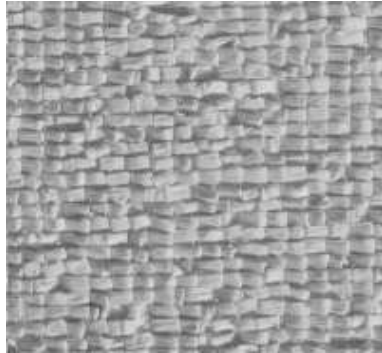
(a) Raiffa (D84)
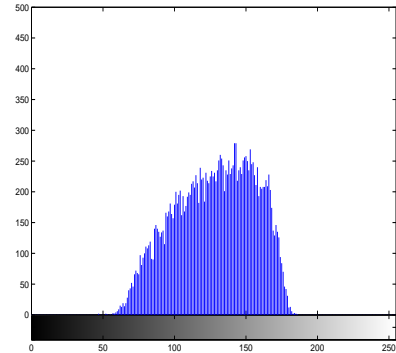
(b) Raiffa Histogram(D84)
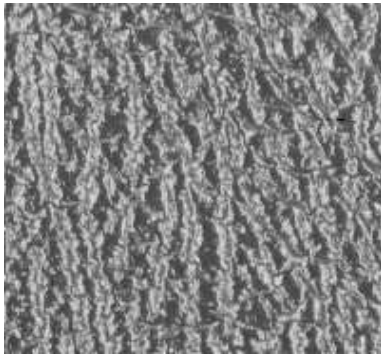
(c) Leather (D2)
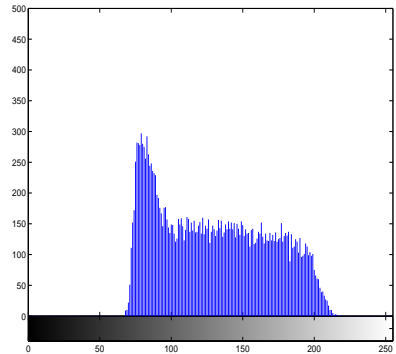
(d) Leather Histogram (D2)
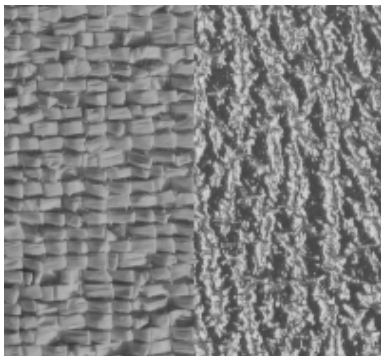
(e) Raiffa–Leather Bi–partite Image
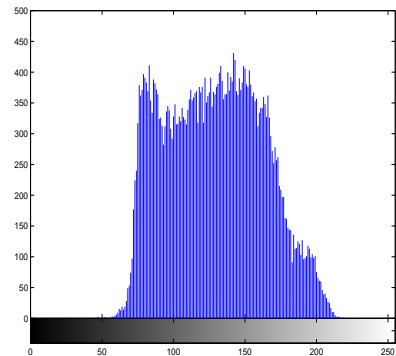
(f) Raiffa–Leather Histogram)

Figure 2.3: Brodatz images of leather and raiffa textures and their corresponding histograms. By viewing the histograms, these textures have many common grey levels, hence, when combining these textures to form a bi–partite image, it becomes difficult to segment the textures from one another. This is evident by viewing the histogram of the combined image.

2.4.2   Texture Methods

When seeking to measure texture, scientists attempt to quantify the nature of the variation of grey levels within an object in an image. An ideal texture measurement should be independent of the object's position, size and shape. There are many different mathematical formulations which measure texture in the literature, Tuceryan and Jain categorize them into four groups: statistical, geometrical, model–based, and signal processing–based [37].

Statistical methods define texture measures as spatial distributions of grey tones for a given area in the image. Statistics are applied to these distributions and used as features for segmentation. Some common statistical methods are autocorrelation features [16, 25], *GLCP* statistics [19], and grey level run lengths [18].

Geometrical texture analysis methods propose that a texture can be characterized as being composed of atomic texture elements or primitives. This method depends on the geometric properties of these texture elements and their orientation with respect to one another. The feature extraction problem is the process of locating the primitives and quantifying their spatial arrangement. An example of geometrical texture analysis is the Voronoi tesselation method proposed by Tuceryan and Jain [36]. As SAR sea ice has no definite primitive structure, this method is not applicable for SAR sea ice segmentation.

Model–based texture analysis is founded on the construction of a model that can be used not only to describe the texture, but also to synthesize the model parameters to capture the perceived qualities of the texture. Markov random fields [6, 11] (MRF) and fractal models [27, 29] are examples of these model–based texture methods, and have been used for SAR sea ice segmentation. Although these methods show promise, they are beyond the scope of this thesis.

Signal processing methods exploit properties of the texture's spectral signature for analysis. The power spectrum, Gabor filter and wavelet transform [5] are common signal processing techniques for extracting texture. Although these methods have been used for SAR sea ice in-

terpretation [5], evidence indicates that these features are sensitive to speckle noise, which is common in SAR imagery. However, recent studies [6] show that signal processing methods are complementary to statistical methods, but will not be discussed further as it is beyond the scope of this thesis.

Of all the methods, the statistical–based *GLCP* technique is the most widely used for SAR sea ice identification in the research literature. Currently, some research efforts are directed towards the fusion of texture features to improve segmentation [6, 8]. Although this area shows promise, this thesis will narrow its focus on modifying the *GLCP* texture features for improving boundary preservation. By directing the research towards modifying *GLCP* features, the enhanced feature set can eventually be used in the fusion methodology to improve segmentation further. A complete and thorough review of the *GLCP* method will be discussed in Chapter 3.

2.5 Challenges of SAR Sea Ice Segmentation

Sea ice is a complicated and ever–changing material. As outlined above, there are many parameters influencing sea ice appearance in SAR platforms. As well, factors such as temperature, wind patterns and salinity contribute to a very complicated appearance of sea ice in SAR imagery. Segmenting SAR sea ice accurately is a very tedious task for the human observer. Listed below is a summary of some of the problems in automated SAR sea ice recognition.

- Different platforms, different resolutions, different polarizations

  As SAR technology is progressing, spatial resolution is improving and features such as polarization are being incorporated. For example, Radarsat-2 will be capable of imaging up to a 3-meter resolution and have cross–polarization. Hence, the SAR data available for remote sensing scientists will be generated from many different platforms, with many different resolutions and polarizations. As a result, the tone and texture of the same ice

type will vary with the platform, which makes it difficult to develop a robust approach that can be applied to any SAR image. The texture variability under different resolutions and platforms has not been well researched.

- Spatial extent of ice floes vary

  The spatial extent of each ice type is different. One ice type may extend several meters where another ice type can stretch several kilometers. As a result, it is difficult to choose parameters for some segmentation algorithms which perform analysis based on neighborhood analysis. In addition, a large ice floe will have a tendency to form leads which fill with open water. As a result, an ice floe can contain a mixture of classes which makes neighborhood analysis difficult.

- Tracing boundaries between ice types

  Even to the human observer, tracing boundaries between ice types is a difficult task. Sea ice types will sometimes appear merged along boundary areas which makes segmentation difficult.

- Sea ice characteristics vary temporally, based on changing weather conditions

  As described in Section 2.3, sea ice is a dynamic material. The melting and accumulation of an ice sheet is dependant on factors such as time, ocean temperature and climate. Due to these dynamic properties of ice, it is difficult to validate the results of a particular segmentation strategy as the objects which are being identified are changing as well.

- Accuracy of SAR imaging

  SAR is convenient for monitoring sea ice, however, there are still some inherent problems with SAR imaging such as speckle noise and geometric distortions. For example, due to the coherent nature of SAR, speckle noise is a predominant artefact in SAR imagery. Although

there exist algorithms to remove speckle noise from an image, they have a tendency to over–smooth textures and erode high contrast boundaries. As well, due to differences in incidence angle across the look direction, the backscatter properties of the same texture will vary slightly across the look direction of the image. Even with the given algorithms to correct for these geometric distortions, this effect will still have an impact on segmentation. In fact, Barber and LeDrew [2] show evidence of higher texture analysis performance in the look direction of an image, which indicates that the SAR platform is directionally biased. Overall, these problems contribute to lower segmentation performance.

Chapter 3

Statistical Texture Analysis

This chapter will begin by reviewing some statistical texture feature extraction techniques and compare their results. Next, a description of *GLCP* method is given. This is followed by a literature review on determining the parameters for a preferred *GLCP* feature set with respect to SAR sea ice segmentation. The chapter concludes by giving an explanation of unsupervised segmentation.

3.1 Statistical Texture Feature Extraction

3.1.1 Methods

There are certain SAR sea ice images where segmentation could be implemented using only the grey level of each pixel. In these situations, higher order texture features are not necessary as they require a significant increase in computation time compared to using just grey level as a feature. Unfortunately, most multi–class SAR sea ice images are more complex in nature, requiring the use of higher order texture features for segmentation.

First order methods are the simplest form of texture analysis [23]. The statistics are based

on individual pixel values with no relationships between pixels. Texture features such as mean, variance, gradient, skewness, *etc.* are extracted from the image [40].

Second order texture features are usually calculated from a transitional relationship matrix which is based on the statistical relationship of a pixel with its neighboring pixels, whereas the first order approach does not take into account the inter–relationship of a pixel and its neighbors. There are three commonly used statistical second order texture methods in the literature [20]: grey level difference (GLD), grey level run length ($GLRL$) and grey level co–occurrence probability ($GLCP$).

The GLD method is an indicator of edges within an image [20] and has proven to increase classification accuracy. Let $f(m, n)$ be the image at row location m and column location n, then for any given displacement value $\eta(\Delta m, \Delta n)$,

$$f_\eta(m, n) = |f(m, n) - f(m + \Delta m, n + \Delta n)| \tag{3.1}$$

where $\Delta m, \Delta n$ are integers. Then a probability density, p_η can be derived from $f_\eta(m, n)$ as follows:

$$p_\eta(i|\eta) = p(f_\eta(m, n) = i) \tag{3.2}$$

If there are k grey levels in the image, p_η will be a k-dimensional vector with its i–*th* element having the probability that $f_\eta(m, n) = i$. For a given separation value, $\eta(\Delta m, \Delta n)$, textures with high p_η close to $i = 0$ are said to be coarse, whereas finer textures will have a more uniform probability distribution. With this methodology, the distribution of p_η indicates the coarseness of a given texture. Statistics such as contrast, entropy, angular second moment, *etc.* can be calculated from p_η.

$GLRL$ statistics indicate neighboring occurrences of identical grey level values in an image [20]. This method uses a $GLRL$ matrix $R(i, j|\theta)$, where each element, $r(i, j|\theta)$, stores the number

of occurrences of a particular grey level i of a specified run length j along orientation θ. With this methodology, coarser textures will have longer run lengths for a given grey level. For finer textures, grey levels change with higher frequency, thus shorter run lengths are expected. So, for textures with different coarseness, the distributions of their run lengths (for a fixed orientation) will vary. Using $r(i, j|\theta)$, several statistical features can be extracted (*e.g.* short run emphasis, long run emphasis, grey level distribution, run length distribution, run percentage, *etc.*).

The *GLCP* method describes the frequency of one grey level appearing in a specified linear relationship with another grey level, within the area under investigation [1]. Traditionally, the co–occurring probabilities, $p(i, j|\delta, \theta)$, are stored in a two dimensional joint probability matrix called the grey level co–occurrence matrix (*GLCM*). Each element $p(i, j|\delta, \theta)$ in the *GLCM* is the normalized frequency of co–occurrence between grey levels i and j for a given displacement δ and orientation θ. A different *GLCM* is needed for each (δ, θ) pair. A detailed discussion of the *GLCP* method is given in Section 3.2.

3.1.2 Comparison

This section provides an overview of previous research studies which compared first order and second order texture methods. It concludes by comparing the second order texture features generated by the *GLD*, *GLRL* and *GLCP* methods as mentioned above.

In general, if the features acquired through first order statistics are not discriminable, second order statistics should be used. For the task of SAR sea ice segmentation, studies have indicated that first order methods are insufficient. Among publications, Shokr [32] provides a comparison of first and second order (*GLCP*) texture measures for supervised classification of SAR sea ice. The objective of his study was to discriminate five categories of sea ice: multi year ice (MYI), first-year rough ice (FYR), first-year smooth ice (FYS), young ice (YI) and new ice (NI). The results indicated that the first order parameters, except for the variance statistic, are not significant

ice classifiers. The second order parameters are significant in two aspects: they are able to discriminate between ice classes, and they may also serve to construct a set of one–time decision boundaries to isolate those classes. As well, the energy and entropy statistics, when combined with the grey level, provided the highest discrimination capability.

In determining which second order approach is preferred, a comparison between GLD, $GLRL$ and $GLCP$ is needed. Of the many publications, Harlow and Conners [20] provide a very systematic and theoretical comparison. The study was designed to compare the relative loss of texture content information encountered by using the intermediate relationship matrices for each of the algorithms considered, where the matrices are: the GLD vector $p_\eta(i|\eta)$, the $GLRL$ matrix $R(i,j|\theta)$, and the $GLCM$ $P(i,j|\delta,\theta)$. A texture algorithm is said to experience a loss of texture context information if there exists two visually distinct textures which cannot be discriminated. When comparing statistical second order methods, they determined whether the intermediate relationship matrices contain information that allow the two textures to be discriminated. Hence, if the corresponding matrices produced from the two visually distinguishable textures are identical, an information loss is experienced.

In order to keep the experiment controlled, Harlow and Conners used textures with the same first order distributions (*i.e.* same mean, variance and skewness). It is worth noting that these are also the same textures used by perceptual psychologist B. Julesz in his investigations of human texture perceptions [24]. The results of the Harlow and Conners study indicate that the $GLCP$ features provide better discrimination ability compared to the the GLD and $GLRL$ features. In fact, it was theoretically indicated that the GLD and $GLRL$ methods are proper subsets of the texture pairs that can be discriminated by the $GLCP$ method. These theoretically derived results agreed very well with another experimental comparison performed by Weska *et al.* [38].

3.2   *GLCP* Texture Features

Application of *GLCP* texture features for interpreting SAR sea ice imagery is detailed in this section. Traditionally, the co–occurring probabilities are stored in the *GLCM*, hence, a description of the *GLCM* data structure is given. This is followed by an example calculation and an explanation of some texture statistics that are applied to the *GLCM*. The section concludes by discussing the optimal parameter set for the *GLCP* features with respect to SAR sea ice segmentation.

3.2.1   Explanation

GLCM

The co–occurrence probabilities offer a second order method for generating texture features. Here, a brief presentation is given on how to populate the *GLCM* data structure, but a more thorough explanation is provided by Haralick *et al.* [19]. Given a spatial window within the image, the co–occurrence probabilities represent the conditional joint probabilities of all pairwise combinations of grey levels given two parameters: interpixel distance (δ) and orientation (θ). It should be noted that since the image window is a discrete set, it is sometimes convenient to represent the parameters δ and θ as Cartesian co-ordinates δ_x and δ_y which are the interpixel spacings in the x– and y–directions, respectively. The probability measure can be defined as:

$$Pr(x) = \{C_{ij} \mid (\delta_x, \delta_y)\} \tag{3.3}$$

where C_{ij} (the co-occurrence probability between grey levels i and j) is defined as:

$$C_{ij} = \frac{P_{ij}}{\sum\limits_{i,j=0}^{G-1} P_{ij}} \tag{3.4}$$

where P_{ij} represents the frequency of occurrence between two grey levels, i and j, for a given displacement vector (δ_x, δ_y) (or displacement δ, and orientation θ), for the specified window size. G is the number of quantized grey levels for the entire image. The sum in the denominator represents the total possible number of grey level pairs within the image window. It is worth noting that as a consequence, $\sum_{\forall i,j} C_{ij} = 1$.

The *GLCM* is a data structure used to store the probabilities where index (i, j) in the matrix is the probability C_{ij}. Commonly used orientations (θ) are $0°$, $45°$, $90°$ and $135°$. The orientations $180°$, $225°$, $270°$ and $315°$ are redundant to the previous four directions, hence, they are typically paired together (*e.g.* $0°$ with $180°$, $45°$ with $225°$, *etc.*) to achieve a symmetric *GLCM*. Also, to ensure a reasonable computation time and non-sparse *GLCM*, the image is usually quantized. Quantization will be discussed Section 3.2.2.

Example

The procedure for calculating co-occurrence data is given in Figure 3.1. A comparison of two texture types is presented for this example. Here, a pair of 5×5 pixel windows are extracted from the image. The *GLCM* is calculated for $(\delta_x, \delta_y) = \{(1, 0), (-1, 0)\}$ (*i.e.* $\delta = 1$ and $\theta = 0°$, $180°$). One sub–image represents a smooth texture and the other represents a coarse texture. The number of grey levels has been quantized to 4 for the entire image. To determine the *GLCM*, the algorithm searches the image window for all possible pixel pairs for the given displacement vector (δ_x, δ_y). For example, the smooth texture has two occurrences of pixel pair $(0, 0)$, eight occurrences of the pixel pair $(0, 1)$, and so on. This procedure is carried forward for all possible combinations of grey levels until the matrix is populated. Using Equation 3.4, the matrix is normalized.

The distribution of non-zero elements in the the *GLCM* is expected to characterize the texture of the image. For example, Figure 3.1 illustrates how the *GLCM* probability distributions differ
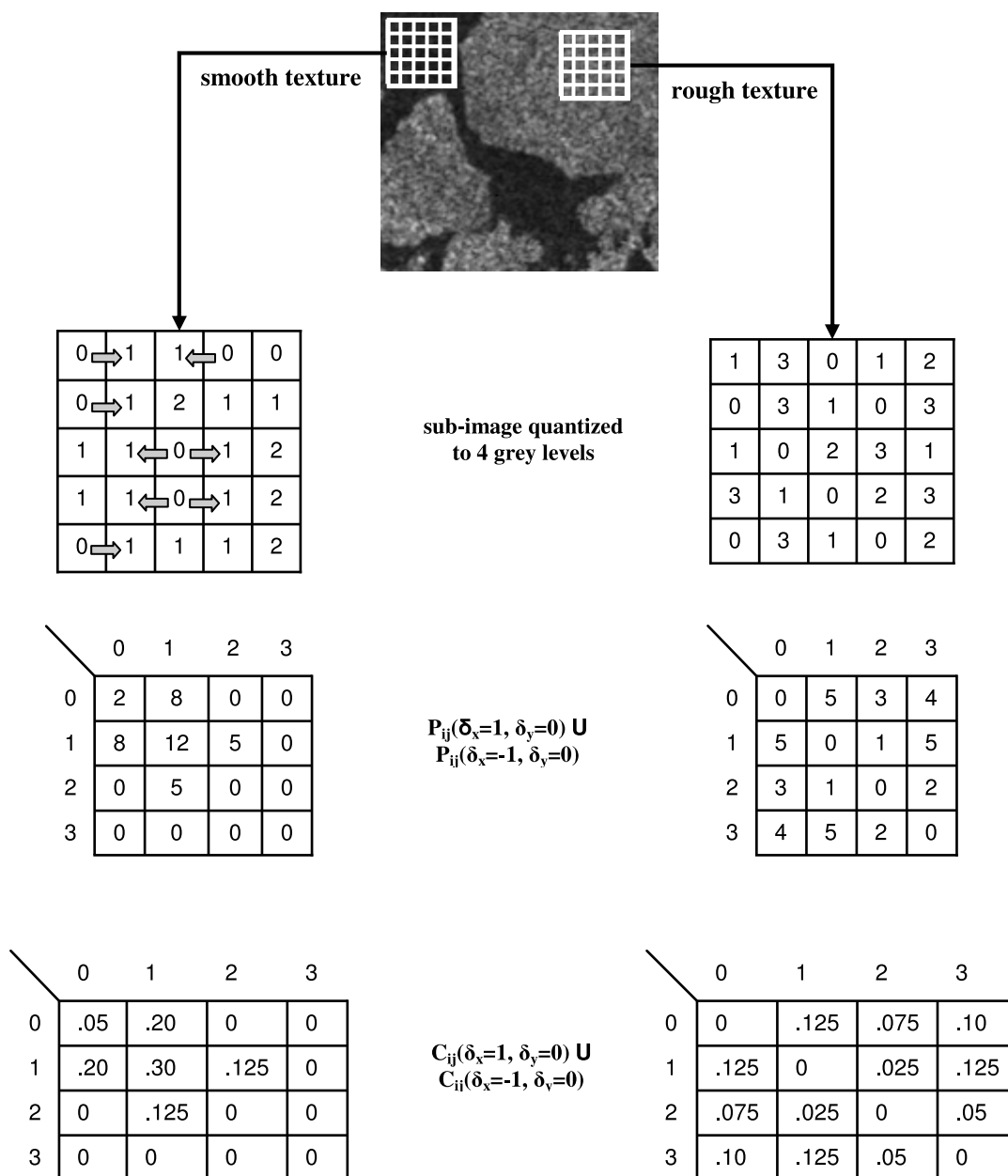
Figure 3.1: Grey level co–occurrence generation example ((δ_x, δ_y) = (1,0) and (-1,0), G = 4). These are example calculations of the *GLCM* for smooth (left) and rough (right) textures.

for smooth and coarse textures. The smooth texture has a high frequency of non–zero elements in the upper–left quadrant of the *GLCM*, indicating that the grey levels did not vary much within the image window. The coarse texture has a high dispersion of non–zero elements away from the diagonal, which indicates the texture is coarse relative to the image window. The differences in these *GLCM*s indicate the suitability of using this technique for texture analysis.

Statistics Defined

Based on the *GLCM*, there are numerous texture statistics that can be extracted. In particular, statistics which are grey level shift invariant are desirable. A statistic is said to be grey level shift invariant if it remains consistent given a DC shift in the mean grey level of the image.

Table 3.1 lists eight common grey level shift invariant statistics. In these equations, G is the number of grey levels in the image and is equal to the dimensions of *GLCM*. The terms (μ_x, μ_y) and (σ_x, σ_y) are the mean and standard deviation of the *GLCM* in the x– and y–directions respectively and are defined as follows:

$$\mu_x = \sum_{i,j=0}^{G-1} i \cdot C_{ij} \tag{3.5}$$

$$\sigma_x = \sum_{i,j=0}^{G-1} C_{ij} \cdot (i - \mu_i)^2 \tag{3.6}$$

Note that if the *GLCM* is symmetric, $\mu_x = \mu_y$ and $\sigma_x = \sigma_y$. Applying texture statistics to the *GLCM*, texture feature maps can be obtained for each pixel of the image. For a given image window, the resulting texture statistic calculated from the *GLCM* is said to belong to the center pixel of that window.

Maximum probability (MAX)	$max(C_{ij})$ for all (i,j)
Uniformity (ENE)	$\sum_{i,j=0}^{G-1} C_{ij}^2$
Entropy (ENT)	$-\sum_{i,j=0}^{G-1} C_{ij} log C_{ij}$
Dissimilarity (DIS)	$\sum_{i,j=0}^{G-1} C_{ij}|i-j|$
Contrast (CON)	$\sum_{i,j=0}^{G-1} C_{ij}(i-j)^2$
Inverse difference (INV)	$\sum_{i,j=0}^{G-1} \frac{C_{ij}}{1+|i-j|}$
Inverse difference moment (IDM)	$\sum_{i,j=0}^{G-1} \frac{C_{ij}}{1+(i-j)^2}$
Correlation (COR)	$\sum_{i,j=0}^{G-1} \frac{(i-\mu_x)(j-\mu_y)C_{ij}}{\sigma_x \sigma_y}$

Table 3.1: Grey level shift-invariant co-occurrence texture statistics

3.2.2   Parameter Selection for *GLCP*

Extraction of *GLCP* texture features from an image requires expert knowledge of the parameters involved. Poor selection of *GLCP* parameters produces an indiscriminable feature space, which results in unpredictable segmentation. The parameters involved in *GLCP* texture feature extraction are: (1) image quantization (G), (2) displacement vector (δ_x, δ_y), (3) statistic selection (Table 3.1) and (4) window size (n_x, n_y). A literature study of these four aspects is discussed below.

Image Quantization (G)

If the full dynamic range of an image is used, each *GLCM* is a 256×256 matrix (65536 entries). Also, if the image window size is 15×15, there are only $2 \times (15 \times 14) = 420$ entries in the matrix. For this situation, the *GLCM* will be quite sparse resulting in unnecessary time–consuming com-

putations of zero elements. To resolve this issue, a quantization method must be used. According to the literature [7, 35], the most effective quantization method with respect to classification ability is linear normalization and is defined:

$$I_{new}(i,j) = (G-1) \cdot \frac{I_{old}(i,j) - min(I_{old})}{max(I_{old}) - min(I_{old})} \tag{3.7}$$

where $I_{new}(i,j)$ and $I_{old}(i,j)$ are the grey levels at location (i,j) after and before quantization respectively. $max(I_{old})$ and $min(I_{old})$ are the maximum and minimum grey levels in the original image and G is the quantization level. This method makes best use of the dynamic range by mapping the original image to [0, G-1].

With respect to quantization, the most important decision is determining the minimum number of grey levels, G, needed to represent a set of textures successfully. Also, one has to consider that the computation time will grow with increasing G.

Soh and Tsatsoulis [35] conducted experiments on the quantization level and displacement vectors used for the *GLCM* and examined their effects on discriminating different SAR sea ice textures. They devised a test using various texture statistics with six different quantization schemes: 8, 32, 64, 128 and 256. The displacement vectors (δ_x, δ_y) used were (1,0), (1,1), (0,1), (-1,1). They used Euclidean distance measures to provide a visual interpretation of the trend between each neighboring quantization scheme (*e.g.* distance between 8 and 32, 32 and 64, *etc.*). The results indicated that $G = 8$ is not suitable due to its poor distinguishing ability and that a 64-bit representation is efficient and sufficient.

Clausi [7] conducted a study which analyzes grey level quantization on the classification ability and feature space separability of the co-occurrence statistics. He devised tests to analyze the classification performance of several texture statistics across many quantized grey levels (8, 12, 16, ..., 256). Further, he investigated the correlation relationship of the statistics as a function of grey level quantization. The results indicated many of the individual statistics have

peak classification at a relatively coarse quantization level (G), with a decrease in classification accuracy with increasing G. Setting G to a value greater than 24 is advocated, however, large values of G (> 64) are deemed excessive as they do not improve classification accuracy and are computationally expensive.

Thus far, there have been no extensive studies which analyze G for segmentation opposed to classification.

Displacement Vector (δ_x, δ_y)

Selection of the interpixel displacement vector is heavily dependent on the nature of the textures to be segmented. To reiterate, most studies view the displacement vector as two separate parameters: displacement (δ) and orientation (θ)

Several studies [22, 33, 35] average the four orientations $(0°, 45°, 90°$ and $135°)$ as the authors assume that the texture measures are insensitive to the direction of the sensor and/or realize that sea ice formations have no inclination to a certain orientation. Conversely, Barber and LeDrew [2] determined that orientations aligned with the look direction of the SAR produce results that have greater statistical significance.

With respect to displacement, δ, the choice relies on the perceived frequency of the texture. For textures with relatively low frequency, larger displacements are needed to capture the pattern. With respect to SAR sea ice segmentation, there have been several recommendations for selecting δ in the literature [2, 22, 33, 28, 35]. Barber and LeDrew [2] statistically prove that $\delta = 1$ generates considerably advanced classification when compared to $\delta = 5$ and $\delta = 9$. Holmes *et al.* [22] indicate through experimentation that $\delta = 2$ is the preferred displacement, however, they do not give a detailed account of their experimentation techiques which led them to this statement. Shokr [33] conducts a study where he experimentally compares $\delta = \{1, 2, 3\}$ and determines $\delta = 2$ is the most suitable. Nystuen and Garcia [28] conduct a study where they

use $\delta = \{1, 2, \ldots, 10\}$ and conclude that $\delta > 4$ produce the most consistent features. However, it should be clarified that consistency does not necessarily translate into increased segmentation accuracy. Soh and Tsatsoulis [35] recommend using multiple displacement values for classifying SAR sea ice imagery.

Statistic Selection

Many of the statistics suggested by Haralick [19] produce highly correlated texture features [2, 33, 1]. From a pattern recognition perspective, it is highly desirable to minimize the correlation of the feature space dimensionality to improve classification accuracy [14]. Barber and LeDrew [2] indicate the best texture discrimination is achieved for a set of three texture statistics considered simultaneously. However, in this paper, they make no direct conclusions as to which statistics are preferred.

Baraldi and Parmiggiani [1] present a thorough analysis of the *GLCP* texture statistics. In this study, they prove that energy and entropy are highly correlated and only one of them should be used for segmentation. As well, contrast and variance measure different texture concepts but present a very similar behavior in the detection of many texture types. Inverse difference moment was shown to be a combination of the textural effects characterizing both energy and contrast. Since these two effects are numerically distinguishable, the use of inverse difference moment is not recommended. Their final conclusions indicate that two parameters, energy (or entropy) and contrast, are the most significant in classification.

Clausi [7] studied the correlation relationship of the statistics as a function of quantization. From this, he determined a preferred set of statistics for texture recognition. He concludes that entropy, contrast and correlation compose a preferred feature set.

Window Size (n_x, n_y)

In a study by Yue [40], she investigates how the window size influences the texture features. Her results indicate that the standard deviation of the texture features increase as the window size decreases. An increase in standard deviation of the texture features leads to poorer segmentation ability, thus, it is necessary to choose larger window sizes.

Generally, it is accepted that the window size should be large enough to characterize the region of interest. If the window size is too small, this will result in a poor neighborhood approximation of the region of interest. If the window size is too large, it is more likely to overlap multiple classes in the image, thus eroding the class boundary. This becomes problematic for SAR sea ice interpretation as there are many texture boundaries.

For the segmentation problem, generally speaking, fine textures require relatively smaller window sizes whereas smoother textures require larger window sizes. As well, one has to base the window size on the size and shape of the ice floes to be monitored.

3.3 Unsupervised Segmentation

Once the features have been extracted from the image, it is necessary to group pixels according to their feature values, this is called classification. Classification can be either supervised or unsupervised. Supervised classification is used when the characteristics of each distinct object type in the image is known. This involves some *a priori* knowledge of the data set and will often require the role of an analyst to manually locate homogenous regions of known land–cover types in the remotely sensed image. The spectral characteristics of these known regions are used to train the segmentation algorithm to segment the remainder of the image. As this method requires human intervention, it detracts from the goal of having a fully automated segmentation approach. In unsupervised segmentation, the identity of object types within the image are assumed to be

unknown. A clustering scheme is used to group together like pixels into different classes according to some similarity measures. Improving the pixel measurements will ease the burden of the clustering process. As well, a clustering methodology that consistently and accurately separates relevant classes within an image is desirable. Unsupervised segmentation requires minimal *a priori* knowledge and human interaction. The remainder of this section will give a brief presentation of the k-means clustering algorithm, which is an unsupervised segmentation technique. A more thorough explanation of k-means is provided by Dude, Hart and Stork [14].

Given the number of classes, k, within an image, the algorithm will attempt to find the class mean vectors $\vec{\mu_1}, \vec{\mu_2}, \ldots, \vec{\mu_k}$ within the feature space. Then, for each data point $\vec{x_i}$ in the feature space, it will assign $\vec{x_i}$ to the nearest class using the minimum Euclidean distance (MED). A procedural description of k-means follows:

1. Assign k prototypes $\vec{\mu_1}, \vec{\mu_2}, \ldots, \vec{\mu_k}$ at random.

2. For each data point $\vec{x_i}$, assign $\vec{x_i}$ to the closest prototype.

   $$\vec{x_i} \, \epsilon \, C_j \quad \text{if} \quad |\vec{x_i} - \vec{\mu_j}| < |\vec{x_i} - \vec{\mu_k}| \quad \forall \, k, \; j \neq k$$

3. For each class C_j, let $\vec{\mu_j}$ = sample mean of points in C_j. If C_j contains no data points, then select $\vec{\mu_j}$ at random.

4. If any class prototypes have changed in step 3, then goto step 2; else done.

Note that the k-means algorithm requires the user to indicate the number of classes. The performance of the algorithm is affected by the size, shape and density of each class in the feature space. As well, the scale and resolution of each feature dimension could affect the success of the algorithm.

To improve cluster separability and segmentation accuracy, the feature space is typically linearly normalized according to Equation 3.7. In this case, each axis of the feature space is

normalized to the range $[0, 1]$, hence, $G = 2$ for this equation and does not represent the number of quantized grey levels. By normalizing each axis in the feature space, differences in scale and resolution amongst feature axes are eliminated.

Chapter 4

Proposed Method: *WGLCP* Texture Features

When calculating the *GLCP* distribution for a given image window, the *GLCP*s are drawn from a uniform distribution. A method is proposed to improve the texture features for the purposes of segmentation and boundary preservation. In this approach, pixel pairs closer to the center of the image window are given higher significance than those further from the center.

This chapter begins by discussing the problems associated with *GLCP* texture features. Essentially, by demonstrating some SAR sea ice segmentation results using *GLCP* texture features, the need for a weighted image window will be motivated. This is followed by a complete formulation of the weighted *GLCP* texture features. The chapter ends by discussing the parameters for an optimal weighted feature set.

4.1 Motivation

When extracting *GLCP* features from an image, larger image windows are needed to ensure the *GLCM* is well sampled (Section 3.2.2). A smaller window with poorly sampled data will result in unreliable and noisy features, thus poorer segmentation. Although large window sizes are needed to capture meaningful features, they will erode texture boundaries. As well, texture boundaries are more severely eroded with natural imagery, where the boundaries have non–linear shape. Typically, in the literature, scientists will use test images with horizontal and/or vertical linear texture boundaries which are well–suited for square image windows. As a result, these images are easier to segment but are not indicative of natural boundaries found in SAR imagery. Larger window sizes also become problematic in images with high "boundary density", such as SAR sea ice imagery. Here, boundary density is a term used to describe regions in images with a high frequency of multiple classes, or texture boundaries.

To demonstrate the influence of window size on *GLCP* texture segmentation ability, a SAR sea ice image was segmented using the *GLCP* texture features with two different window sizes: 9×9 and 15×15. The sea ice image shown in Figure 4.1 is obtained from Barber *et al.* [2]. The image is extracted from X-band, HH polarization, STAR-1 with a six meter resolution. Land cover and three ice types are included in the image. The ice types included are first year smooth (FYS) ice, first year rough (FYR) ice and multi year ice (MY). After *GLCP* feature extraction, the feature space was linearly normalized and segmented using k-means clustering ($k= 3$). It is worth noting that the land cover is masked (and omitted) during segmentation because the location of land cover can easily be obtained from GIS (Geographical information systems).

Comparing the segmentation results in Figure 4.2, one can notice that the smaller window size provides a suitable ice map but still results in inconsistent and noisy segmentation. Ideally, there should be no noise artefacts in the lower–left quadrant of the image. This agrees with the
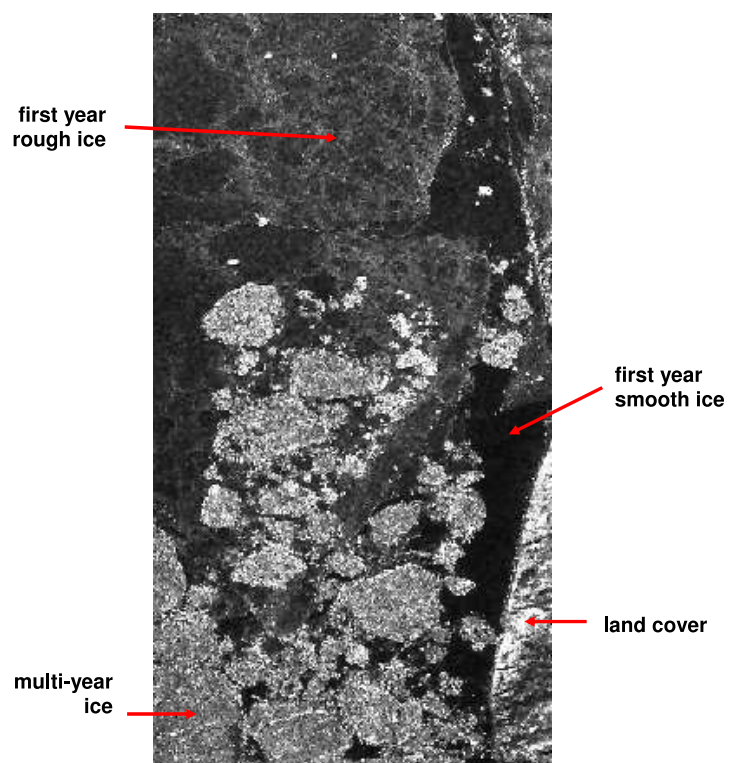
Figure 4.1: STAR–1, X–band, HH polarization image of Mould Bay, NWT (March 1984), six meter resolution. Contains land cover and three ice types: FYS, FYR and MY.

(a) 9×9 window   (b) 15×15 window

Figure 4.2: STAR–1 segmentation results Using different window sizes. FYS labelled black, FYR labelled dark grey, MY labelled white and land cover labelled light grey. The smaller window size provides an accurate, but noisier ice map. The larger window size is more consistent, but there is a considerable amount of misclassification near texture boundaries.

study conducted by Yue in [40]. Her results indicate that the standard deviation of the texture features increase as the window size decreases, which leads to poorer segmentation ability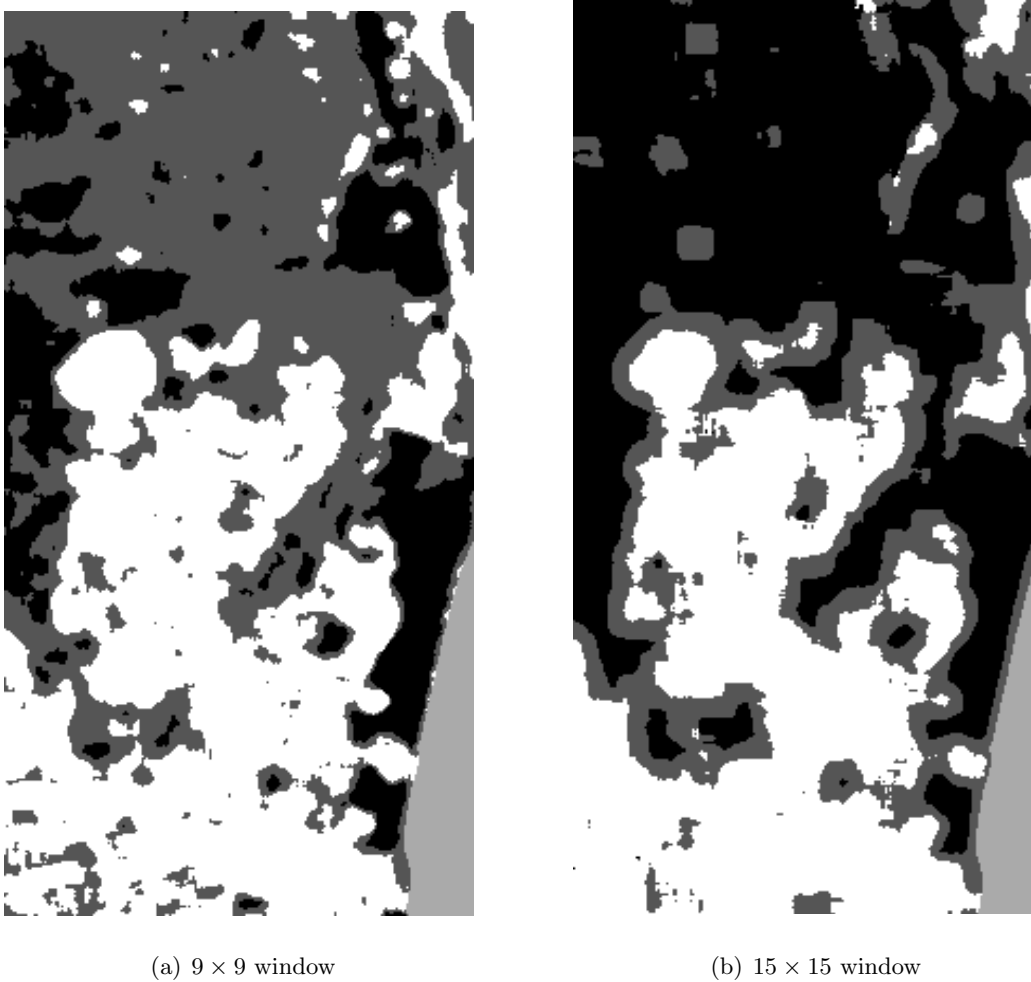. The segmentation results for the larger window size are more consistent at separating the ice types from one another, however, there is a considerable increase in misclassification near the class boundaries and narrow texture regions in this ice map. This is apparent in the loss of detail in the middle–left region of the image where there are disjoint regions of MY ice that appear merged in the results. As well, it appears that the label for FYR ice is detecting the class boundary between FYS and MY ice, rather than separating the relevant ice types. Essentially, there are two competing objectives in choosing the window size for $GLCP$ feature extraction. The first objective is to develop a consistent and discriminable feature set, which requires adequate samples provided by larger window sizes. The second objective is to preserve texture boundaries within the image, which requires decreasing the window size to minimize the amount of texture boundary overlap during feature extraction. These objectives become especially problematic for SAR sea ice segmentation due to the high frequency of boundaries contained in a scene. The goal of this thesis is to develop a feature extraction method which will provide consistent and discriminable features while preserving texture boundaries.

A modification to the $GLCP$ feature extraction method is proposed to preserve texture boundaries while providing consistent and discriminable feature sets. Using this approach, a pixel pair closer to the center of the image window is given higher significance than those on the border. As illustrated in Figure 4.3, the mean spatial location of a pixel pair is calculated and is defined as r_{ij}. Then, the Euclidian distance of r_{ij} to the center of the image window will determine the relative probability of co-occurrence. As shown in Figure 4.3, the problem is as simple as determining the distance from A' to A, then weighting the pixel pair according to the distance measured. By employing this weighting scheme, larger window sizes are permitted which will lower the variability of the texture features (thus providing better segmentation) as indicated in [40]. As well, since
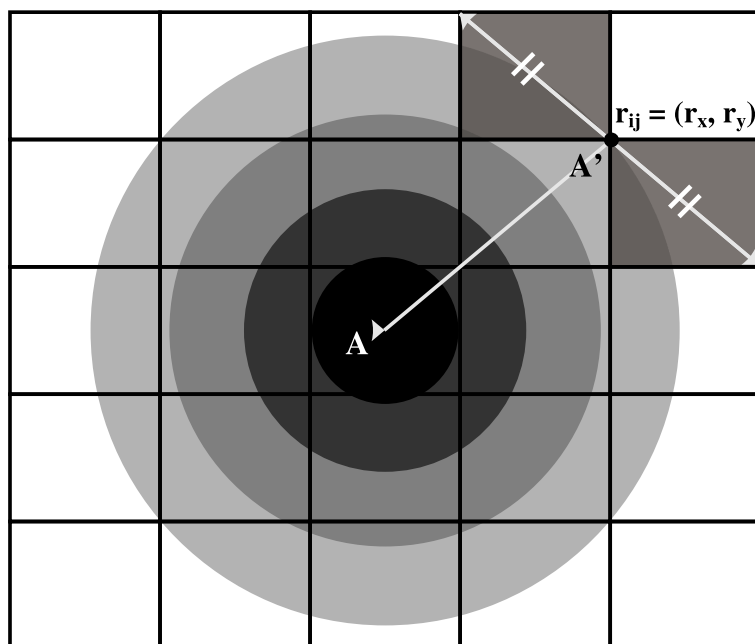
Figure 4.3: Measuring the pixel pair distance to the center of the image window

the features measured belong to the center pixel of the image window, weighting the pixel pair distance to the center of the image window will result in better neighborhood approximations of the feature values, thus preserving the texture boundaries. In multiple texture regions, the measurements are weighted towards the texture properties of the neighborhood surrounding the center pixel. In homogenous texture regions, the proposed method is expected to still provide consistent, reliable features. A thorough testing of these concepts follow in Chapter 5.

4.2 Formulation

The location of the pixel pair to the center of the image window determines the relative probability of co-occurrence for the weighted *GLCM*. The greater the length of A'–A in Figure 4.3, the lower the probability of occurrence.

Assume the effective image window, W, is rectangular with n_x columns and n_y rows (where

W(-2,-2)	W(-1,-2)	W(0,-2)	W(1,-2)	W(2,-2)
W(-2,-1)	W(-1,-1)	W(0,-1)	W(1,-1)	W(2,-1)
W(-2,0)	W(-1,0)	W(0,0)	W(1,0)	W(2,0)
W(-2,1)	W(-1,1)	W(0,1)	W(1,1)	W(2,1)
W(-2,2)	W(-1,2)	W(0,2)	W(1,2)	W(2,2)

Table 4.1: Example of indexing scheme for 5×5 image window

n_x and n_y are odd numbers). Then the image window can be indexed as follows:

$$
\begin{aligned}
W_x &\in \left\{ -\lfloor \frac{n_x}{2} \rfloor, -(\lfloor \frac{n_x}{2} \rfloor - 1), \ldots, (\lfloor \frac{n_x}{2} \rfloor - 1), \lfloor \frac{n_x}{2} \rfloor \right\} \\
W_y &\in \left\{ -\lfloor \frac{n_y}{2} \rfloor, -(\lfloor \frac{n_y}{2} \rfloor - 1), \ldots, (\lfloor \frac{n_y}{2} \rfloor - 1), \lfloor \frac{n_y}{2} \rfloor \right\}
\end{aligned}
\tag{4.1}
$$

where $W_x \times W_y$ is the set of pixels in the image window indexed by their x–y (i.e. column–row) designations as outlined by the example in Table 4.1. This indexing scheme is selected so that the origin of the image window will reside at the center pixel location (*i.e.* coordinate $(0,0)$ is the center of image window), which is convenient for calculating the weighted grey level co-occurrence probabilities (*WGLCP*). The grey levels in the image window can be represented as a function of the index as follows:

$$
W(x, y) = i, \ where \ i \subseteq \{0, 1, \ldots G - 1\}
\tag{4.2}
$$

where G is the number of grey levels in the image.

Given two pixels in the image window that are separated by (δ_x, δ_y), one with grey level i, the other with grey level j, the pixel pair location is simply the mean location of $W(x_1, y_1)$ and $W(x_2, y_2)$, and is defined as follows:

$$
\begin{aligned}
r_{ij} &= r_{ij}(W(x_1, y_1), W(x_2, y_2)) \\
&= \left(\frac{x_1 + x_2}{2}, \frac{y_1 + y_2}{2} \right) \\
&= (r_x, r_y)
\end{aligned}
$$

$$given,$$

$$W(x_1, y_1) = i, \ W(x_2, y_2) = j, \ (\delta_x, \delta_y) = (x_1 - x_2, \ y_1 - y_2) \tag{4.3}$$

In the previous chapter, P_{ij} is defined as the co–occurring frequency between two grey levels (Equation 3.4). However, in this formulation, P_{ij} is the non–normalized weighted co-occurring probability and is a Gaussian function of r_{ij}. Formally, for a fixed interpixel displacement vector (δ_x, δ_y), the non–normalized weighted co-occurring probability is:

$$P_{ij} = \sum_{\forall r_{ij}} \frac{1}{2\pi\sigma_x\sigma_y} \exp\left\{ -\frac{1}{2}\left[\left(\frac{r_x}{\sigma_x}\right)^2 + \left(\frac{r_y}{\sigma_y}\right)^2 \right] \right\} \tag{4.4}$$

where σ_x and σ_y represent the standard deviation of the Gaussian probability density function (pdf) in the x– and y–directions respectively. Essentially, this method uses the Euclidean distance of the pixel pair to the origin to determine the weighted co-occurring probabilities. The *GLCM* data structure is used to store these weighted probabilities, hence, Equation 3.4 from the previous chapter can be used to normalize P_{ij}. In theory, if the standard deviations are sufficiently small relative to the window size, P_{ij} will already be normalized. The statistics from Table 3.1 can be applied to extract texture features.

4.3 Selecting Standard Deviation

As indicated by Equation 4.4, the calculation of the *WGLCP*s introduces two new parameters: σ_x and σ_y – standard deviations in the x– and y–directions respectively for the Gaussian pdf. Typically, square image windows are used, hence, $\sigma = \sigma_x = \sigma_y$. The standard deviation controls the weighted probability given to a pixel pair within the image window. Smaller standard deviations (σ) indicate that pixel pairs further away from the center of the image window should be given less significance, whereas larger values for standard deviation provide a more uniform weighting scheme. Selecting a value for σ should depend on two factors: the boundary density in the image and the *GLCP* window size.

The boundary density in an image influences the selection of σ. More boundaries in the image will result in more occurrences where the image window will overlap multiple textures. As the window overlaps multiple textures, the co-occurring probability distribution is affected, resulting in indiscriminable features. By using a smaller standard deviation, the outlying pixel pairs in the image window will be given less significance, resulting in a better local approximation of the true texture measure in areas where the image window overlaps multiple classes. Figure 4.4 is an enlarged section of a SAR sea ice image. The smoother dark region is water, the higher frequency bright region is ice and the red box represents a window used to calculate the *WGLCP* texture features. The window contains a mixture of water and ice classes, thus, by using a smaller σ to calculate the *WGLCP*s, the effects of ice will be less predominant and will result in an improved feature measurement. In situations where the window is in a homogenous texture region, there are no foreseen adverse effects; the texture characteristics of the center neighborhood (of the window) are still given higher significance, but since the region is homogenous, it should not be of concern what neighborhood of the window is given higher weighting.

Another factor influencing the selection of standard deviation is the window size used to deter-
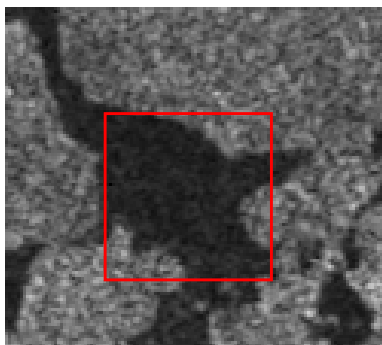
Figure 4.4: SAR sea ice image which illustrates need for using smaller deviations. The image window contains multiple textures.

mine the *WGLCP* texture features. The size of the window determines the maximum Euclidean distance that a pixel pair will be from the center, hence, the standard deviation should be selected accordingly. To maximize the energy of the Gaussian pdf within the effective image window, the standard deviations are estimated to be $\frac{1}{4}$ of the window size. This captures approximately 95 percent of the pdf's energy (area) in the effective window. Formally, the standard deviation can be written as a function of the window size as follows:

$$\sigma_x = \frac{n_x}{4}, \quad \sigma_y = \frac{n_y}{4} \tag{4.5}$$

4.4   Summarizing *WGLCP* Method

The *WGLCP* method is applied in Chapter 5 and is summarized as follows:

1. Place image window at starting location of image and initialize elements in *GLCM* to 0.

2. (a) For pixel $W(x, y) = i$, find the corresponding pixels located at a displacement $\pm(\delta_x, \delta_y)$ if applicable.

$$W^+(x + \delta_x, y + \delta_y) = j \text{ and } W^-(x - \delta_x, y - \delta_y) = k,$$

where $i, j, k \subseteq \{0, 1, \ldots G - 1\}$.

(b) Find mean co–ordinate for W–W^+ and W–W^- as follows:

$$W\text{–}W^+ = r_{ij} = (x + \tfrac{\delta_x}{2}, y + \tfrac{\delta_y}{2}) \text{ and } W\text{–}W^- = r_{ik} = (x - \tfrac{\delta_x}{2}, y - \tfrac{\delta_y}{2})$$

(c) Update $GLCM$ data structure as follows:

$$P_{ij}^{(new)} = P_{ij}^{(old)} + \frac{1}{2\pi\sigma_x\sigma_y} \exp\left\{ -\frac{1}{2}\left[\left(\frac{x+\frac{\delta_x}{2}}{\sigma_x}\right)^2 + \left(\frac{y+\frac{\delta_y}{2}}{\sigma_y}\right)^2 \right] \right\}$$

$$P_{ik}^{(new)} = P_{ik}^{(old)} + \frac{1}{2\pi\sigma_x\sigma_y} \exp\left\{ -\frac{1}{2}\left[\left(\frac{x-\frac{\delta_x}{2}}{\sigma_x}\right)^2 + \left(\frac{y-\frac{\delta_y}{2}}{\sigma_y}\right)^2 \right] \right\}$$

3. Repeat step 2 for all pixels in image window.

4. Normalize $GLCM$ such that the sum of all elements in the matrix is 1.

5. Calculate desired statistics according to Table 3.1 and store them in an n–dimensional vector $\vec{f}$.

6. Assign $\vec{f}$ to the center pixel in the image window.

7. Shift window over one column in image. If at end column of image, begin a new row. Repeat step 1 until end of image.

Chapter 5

Experiments and Results Analysis

The *GLCP* method has been used extensively to classify sea ice types in SAR for decades. From the literature, there exists strong supportive evidence that this method is the preferred texture analysis algorithm for SAR sea ice identification [2, 5]. However, this method suffers as it consistently misclassifies relevant ice types near textured boundaries. To overcome these shortcomings, the *WGLCP* texture features have been developed. The chapter begins by comparing the *GLCP* and *WGLCP* texture features with respect to boundary preservation, segmentation ability, robustness and computational demands. From this comparative study, an inconsistency with the *GLCP* correlation statistic was observed. This motivated a thorough investigative study into the suitability of using the correlation statistic for image segmentation. As the overall goal of this thesis is to improve unsupervised sea ice segmentation accuracy, the concepts developed from this study were used to develop a preferred feature set used to segment various images.

5.1 Comparison of *GLCP* and *WGLCP* Texture Features

Four criteria were used to compare the performance of the *GLCP* and *WGLCP* feature sets: (1) boundary preservation, (2) segmentation ability, (3) robustness to increasing boundary density and (4) computational demands. This section is comprised of four tests to address these criteria.

The first test will compare the *GLCP* and *WGLCP* feature sets with respect to boundary preservation. Edge transects of the features are taken across various textured bi–partite images and compared. The second test is a comparison of the feature sets with respect to SAR sea ice segmentation ability. The texture feature sets are applied to the unsupervised segmentation problem and compared. The third test assesses the robustness of the feature sets, where robustness is the segmentation performance as a function of increasing image boundary density. Essentially, as the boundary density of an image increases, the segmentation ability of the texture features deteriorates. This test compares the robustness of *GLCP* and *WGLCP* feature sets in terms of segmentation ability as the image boundary density increases. The final test will compare the computational time required for feature extraction for both feature sets.

5.1.1 Determining the Texture Boundary Response

Explanation

An edge transect is a profile view of a texture feature as the image window moves across a row in the image. The purpose of this test is to measure and compare the response of the *GLCP* and *WGLCP* features across a texture boundary.

As illustrated in Figure 5.1, an artificial bi–partite image is formed with a vertical boundary. The left–hand side of the image is texture "A" and right–hand side is texture "B". The edge transects were calculated as follows:
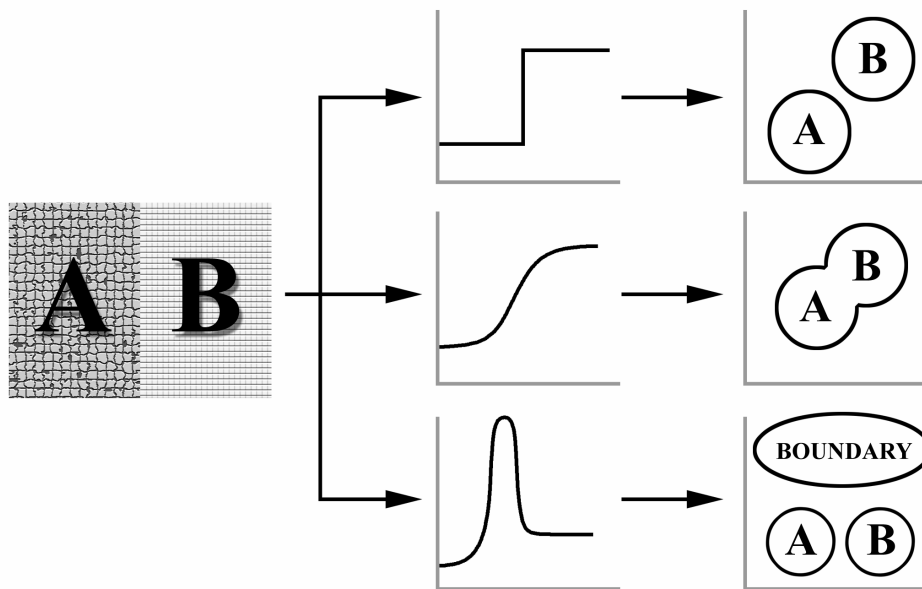
1. Randomly select a row in the image.

Figure 5.1: Visual interpretation of edge transects. Illustrated are ideal (step–like), over– and under–damped texture boundary transitions for the edge transects. Each type of response will have impact on the feature space separability.

2. For each position in the given row, calculate the relevant *(W)GLCP* statistics for the different displacement vectors:

$$(\delta_x, \delta_y) = \{(1, 0), (1, 1), (0, 1), (-1, 1)\}.$$

3. To make the features directionally invariant, average each statistic over the four displacement vectors used.

4. To increase the signal–to–noise ratio, repeat steps 1 to 3 twenty times and average over the twenty samples.

5. As mentioned in Section 3.3, normalize the feature space between [0, 1] to improve cluster separability.

6. For each feature, plot the feature value versus image column position. Observe the results.

Ideally, the value of a feature will have a step–like transition as it crosses the texture boundary, which results in well–defined separable clusters. In practice, this transition will be over– or under–damped [13], which is not as desirable. These scenarios are outlined in Figure 5.1. An over–damped response indicates that the measure is a mixture of both texture values as it crosses the texture boundary. This causes a higher within-class variance and lower between-class separability, resulting in poor cluster discrimination as indicated in the figure. In cases where the response is severely under–damped, the edge transect results will have significant overshoot as it crosses the texture boundary. This will cause a confounding feature space in scenarios where there is a high boundary density. Essentially, features which are close to the boundary will form a distinct and separable third class as illustrated in Figure 5.1. This will cause the algorithm to separate boundary versus non–boundary pixels rather than separate different textures. Note that this scenario will occur only if there is severe overshoot in the edge transect response (*i.e.* approaching an impulse–like response), in cases where there is minimal overshoot, this will not be an issue.
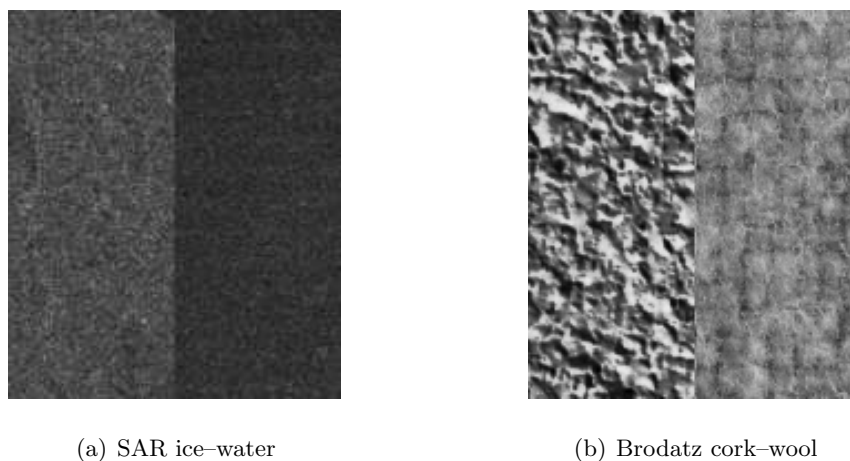
(a) SAR ice–water   (b) Brodatz cork–wool

Figure 5.2: Bi–partite test images with vertical boundary that are used to determine the texture boundary response of the feature sets.

Test Data

Figure 5.2 illustrates the two bi–partite images that were used in the tests. The first image consists of SAR ice (left–side) and SAR water (right–side) textures. These textures were extracted from Radarsat-1 of Beaufort Sea (June 1998) using ScanSAR wide beam mode (Section 2.2). The reason for selecting these textures is obvious as the goal of this thesis is to improve SAR sea ice segmentation. The second image is comprised of cork (left–side) and wool (right–side) textures from the Brodatz photo album [4]. These textures were selected because they have a well–defined texture pattern and Brodatz imagery is used extensively in the literature. Also, it is worth noting that the textures for the Brodatz image were adjusted to have the same mean grey level (DC shift with no information loss). Table 5.1 summarizes the parameters used in feature extraction for the transects.

| (W)GLCP Parameters	Values
Displacement Vector	(1,0), (1,1), (0,1), (-1,1)
Quantization	32 levels
Statistics	entropy, contrast, correlation
Window Size	19×19
Number of Samples	20
Standard Deviation	$\frac{n}{4} = 4.75$ (for *WGLCP* only)

Table 5.1: *GLCP* and *WGLCP* parameters used in feature extraction for bi-partite images.

Methods of Analysis

To objectively compare the performance of the feature sets, the transect results of the *GLCP* and *WGLCP* methods must be quantified. To accomplish this, the average gradient of the feature as it crosses the texture boundary is computed. The central difference is used to calculate the gradient for a given function, $f(x)$:

$$f'(x) = \frac{f(x+1) - f(x-1)}{2} \tag{5.1}$$

For a window size of 19×19, approximately 10 samples of $f'(x)$ are taken across the texture boundary and averaged; this is defined as the average gradient for the texture boundary. Note that this is deemed to be a sufficient number of samples to adequately reflect the slope of the boundary transition based on the effective window size. By taking a ratio of the average gradient for *WGLCP*:*GLCP*, the methods can be compared. If this number is > 1, it indicates that *WGLCP* feature has a steeper texture boundary response and is more desirable.
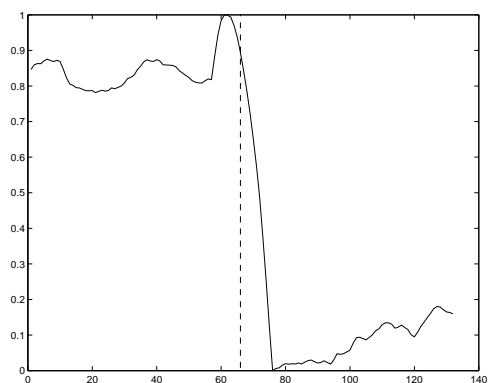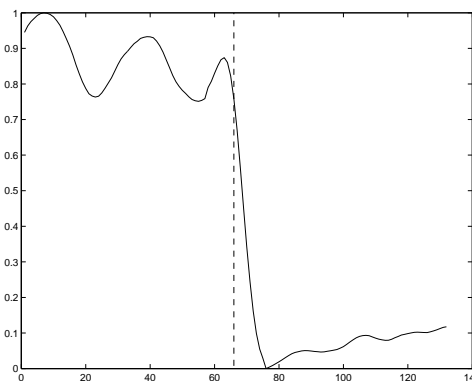
(a) *GLCP*: entropy results
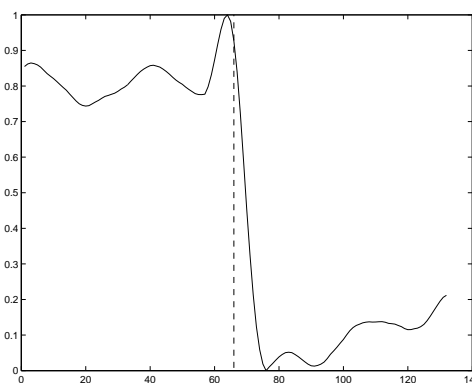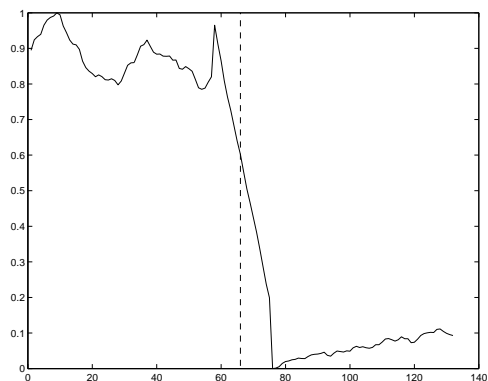
(b) *WGLCP*: entropy results

(c) *GLCP*: contrast results

(d) *WGLCP*: contrast results

(e) *GLCP*: correlation results

(f) *WGLCP*: correlation results

Figure 5.3: Edge transects for SAR ice–water bi–partite image for selected feature statistics.
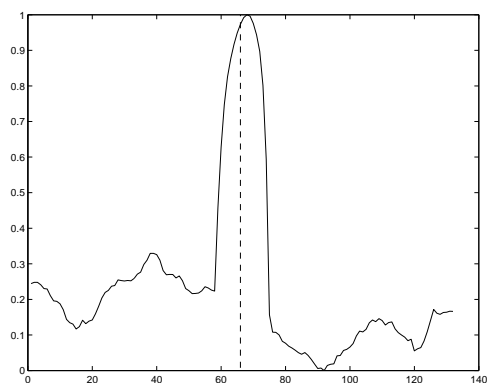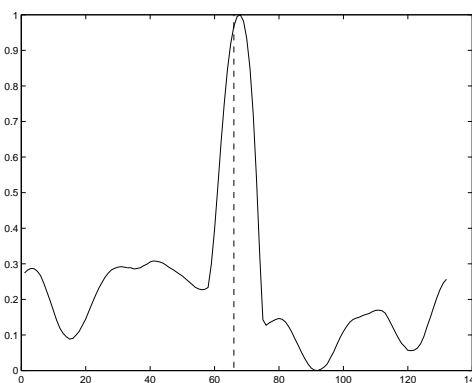
(a) *GLCP*: entropy results

(b) *WGLCP*: entropy results

(c) *GLCP*: contrast results

(d) *WGLCP*: contrast results

(e) *GLCP*: correlation results

(f) *WGLCP*: correlation results

Figure 5.4: Edge transects for Brodatz cork–wool bi–partite image for selected feature statistics.
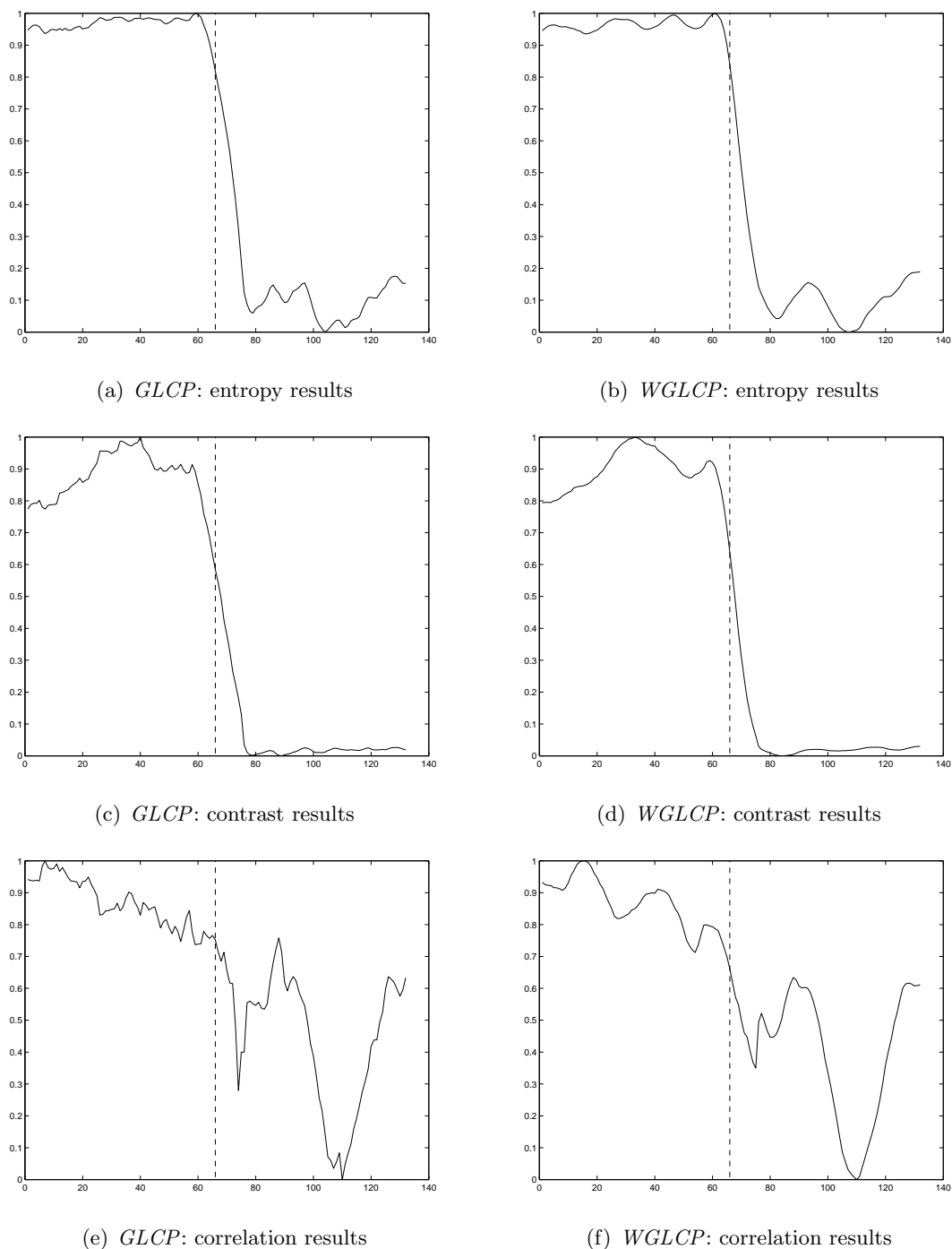
	SAR image	Brodatz image
entropy	1.30	1.22
contrast	2.12	1.48
correlation	N/A	N/A

Table 5.2: *WGLCP*:*GLCP* average gradient ratio for selected statistical features.

Results

Figures 5.3 and 5.4 show the edge transect plots for the SAR and Brodatz bi-partite images respectively. For these figures, the statistical features used were entropy, contrast and correlation as recommended in [7]. The dashed vertical line in these figures represents the true texture boundary. For the SAR ice–water results in Figure 5.3, it is visually apparent that the *WGLCP* features have a sharper transect response as they cross the texture boundary, indicating better boundary preservation. However, for the correlation statistic, both (*GLCP* and *WGLCP*) transects are impulse–like at the texture boundary. This is similar to the under–damped scenario explained in Figure 5.1, and causes one to question the true suitability of using the correlation statistic for SAR sea ice segmentation. As a result, a thorough investigation into the *GLCP* correlation statistic is given Section 5.2. Figure 5.4 for the Brodatz cork–wool image also illustrates that the *WGLCP* texture features provide a sharper response across the texture boundary. However, in this scenario, the correlation statistic does not give an impulse–like response across the texture boundary, but, appears very noisy and indiscriminable.

Table 5.2 outlines the *WGLCP*:*GLCP* average gradient ratio for the SAR and Brodatz edge transects as they cross the texture boundary. For all statistics, the *WGLCP*:*GLCP* is greater than 1 indicating the *WGLCP* features provide a steeper response, which suggests they will provide better boundary preservation during segmentation.

(W)GLCP **Parameters**	**Values**
Displacement Vector	(1,0), (1,1), (0,1), (-1,1)
Quantization	32 levels
Statistics	entropy, contrast, correlation
Window Size	15×15
Standard Deviation	$\frac{n}{4} = 3.75$ (for *WGLCP* only)

Table 5.3: *GLCP* and *WGLCP* parameters used for SAR sea ice segmentation.

5.1.2 SAR Sea Ice Segmentation Ability

Explanation

To compare the segmentation abilities of the *GLCP* and *WGLCP* features, SAR sea ice images are interpreted using unsupervised segmentation. Table 5.3 outlines the *(W)GLCP* parameters used for this experiment as recommended by the literature review in Section 3.2.2. After feature extraction, the feature space was normalized and k-means clustering was applied.

Test Data

Test set 1 (Figure 5.5) is a scene captured in the Beaufort Sea (June 1998) from Radarsat–1 ScanSAR wide beam mode (Section 2.2). A manual segmentation of the image is included with the test set and is used as *ground truth* for analysis. This image was selected as it has relatively equal proportions of ice and water pixels (*i.e.* 55% ice, 45% water).

Test set 2 (Figure 5.6) is of Baffin Bay (June 24, 1997) and is also from Radarsat–1 with the same imaging parameters. As above, the manual segmentation of the image is included in the test set and will be used in analysis. This image was selected due to the numerous amount of cracks within the ice floes. These cracks increase the number of ice–water boundaries and cause
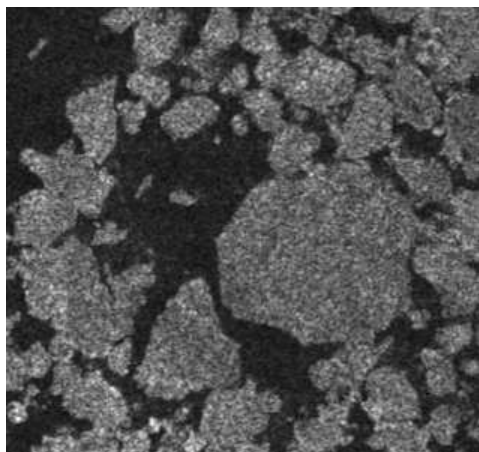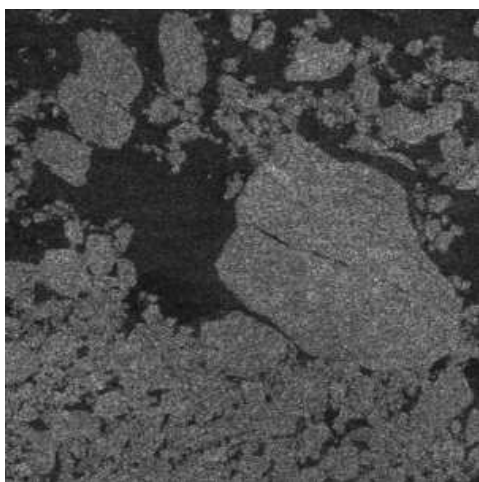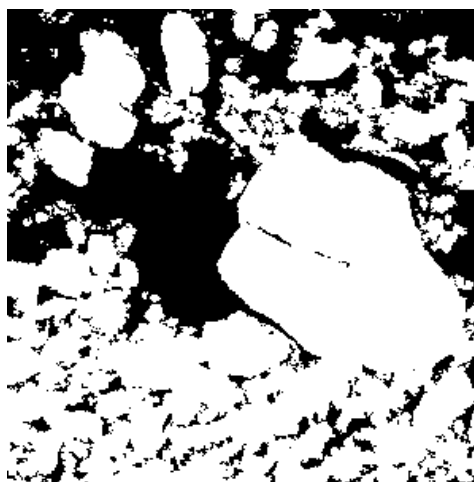
(a) Original
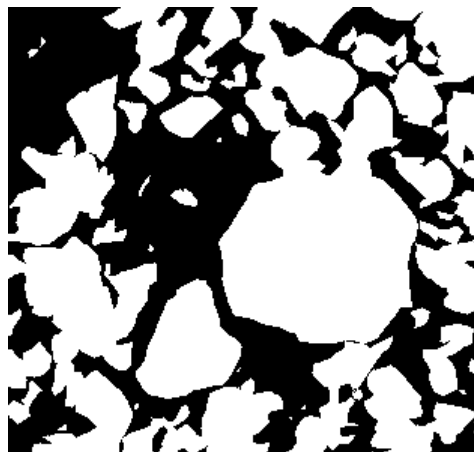
(b) Manual Segmentation

Figure 5.5: Test set 1 – SAR sea ice image from Beaufort Sea.

(a) Original

(b) Manual Segmentation

Figure 5.6: Test set 2 – SAR sea ice image from Baffin Bay.

	True Categories	
	X	**Y**
X	A	B
Y	C	D

Table 5.4: Example of confusion matrix for a two–class problem.

many cases where the class assignment of the window actually occupies a small percentage of the window coverage. For these reasons, the cracks in this image prove to be very challenging for segmentation.

Methods of Analysis

Using the ground truth image, the cumulative correct and incorrect classifications for each test set are determined and stored in a *confusion matrix* [30]. For the two–class problem outlined in Table 5.4, A is the number of pixels correctly assigned to Class X, B is the number of pixels incorrectly assigned as Class X, C is the number of pixels incorrectly classified as Class Y, and D is the number of pixels correctly assigned to Class Y.

Using the confusion matrix, the producer's accuracy, user's accuracy, overall accuracy and overall error are determined (Equation 5.2). Producer's accuracy measures how well a particular class was identified during segmentation. The user's accuracy explains how correct the algorithm was at identifying a particular class. Overall accuracy and error represent the total correct and incorrect classification percentage respectively.

$$
\begin{aligned}
X_{producer} &= \tfrac{A}{A+C} \quad Y_{producer} = \tfrac{D}{B+D} \\
X_{user} &= \tfrac{A}{A+B} \quad Y_{user} = \tfrac{D}{C+D} \\
Accuracy &= \tfrac{A+D}{A+B+C+D} \quad Error = \tfrac{B+C}{A+B+C+D}
\end{aligned}
\tag{5.2}
$$

Amongst the analysis tools, the kappa ($\hat{\kappa}$) statistic and the confidence interval ($\hat{\sigma}$) are commonly used to evaluate the confusion matrix. The kappa statistic is a measure of the difference between the actual agreement between reference data and an automated classifier and the chance agreement between the reference data and a random classifier [30]. The kappa statistic has a range of $[-1, 1]$ with high values indicating strong separability. The confidence interval indicates the variability of the classifier [3]. Low confidence interval indicates a robust classifier. The kappa statistic and confidence interval are computed as follows:

$$\hat{\kappa} = \frac{N \sum\limits_{i=1}^{r} x_{ii} - \sum\limits_{i=1}^{r} (x_{i+} \cdot x_{+i})}{N^2 - \sum\limits_{i=1}^{r} (x_{i+} \cdot x_{+i})} \tag{5.3}$$

$$\hat{\sigma} = \frac{\sum\limits_{i=1}^{r} x_{ii}(N - \sum\limits_{i=1}^{r} x_{ii})}{N^2 - \sum\limits_{i=1}^{r} (x_{i+} \cdot x_{+i})} \tag{5.4}$$

where r is the number of classes in the confusion matrix, x_{ii} is the elements on the major diagonal, x_{i+} is the sum of the elements in row i, x_{+i} is the sum of the elements in column i, and N is the total number of observations in the matrix.

When two confusion matrices (segmentation algorithms) are compared, the following test statistic can be used to determine a significance value (using a significance level of 5%) [3].

$$Z \sim \frac{\hat{\kappa_1} - \hat{\kappa_2}}{\hat{\sigma_1} - \hat{\sigma_2}} \tag{5.5}$$

Results

Figures 5.7 and 5.8 show the segmentation results for test set 1 and 2 respectively. For both results, an edge map of the true boundaries (as determined from the ground truth image) are overlayed in red to provide a better indication of the segmentation performance.
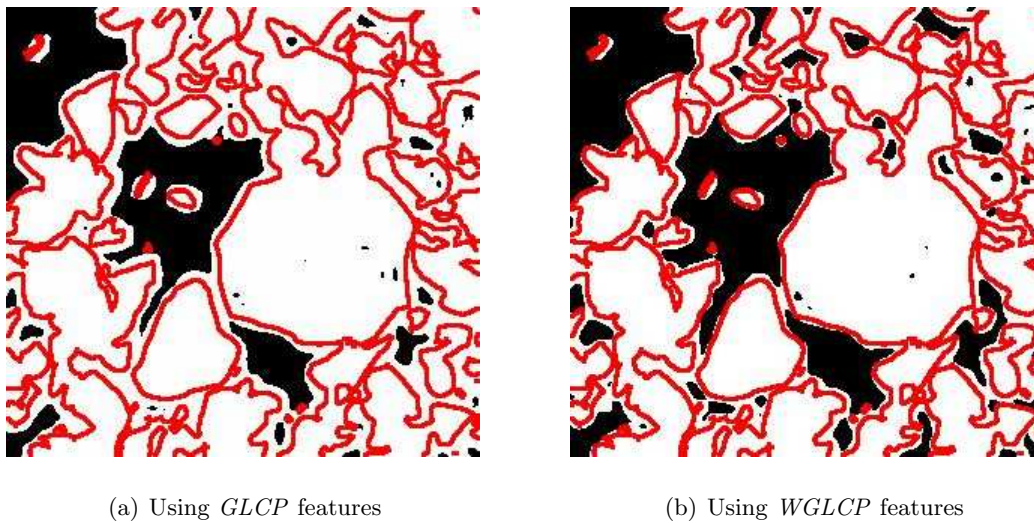
(a) Using *GLCP* features

(b) Using *WGLCP* features

Figure 5.7: Comparing *GLCP* and *WGLCP* features for SAR sea ice segmentation of Beaufort image (test set 1). True boundaries indicated by red.
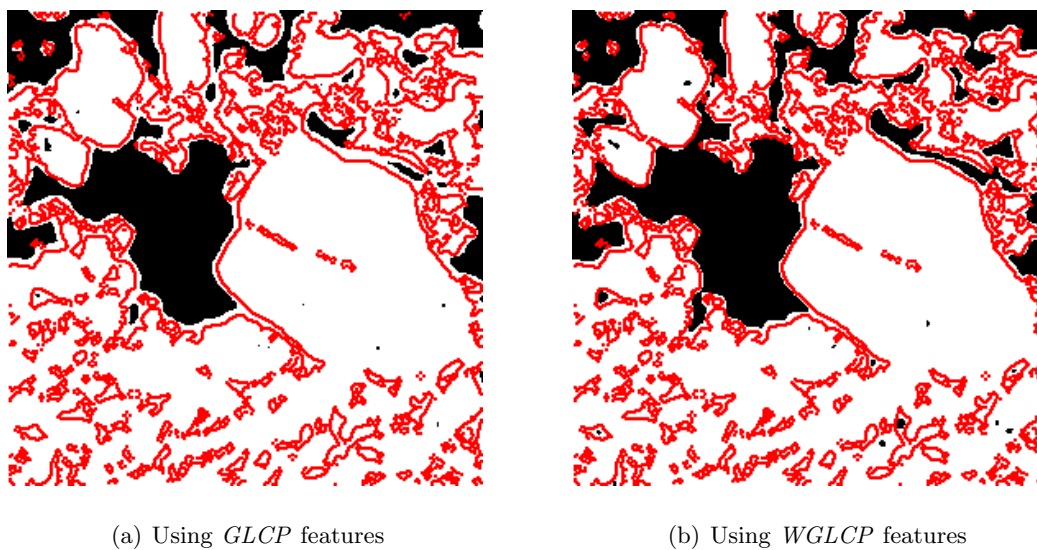

(a) Using *GLCP* features

(b) Using *WGLCP* features

Figure 5.8: Comparing *GLCP* and *WGLCP* features for SAR sea ice segmentation of Baffin image (test set 2). True boundaries indicated by red.

METRIC	test set 1		test set 2	
	GLCP	**WGLCP**	**GLCP**	**WGLCP**
Overall Accuracy (%)	73	79	82	85
Ice: Producer's Accuracy (%)	99	99	99	99
Ice: User's Accuracy (%)	68	74	78	82
Water: Producer's Accuracy (%)	36	51	47	57
Water: User's Accuracy (%)	99	99	99	99
Kappa Statistic	0.40	0.54	0.54	0.63

Table 5.5: Performance analysis for *GLCP* and *WGLCP* segmentation of test set 1 and 2.

By viewing the lower right quadrant of the Beaufort segmentation results (Figure 5.7), it is apparent that the *WGLCP* features perform better at segmenting regions close to boundaries. In general, there are fewer pixels incorrectly classified as water near boundary regions; this is reflected by a 15% increase producer's accuracy for water when using the *WGLCP* texture features. Table 5.5 lists all the accuracies for the Beaufort image (test set 1), and indicates that there was a 6% increase in the overall accuracy for the *WGLCP* feature set.

The Baffin Bay segmentation results (Figure 5.8) also display the same behaviors as Beaufort results. In general, *WGLCP* texture features perform better at segmenting regions close to boundaries. Formally, Table 5.5 indicates that there was a 3% increase in the overall accuracy when using the *WGLCP* features; however, both algorithms were still unable to detect the cracks in the lower portion of the image. This is a result of the effective window size being too large.

For both test sets, there is a significant increase in the user's accuracy for ice classification and the producer's accuracy for water classification. Both of these statistics are positively correlated and indicate that additional ice pixels were identified correctly while fewer water pixels were incorrectly assigned. As well, for both test sets, there was a significant increase in the kappa

statistic. Using the test statistic (Equation 5.5), the *WGLCP* segmentation results are said to be a statistically significant improvement compared to the *GLCP* results for both test sets.

5.1.3 Performance with Increasing Image Boundary Density

Explanation

Areas in images with high boundary density are difficult to segment using texture measures. As the boundary density of an image increases, the segmentation accuracy is expected to decrease at a relative rate. This section will compare the *GLCP* and *WGLCP* features with respect to robustness. Here, robustness is a measure of the ability for the feature set to discriminate images with high boundary density. Using the preferred *(W)GLCP* parameter set outlined above in Table 5.1, multiple images with increasing boundary density are interpreted and analyzed using unsupervised segmentation.

Test Data

The test data was synthetically created using textures from the Brodatz photo album [4]. The image sizes are fixed (252×252 pixels) and contain only two classes (*i.e.* textures) with a varying number of distinct regions. As the number of regions in the image increases, so does the boundary density. For example, Figure 5.9 illustrates an image with four distinct regions and its corresponding ground truth image. Because boundaries in SAR sea ice imagery have complex shape, the texture boundaries for this test set are selected to be sinusoidal with the frequency and amplitude dependant on the number of regions in the image. The only textures used were cork (D4) and wool (D92); they were adjusted to have the same mean grey level (DC shift with no information loss). The complete test set comprises thirteen images with a different number of regions (2, 4, 9, 16, 25, 36, 64, 81, 144, 196, 324, 441, 576). As the number of regions in the image increase, the size of each individual region will decrease. Given the number of regions in

(a) Cork–wool (4 regions)   (b) Template (4 regions)
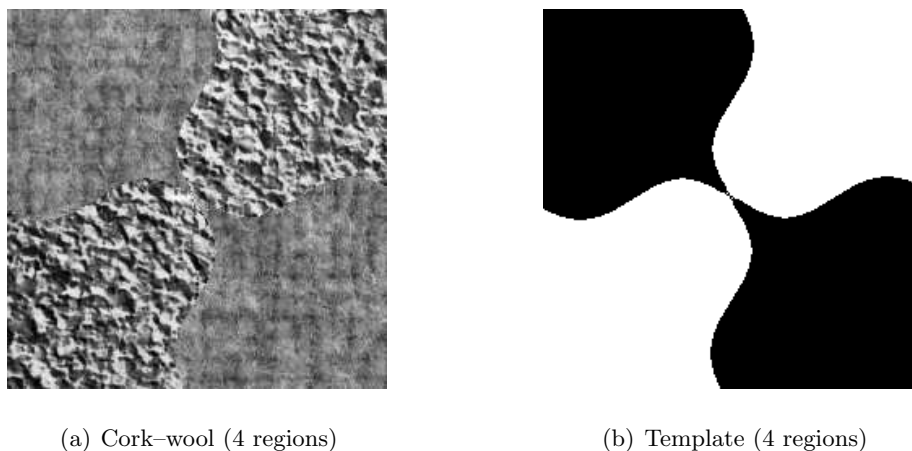
Figure 5.9: Brodatz test image with 4 regions.

an image, the boundary density is calculated by taking an edge map of the ground truth image, counting the number of pixels classified as an edge, then dividing by the total number of pixels in the image.

Methods of Analysis

Using the same analysis tools (*i.e.* user's/producer's/overall accuracy, kappa statistic, significance test) as in Section 5.1.2, the feature sets can be compared for each image in the test set. Aside from comparing the *GLCP* and *WGLCP* features on a per image basis, it is possible to show macroscopic trends across the images in the test set. One such trend is plotting the overall accuracy and kappa statistic as a function of increasing boundary. By doing this, one can compare the relative loss in segmentation performance for both *GLCP* and *WGLCP* feature sets. Generally speaking, the accuracy and kappa plots will have the same trends, hence, only a thorough discussion of the kappa statistic will follow in the discussion. Another excellent analysis tool of robustness is found by plotting the values of the Z–statistic (Section 5.1.2) as a function of increasing boundary density, which will show the relative increase in confidence of the *WGLCP* features.

Results

All graphical segmentation results for each image and a summary of analysis are found in Appendix A. For demonstrative purposes, Figures 5.10 and 5.11 contain the segmentation results for the 4– and 196–region images. When the boundary density in the image is low, the unsupervised segmentation results for both ($GLCP$ and $WGLCP$) feature sets perform well. In fact, the $WGLCP$ results are slightly more prone in producing regional errors; especially for images with low boundary density. This is apparent by the segmentation artefacts contained in the lower–right quadrant of the 2–, 4– and 25–region images in Appendix A and Figure 5.10 (for the 4–region image). However, since these regional misclassification artefacts are located at identical locations for the test images and only occur for the cork texture at a particular location, it indicates that they represent flaws in the image texture. Nonetheless, it proves useful by illustrating the noise sensitivity of $WGLCP$ features. To overcome the noise sensitivity issue, a larger standard deviation could be selected for $WGLCP$ method at the expense of poorer boundary preservation. Even with these noise artefacts, the $WGLCP$ features still slightly outperform the $GLCP$ features by providing more accurate segmentation near boundary regions.

In general, images with narrow texture regions are better segmentated with the $WGLCP$ feature set. This is visually observed from the graphical segmentation results in Figure 5.11. By giving more weight to pixel pairs near the center of the image window, the $WGLCP$ method is able to better discriminate these small–area, multi–class regions, which are abundant in SAR sea ice imagery. In fact, a significant improvement of the $WGLCP$ method with respect to the $GLCP$ method is demonstrated by the statistic test in Equation 5.5 for all test images.

Figure 5.12 illustrates plots of kappa statistic and Z–statistic as a function of boundary density. At relatively low boundary densities, both $GLCP$ and $WGLCP$ segmentation results have similar kappa values. As the boundary density increases, the $GLCP$ kappa value decays at a faster rate than the $WGLCP$ method, indicating that the $WGLCP$ features perform better un-

(a) Original Image

(b) Ground Truth Image

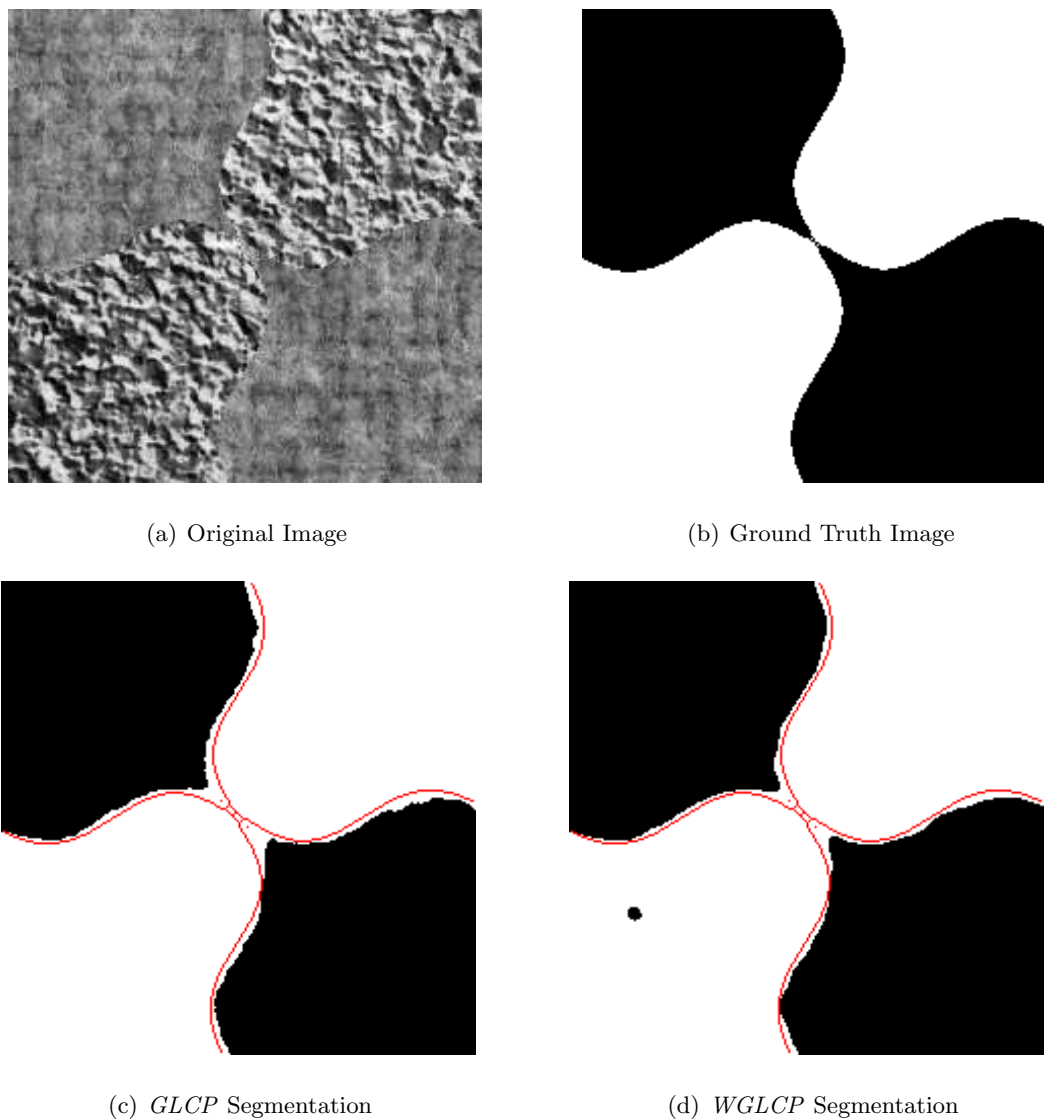(c) *GLCP* Segmentation

(d) *WGLCP* Segmentation

Figure 5.10: Graphical segmentation results of the Brodatz cork–wool image. There are 4 regions in this image. Included is the (a) original image, the (b) ground truth image, (c) unsupervised segmentation results using *GLCP* features, and (d) unsupervised segmentation results using *WGLCP* features.
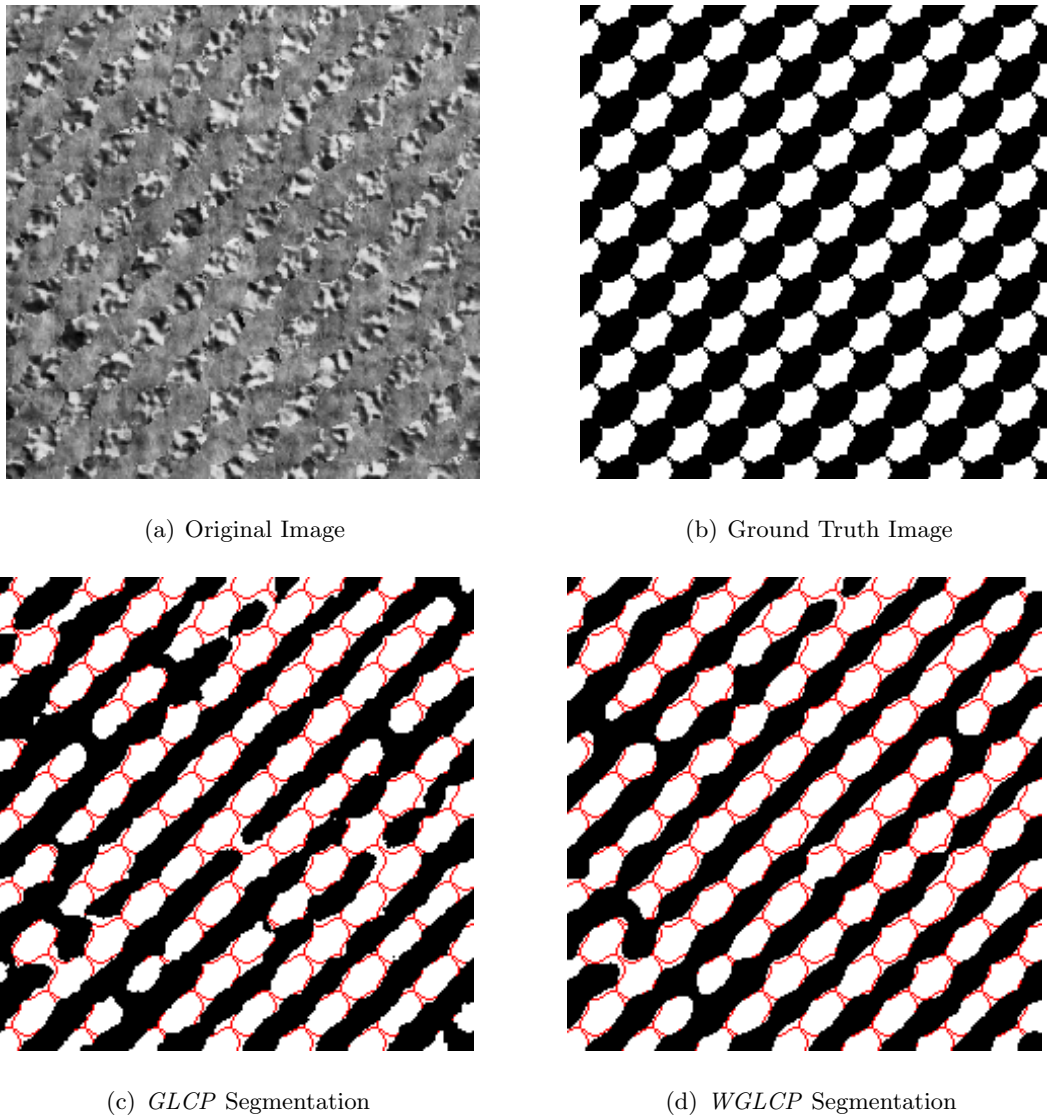
(a) Original Image

(b) Ground Truth Image

(c) *GLCP* Segmentation

(d) *WGLCP* Segmentation

Figure 5.11: Graphical segmentation results of the Brodatz cork–wool image. There are 196 regions in this image. Included is the (a) original image, the (b) ground truth image, (c) unsupervised segmentation results using *GLCP* features, and (d) unsupervised segmentation results using *WGLCP* features.
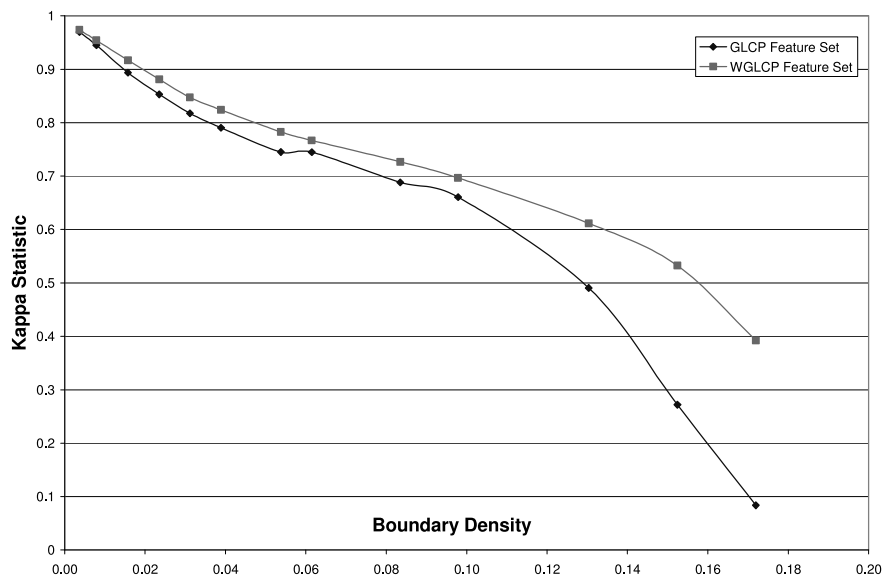
(a) Kappa statistic versus boundary density
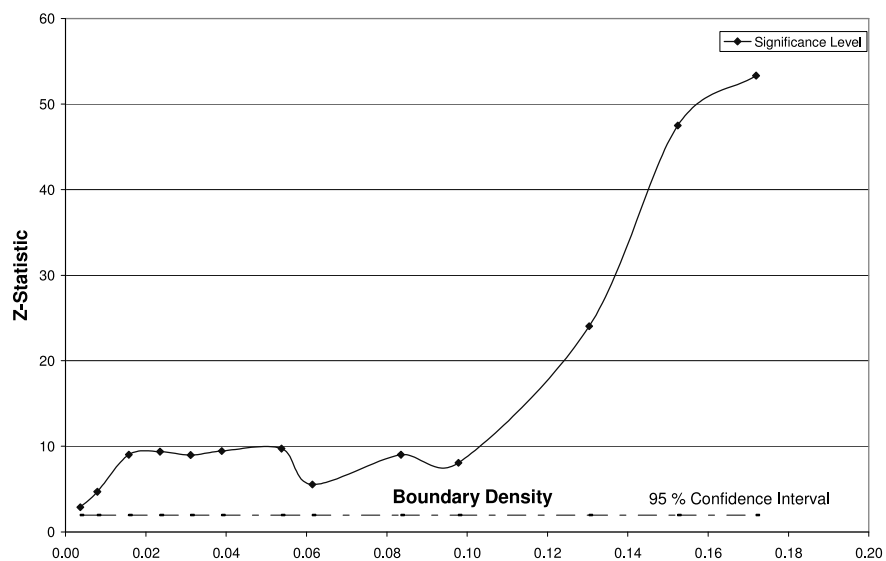
(b) Z–statistic versus boundary density

Figure 5.12: Performance measures as a function of increasing boundary density.

der more adverse conditions. Ultimately, the boundary density increases to a rate which makes the individual texture regions in the image smaller than the window size used for feature extraction. In this situation, the *GLCP* kappa value decreases at a non–linear rate of decay while the *WGLCP* kappa value decreases at a relatively stable, linear rate. This trend strongly indicates that the *WGLCP* feature set is more robust and stable than the *GLCP* feature set.

As mentioned, the improvement in results (*WGLCP* versus *GLCP*) is statistically significant for all images in the test set. Generally speaking, the Z–statistic increases with the boundary density when comparing feature sets. To illustrate, Figure 5.12 contains a plot of the Z–statistic versus boundary density, with the 95% confidence interval indicated by the dashed horizontal line. The Z–statistic remains fairly constant for relatively low boundary density. As the boundary density increases, there is a quick rise in the Z–statistic, indicating the *WGLCP* method is outperforming the *GLCP* method.

5.1.4   Computation Time

As with any automated algorithm, the length of time required to produce a result can be a major factor in determining usefulness. This section presents a comparison of the computation time required for each algorithm on the test data.

Historically, the co–occurring probabilities are stored in an inefficient sparse matrix known as the grey level co-occurrence matrix (*GLCM*). Statistics are applied to the *GLCM* to generate the texture features. This method is computationally expensive since the matrix is usually sparse leading to many unnecessary calculations involving zero probabilities when applying statistics. Recently, there have been advances in the computation time through the use of grey level co-occurring linked lists (*GLCLL*) [10] and the grey level co-occurrence hybrid structure (*GLCHS*) [12]. In contrast to the *GLCM* technique, these methods avoid storing zero probabilities for grey level pairs. In their publication for the *GLCHS* [12], Clausi and Zhao indicate that the *GLCHS*

is consistently faster than the *GLCLL* and orders faster than the *GLCM* method. For coarse quantizations and small window sizes, the *GLCHS* method runs at 37.7% the speed of the *GLCLL* method and 14.3 % the speed of the *GLCM* method, generating substantial computational savings.

The *WGLCP*s are stored in a *GLCM* data structure as there is no obvious way to calculate them using one of the hybrid data structures mentioned above. Currently, there has been no investigation if the weighted texture features can be calculated using a different data structure. For this thesis, the *GLCP* texture features were calculated using a modification of the *GLCHS* method, which is found in the PCI Geomatica$^{\text{TM}}$ software version 8. Table 5.6 shows the computation times required for the *GLCP* features using this method and the *WGLCP* features using the *GLCM* method. Both methods employed the user–defined parameter set outlined in Table 5.3. Computation times are reported in minutes, as measured on a Pentium IV, 1.6GHz computer running Windows 2000 and Matlab 6.1.0.450 Release 12.1 with 512MB RAM. In a sense, this is an unfair comparison as no investigation has yet been made to accelerate the *WGLCP* method. However, the results still indicate *WGLCP* features take considerably longer than the *GLCP* features by an order of magnitude.

Origin	Image Size	*GLCP*	*WGLCP*
Figure 5.10	252×252	14	686
Figure 5.6	300×300	17	741
Figure 5.5	313×330	19	762
Figure 4.1	429×223	22	784

Table 5.6: Computational requirements, in minutes, for algorithms based on image size. Computation times are reported in minutes, as measured on a Pentium IV, 1.6GHz computer running Windows 2000 and Matlab 6.1.0.450 Release 12.1 with 512MB RAM.

(a) Original Image   (b) Segmentation Results
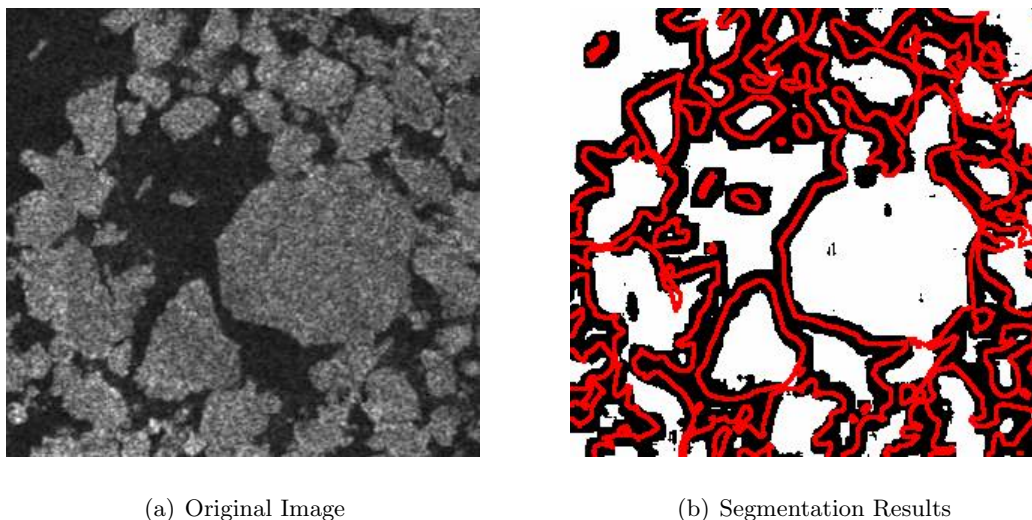
Figure 5.13: Segmenting image of Beaufort Bay using only *GLCP* correlation feature. *GLCP* user–defined parameters outlined in Table 5.3

5.2 *GLCP* Correlation Statistic Study

5.2.1 Overview

For *supervised* segmentation, the *GLCP* correlation statistic is advocated to improve SAR sea ice segmentation accuracy [7]. However, the experiment conducted in Section 5.1.1 indicates that the *GLCP* correlation statistic will not make a suitable feature for *unsupervised* segmentation. These results indicate that using correlation as a feature will separate boundary versus non–boundary rather than the relevant ice types in an image. This is re–affirmed by the segmentation results shown in Figure 5.13. For these results, the Beaufort image (introduced in Section 5.1.2) was segmented using only the *GLCP* correlation measures and k–means clustering. The true boundaries are indicated by the red line which is overlayed in the segmented image. It becomes very apparent that the *GLCP* correlation statistical features result in texture boundary detection for the SAR image, rather than separating relevant ice types.

The remainder of this section provides an in–depth analysis of the *GLCP* correlation statistical feature and its suitability for segmenting SAR sea ice. The first test involves analyzing some edge transects on synthetic bi–partite test imagery. By using synthetic imagery, texture characteristics remain controlled and the *GLCP* statistics become easier to analyze. The second test analyzes the *GLCP* feature space assuming labelled features. Using labelled features, it is possible to calculate Fisher distances, analyze probability distributions (*i.e.* histograms) for each feature, and investigate two–dimensional plots of the feature space.

5.2.2 Boundary Response for Synthetic Imagery

Explanation

The purpose of this experiment is to analyze the *GLCP* edge transects for various synthetic texture boundaries. By using synthetic test data, texture characteristics such as frequency, variance, mean grey level, *etc.* are controlled so the transect results can be generalized for different categories of textures. For example, the current hypothesis is that the *GLCP* correlation feature has poor performance across high contrast texture boundaries such as SAR ice–water. By developing synthetic bi–partite test images with these certain characteristics, generalizations can be made that are independent from any particular texture boundary.

The general procedure for determining edge transects is outlined in Section 5.1.1. This test employs the same methodology except only the *GLCP* statistics were used.

Test Data

The test data consists of two synthetic bi–partite textured images as shown in Figure 5.14. The textures were synthetically created from sinusoidal functions with a specified frequency, amplitude and DC gain. By varying these three parameters (frequency, amplitude, DC gain), different textural effects can be synthesized. As well, white Gaussian noise ($\sigma = 1.5$) was added
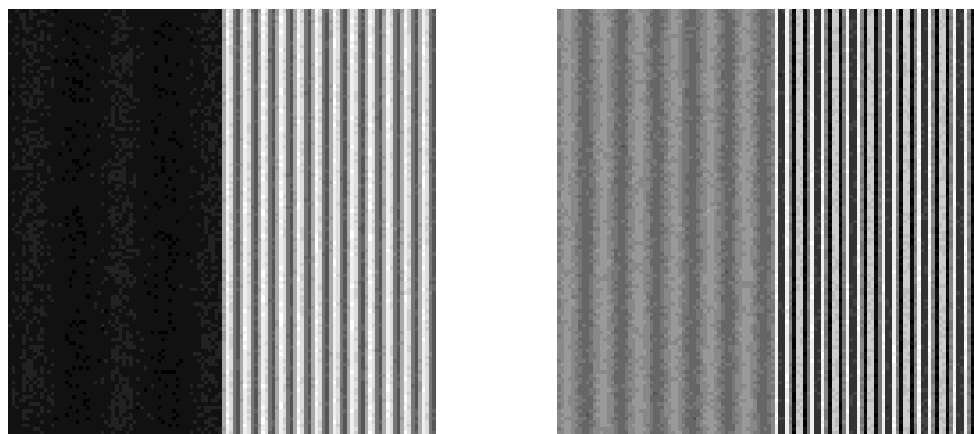
(a) Textures with different DC gain, different amplitude and different frequency.

(b) Textures with the same DC gain, different amplitude and different frequency

Figure 5.14: Synthetic bi–partite test images used for edge transects. The first image contains a high contrast texture boundary. The second image contains a low contrast texture boundary.

to each image in the test set to make the results more realistic. Each test image contains different texture pairs as follows:

1. Textures with different DC gain, different amplitude and different frequency

   The first texture was dark (*i.e.* low DC gain), had low variance (*i.e.* amplitude) and was of low frequency. This was to simulate the appearance of the water texture as it appears in SAR imagery. The second texture was brighter, had higher variance and higher frequency. This texture was simulating the appearance of ice in SAR. When combining these textures, a high contrast bi–partite image is formed.

2. Textures with same DC gain, different amplitude and different frequency

   As stated, both textures have the same mean grey level. The first texture has a low variance and frequency. The second texture had a high variance and frequency. For this bi–partite test image, there is no sharp contrast difference between the texture boundary.

This is similar to the appearance of first year rough ice and multi–year ice in SAR imagery. Typically, these textures will have similar mean grey levels, but different frequencies and variance.
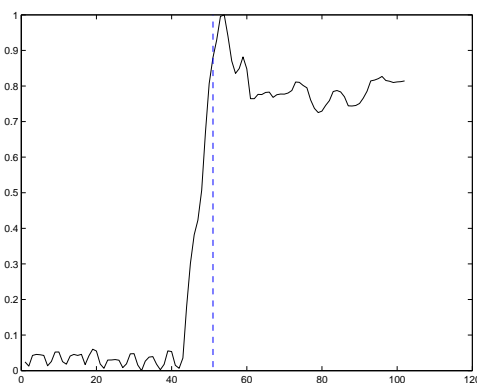
Results

Figure 5.15 contains the edge transect results for the high and low contrast images. The true texture boundary is indicated by the dashed blue line. The plots on the left–hand side are transects for the high contrast image. The plots on the right–hand side are transects for the low contrast image.

As expected, the entropy and contrast statistical features provide a step–like response across the texture boundary. This coincides with the previous research studies [35, 7, 1]. It is also noticeable that some of the feature values have a certain periodicity for the higher frequency textures. This is a result of having larger window sizes. However, smaller window sizes would result in even greater variance of the texture features as shown by Yue [40].

The impulse–like response of the *GLCP* correlation feature across high contrast texture boundaries can be explained through analyzing the probability distributions within the *GLCM*. During feature extraction, the distribution of non–zero elements in the *GLCM* was monitored within and across the texture boundaries. Figure 5.16 provides a general diagram of how the *GLCM* changes across the boundary. For the dark texture, there is a high distribution of non–zero elements concentrated in the upper–left quadrant of the *GLCM*. For the higher frequency bright texture, the bottom–right quadrant of the *GLCM* is more highly populated. During this transition from dark–to–light textures, the probability distribution migrates from the top–left quadrant to the bottom–right quadrant. As a result, the *GLCM* probability distribution becomes observably more correlated.
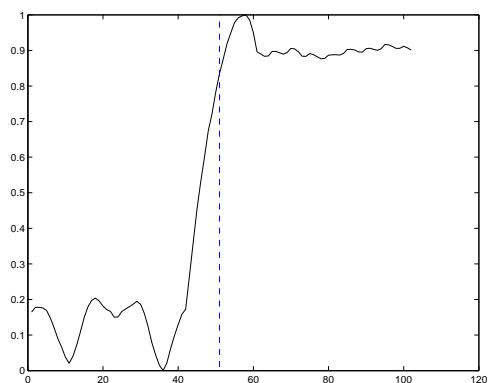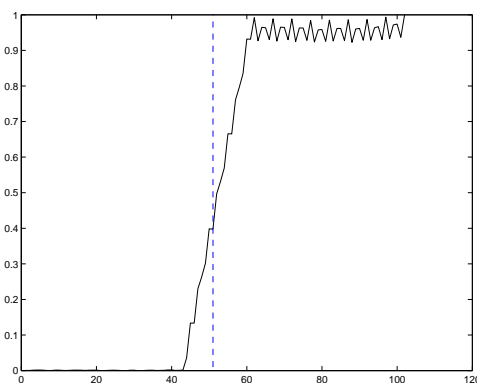
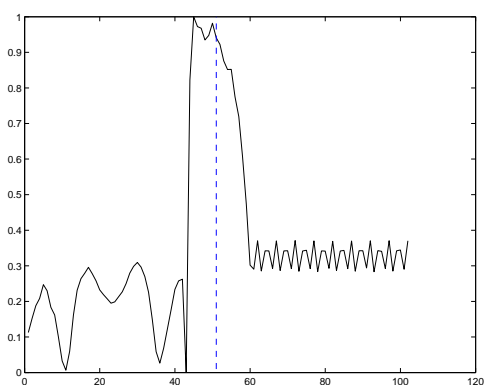(a) High contrast image: entropy results

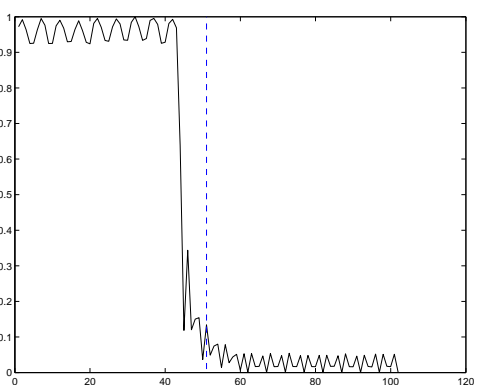(b) Low contrast image: entropy results
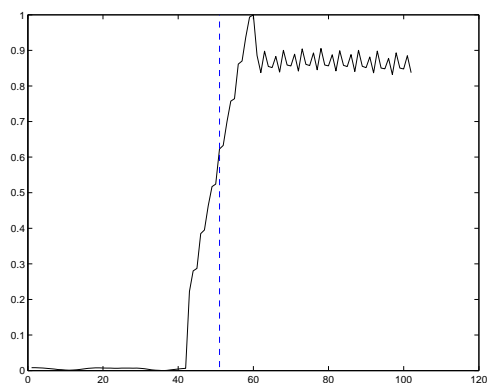
(c) High contrast image: contrast results

(d) Low contrast image: contrast results

(e) High contrast image: correlation results

(f) Low contrast image: correlation results

Figure 5.15: Edge transects for synthetic bi–partite imagery. The images on the left are the feature transects for high contrast image. The images on the right are the feature transects for low contrast image. The true texture boundary is indicated by the dashed blue line.
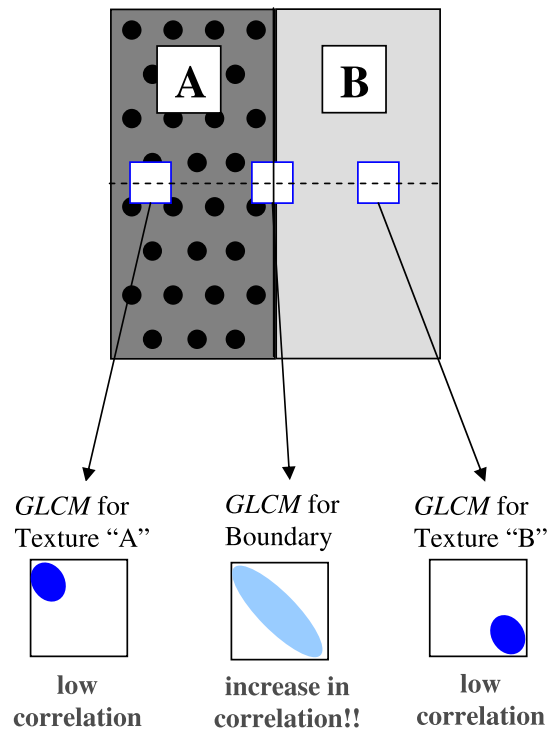
Figure 5.16: Visualization of how the probability distribution in the *GLCM* changes across high contrast texture boundaries. Texture "A" is has a low mean grey level and texture "B" has a high mean grey level. The probability distribution in the *GLCM* becomes more correlated as it crosses the texture boundary.

5.2.3 Labelled Feature Analysis

Explanation

Rather than separating relevant ice types in SAR imagery, correlation measures will tend to detect boundaries. Therefore, by using labelled features, one can perform analysis on the feature space to determine reasons for this poor unsupervised segmentation. For the SAR sea ice image in this test, the labelled feature space will comprise three relevant classes: ice, water and boundary. By calculating Fisher linear discriminants between the classes, one can determine the which pair of classes ('ice and water', 'ice and boundary', or 'water and boundary') have the greatest separability. As well, it is possible to verify the Fisher measurements by observing distributions and two–dimensional plots of the labelled feature space.

Test Data

The *GLCP* features are extracted from the Beaufort image (Figure 5.5) according to the parameter set in Table 5.3. Using the ground truth segmentation, one of three labels are assigned to each pixel in the feature space: ice, water or boundary. Due to the smearing effects of the large window sizes needed for *GLCP* feature extraction, a pixel is labelled boundary if its distance is at least $\lceil \frac{1}{4} \cdot n \rceil$ pixels from a true boundary; where n is the size of the image window, and the true boundary is determined from the ground truth image. For example, using a window size of 15×15, any pixels that are at least a distance of $\lceil \frac{1}{4} \cdot n \rceil = \lceil \frac{1}{4} \cdot 15 \rceil = 4$ pixels from the true boundary are labelled boundary as well.

Methods of Analysis

To adequately determine the properties of the labelled feature space, three methods of analysis will be performed. The first method involves calculating cluster separability using the Fisher

criterion [17]. The second and third tests are qualitative visualizations to support the Fisher results and better understand the nature of the feature space.

The distance between two clusters is a common measurement in determining cluster separability. However, if the feature space dimension is larger than three, the distance measurement becomes difficult to visualize. Using the Fisher criterion, one can project n dimensional feature data onto a line ω and calculate a weighted distance between the projected clusters [14]. Essentially, determining the Fisher criterion for two labelled classes (C_1 and C_2) in the feature space, the ratio of the between–class scatter matrix (S_B) and within–class scatter matrix (S_W) is used as follows [17]:

$$J = tr(S_W^{-1}S_B) \tag{5.6}$$

where tr denotes trace. Based on the sample data for each class in the feature space, the following relations for S_B and S_W hold true:

$$S_B = P_1(m_1 - m_0)(m_1 - m_0)^T + P_2(m_2 - m_0)(m_2 - m_0)^T \tag{5.7}$$

$$S_W = P_1\Sigma_1 + P_2\Sigma_2 \tag{5.8}$$

where, P_i is the *a priori* probability of class i,

   m_i is the mean of class i,

   Σ_i is the covariance matrix of class i,

   $m_0 = P_1m_1 + P_2m_2$.

Using Equation 5.6, larger values of J indicate greater cluster separability. The Fisher criterion is used to determine cluster separability between the following pairs of classes: ice and water, ice and boundary, water and boundary. Essentially, the pair with the highest value of J for the given feature space is deemed the most separable cluster pair.

The second and third tests are designed to visually support the results of the Fisher analysis. In these tests, distributions and two–dimensional plots of the feature space will be observed for the reader to gain a better understanding of the correlation statistic within the feature space. The second test will analyze the histograms of the various *GLCP* statistical features. By analyzing the distribution of a feature for each class in the feature space, one can visually determine which two class distributions appear most separable. The third test will provide some two–dimensional plots of the feature space using various *GLCP* features. The statistical features (entropy, contrast, correlation) will be plotted against one another (entropy vs. contrast, entropy vs. correlation, contrast vs. correlation) and observed. In typical situations, the boundary features will be within the range of the ice and water classes. That is, within the feature space, the boundary features will be located between the ice and water features. In situations where the boundary features are outside the range of the ice and water features, they will skew the ice–water decision boundary, resulting in poor segmentation.

Results

Using the Fisher criterion, the cluster separability between ice, water and boundary classes is determined. Table 5.7 summarizes the results of Fisher analysis on different feature spaces. For example, according to the Fisher criterion, when the feature space comprises only the entropy statistic, the ice–water separability is relatively higher (4.21) than the other class pairs, indicating that the ice and water pixels are more easily segmented. However, for this situation, the ice–boundary separability is very low (0.08), indicating that there is a bias which will group ice and boundary pixels together, even in situations where the boundary pixel should be classified as water. The results also show that a feature space containing only entropy or only contrast have similar characteristics in terms of inter–class separability.

The Fisher results also indicate that the hypotheses regarding the correlation statistic were

	Statistics Used In Feature Space				
	entropy	contrast	correlation	entropy, contrast, correlation	entropy, contrast
Ice vs. Water	4.21	2.74	0.50	12.55	15.01
Ice vs. Boundary	0.08	0.39	1.82	1.83	0.45
Water vs. Boundary	2.57	1.00	0.71	2.87	2.72

Table 5.7: Fisher measures for various feature spaces of the Beaufort image.

correct; that is, a feature space comprised only of the *GLCP* correlation statistic will separate boundary versus non–boundary, rather than relevant ice types. The Fisher criterion indicates ice and boundary have the highest separability at 1.82 units, whereas ice–water and water–boundary have Fisher values of 0.50 and 0.71 respectively. This indicates that ice and water classes will be indistinguishable during segmentation and boundary pixels will form a distinct class. These results also coincide with the segmentation results illustrated above in Figure 5.13, where the correlation statistical feature resulted in texture boundary detection.

When all three statistics (entropy, contrast, correlation) are combined, the Fisher criterion shows greatest separability between ice and water classes. Also, for this scenario, the ice–boundary classes have a relatively lower separability than water–boundary classes (1.83 versus 2.87), indicating that there is a slight bias to over–classify boundary pixels as ice. Finally, when the correlation statistical feature is removed from the feature space, ice and water pixels have a higher separability (15.01 versus 12.55). However, this scenario indicates that the bias to misclassify the boundary pixels as ice still exists.

For the remaining tests in this section, each *GLCP* statistic (entropy, contrast, correlation) was averaged over all the displacements to produce directionally invariant features. To support the results of the Fisher criterion and provide a visualization of the feature space, a histogram
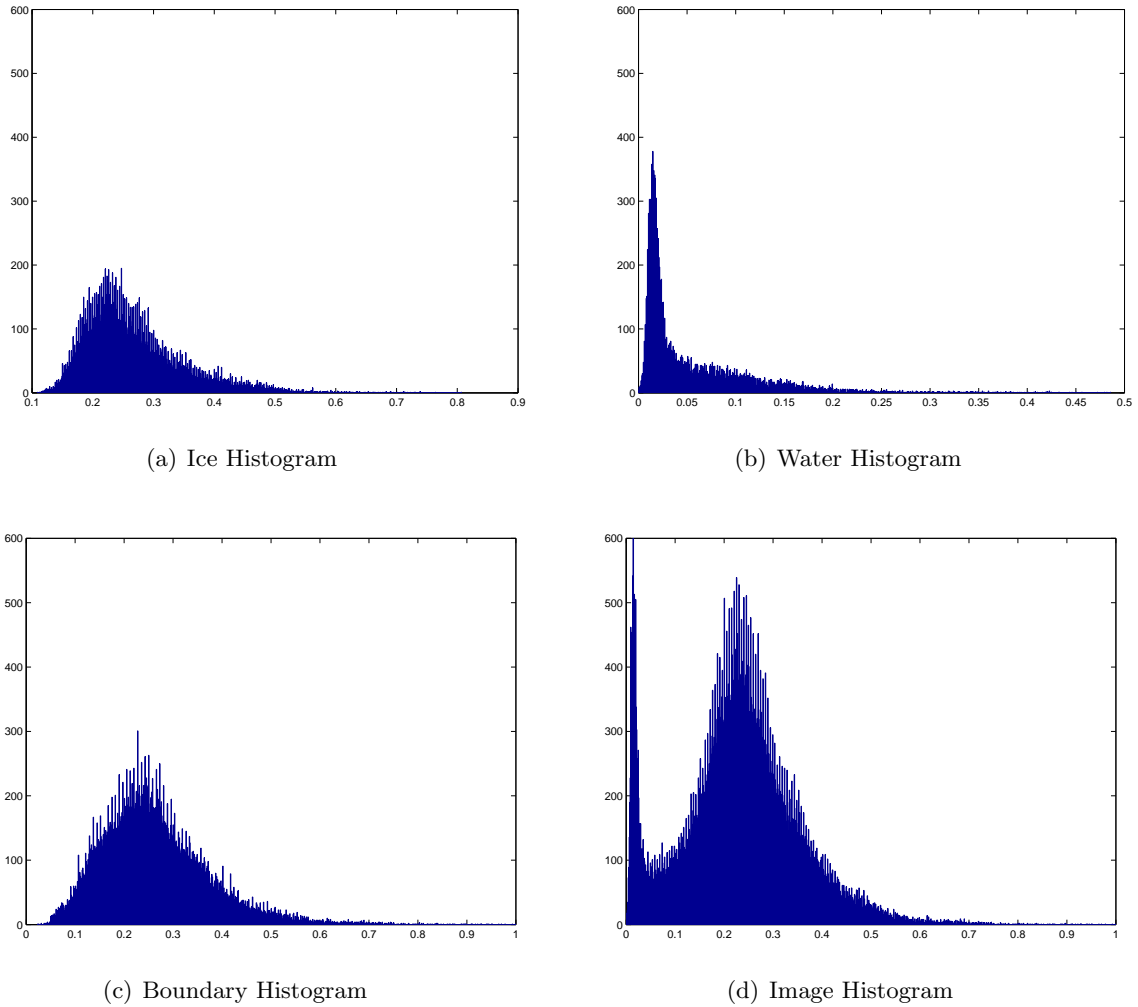
(a) Ice Histogram

(b) Water Histogram

(c) Boundary Histogram

(d) Image Histogram

Figure 5.17: Histograms of *GLCP* contrast statistic for each class in the Beaufort Sea image.

(a) Ice Histogram

(b) Water Histogram

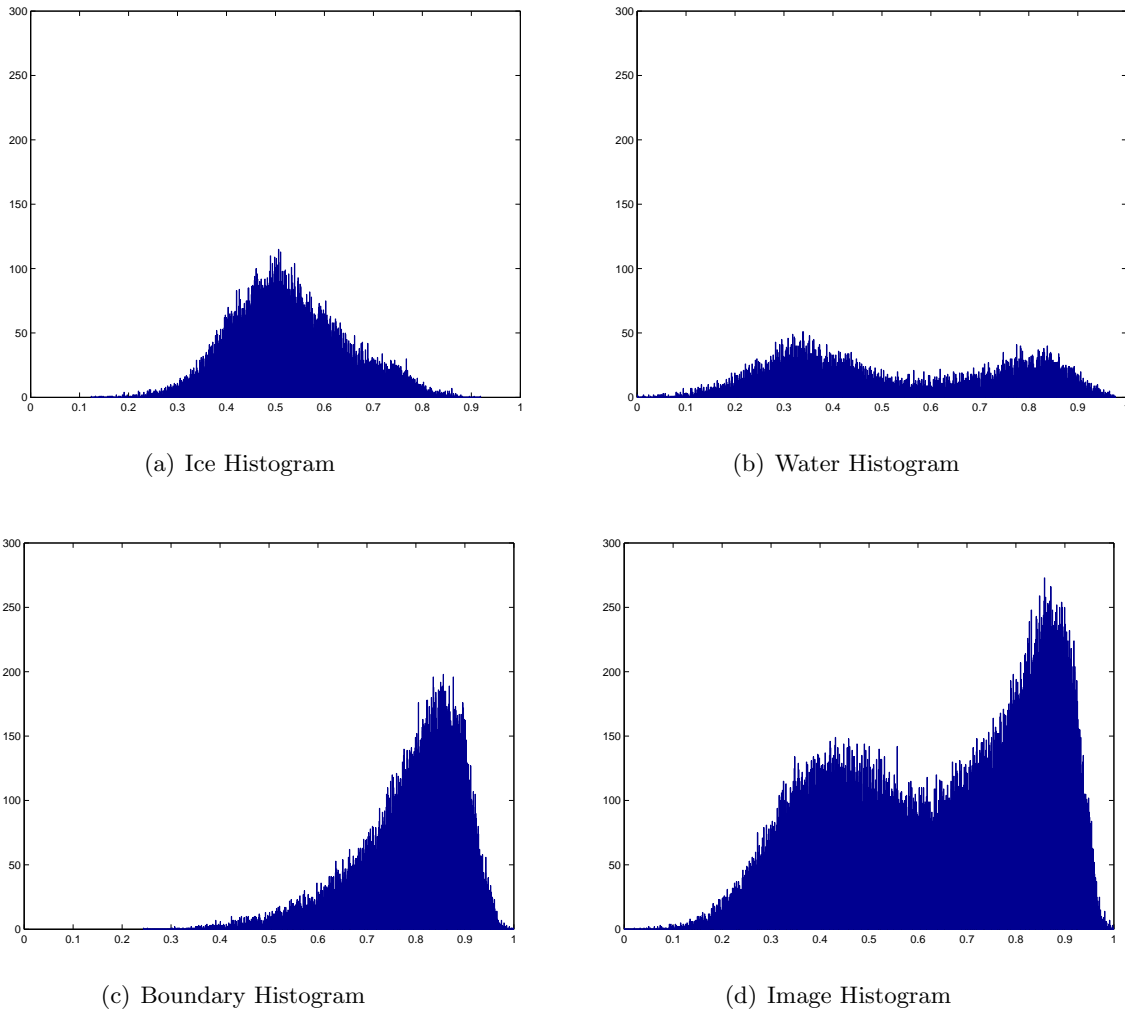(c) Boundary Histogram

(d) Image Histogram

Figure 5.18: Histograms of *GLCP* correlation statistic for each class in the Beaufort Sea image.

is taken of the *GLCP* contrast and correlation statistical features. The entropy histogram was omitted as it exhibits similar behavior to the contrast results. By viewing the feature distributions for each class (ice, water, boundary) and the entire image, it is easy to visualize the contribution that each class has to the overall feature separability. Figure 5.17 and 5.18 show the histograms for contrast and correlation statistical features respectively. Observing the results for contrast, the histograms for ice and water have distinct distributions, making it easy to distinguish the two textures from the image histogram. The ice and boundary histograms have very similar distributions and become indistinguishable in the image histogram. These visual interpretations agree with the Fisher measures for contrast, which indicate that the ice–water pixels have high separability and the ice–boundary pixels have very low separability. The correlation histograms also agree with the Fisher results. According to the histograms, ice and boundary seem to be the most dominant and separable clusters, while the water histogram appears to be a mixture of ice and boundary. Employing a thresholding scheme for the correlation image histogram would result in separating ice and boundary, as indicated above by the Fisher criterion.

Another method to visually determine the nature of the *GLCP* correlation statistic is to plot the feature space. Using the directional invariant statistical features (entropy, contrast, correlation), two–dimensional plots of the feature space were analyzed. Figure 5.19 shows various two–dimensional plots of the feature space which include and omit the presence of the boundary pixels. In these images, the blue, red and green colours represent water, ice and boundary features respectively. Viewing the results, the following statements can be made about each plot:
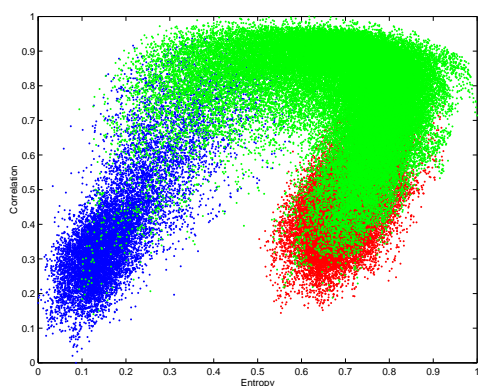
- entropy versus contrast

  The feature space appears to be highly correlated, indicating the necessity for principle components analysis (PCA) when applying this problem to supervised segmentation. As well, the feature space indicates that the boundary class is a mixture of the ice and water
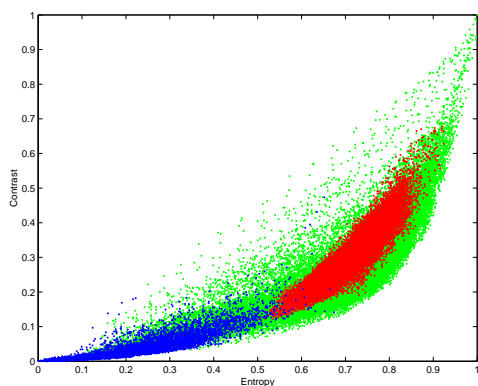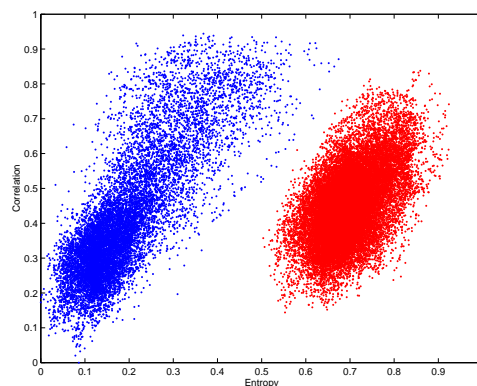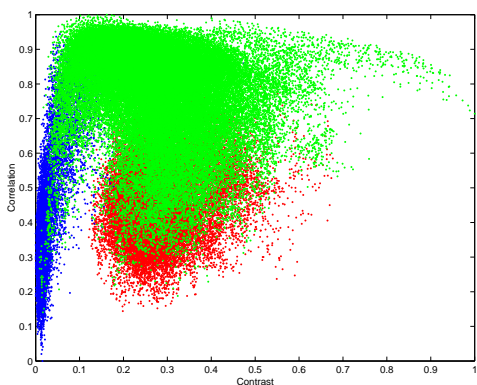
(a) Entropy vs. Contrast
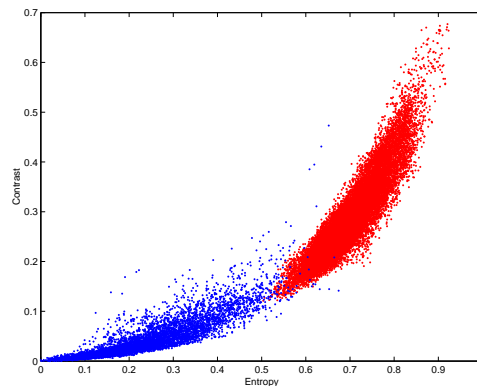
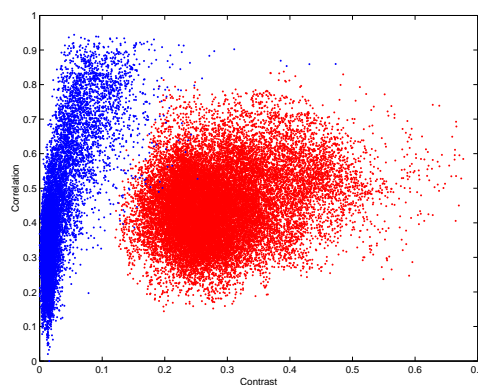(b) Entropy vs. Contrast (boundary features omitted)

(c) Entropy vs. Correlation

(d) Entropy vs. Correlation (boundary features omitted)

(e) Contrast vs. Correlation

(f) Contrast vs. Correlation (boundary features omitted)

Figure 5.19: Two–dimensional plots of the feature space for the Beaufort image. Red represents ice, blue represents water, green represents boundary.

classes, implying that the boundary pixels are not likely to form a distinct third class during segmentation. Also by viewing the figure, it apparent that the boundary pixels are also biased towards the ice class, indicating that a ice–water decision boundary would most likely over–assign boundary pixels as ice. Figure 5.19 also illustrates the appearance of the feature space in an ideal (yet unrealistic) scenario where the boundary pixels are removed from the image. After removal, the feature space appears much more easy to segment with very little overlap between the ice and water clusters.

- entropy versus correlation

  The pixels labelled as boundary are spread across the ice and water classes. There is a high percentage of boundary pixels that overlap with the ice region in the feature space. Using this feature space, ice and water are still the dominant clusters, however, there appears to be a large bias to over–classify pixels near boundaries as ice. This verifies the results provided by the Fisher analysis. Again, if the boundary pixels were removed from this image, the remaining ice and water clusters appear very distinct and easily separated.

- contrast versus correlation

  This graph exhibits similar behavior as entropy versus correlation plot. From this plot, the most likely decision boundary would result in distinct ice and water clusters. Again, there appears to be a bias for the boundary pixels to be misinterpreted as ice. Also, if the boundary pixels were removed, the resulting ice and water clusters are very easily separated.

5.3   Towards Improving SAR Sea Ice Segmentation Ability

In this section, the concepts developed in the previous experiments are used to improve image segmentation with a focus on SAR sea ice imagery. Thus far, two hypotheses were developed

and tested individually. The first hypothesis demonstrates that *WGLCP* texture features provide better texture boundary preservation, segmentation ability and robustness (to increasing boundary density) compared to the standard *GLCP* features. The second hypothesis demonstrates that the *GLCP* correlation statistical feature is not a suitable feature for the segmentation of high contrast images, such as SAR sea ice imagery. Combining these hypotheses, a preferred feature set is experimentally determined for image segmentation. This test comprises of the following four combinations for segmenting a variety of imagery:

1. *GLCP* texture feature extraction using entropy, contrast, correlation statistics.

2. *GLCP* texture feature extraction using entropy and contrast (no correlation) statistics.

3. *WGLCP* texture feature extraction using entropy, contrast, correlation statistics.

4. *WGLCP* texture feature extraction using entropy and contrast (no correlation) statistics.

After each feature set is extracted, the feature space is normalized and k–means clustering is applied with k set equal to the number of distinct classes in the image. Aside from the statistical features, each feature set employed the same user–defined parameters as outlined in Table 5.8. Based on the experiments conducted in the previous sections, the hypothesis is that feature set #4 (*i.e. WGLCP* using entropy and contrast statistics) should provide the best segmentation results for the high contrast (SAR sea ice) images used in this section. It should be noted that adding grey tone to the feature space for high contrast images would improve segmentation. However, these tests are focussed on comparing the feature sets with respect to one another, therefore, grey tone was not added to the feature space.

(W)GLCP Parameters	Values
Displacement Vector	(1,0), (1,1), (0,1), (-1,1)
Quantization	32 levels
Window Size	15×15 or 19×19
Standard Deviation	$\frac{n}{4} = 4.75$ (for *WGLCP* only)

Table 5.8: Textural parameters used for testing in Section 5.3.

5.3.1   Beaufort Sea Image

This image was first introduced in Section 5.1.2 on page 54 and is from the Radarsat–1 platform. The parameters in Table 5.8 were used with a window size of 15×15 for feature extraction. The image contains sea ice and open water (*i.e.* $k = 2$) and is considered to be of relatively high contrast. As a result, feature set #4 (*WGLCP* features omitting correlation) is expected to provide the highest segmentation accuracy.

Figure 5.20 shows the segmentation results using the four feature sets. Again, the red lines overlayed in the image represent the true boundaries. By viewing the figures for the *GLCP* feature set, omitting the correlation statistical feature provides better segmentation. In fact, the segmentation accuracy increases from 72.9% to 77.0% when removing the correlation feature (as determined from the ground truth image) from the *GLCP* feature set. As well, using a 95% confidence interval, the results are considered statistically significant. This is observed by an increase boundary classification for the image.

Observing the *WGLCP* feature set segmentation results (Figure 5.20), there appears to be no noticeable change in segmentation accuracy. The segmentation accuracy increases subtly from 79.1% to 79.3% when omitting the correlation feature. When comparing these results, they are deemed to be not statistically significant indicating the results are similar. Overall, when using the *WGLCP* features, the correlation statistical feature does not have a positive or negative
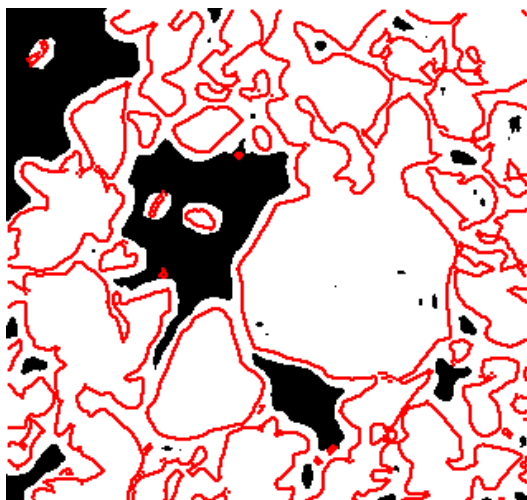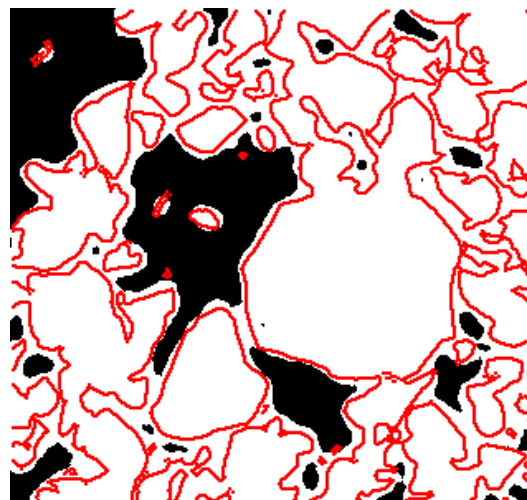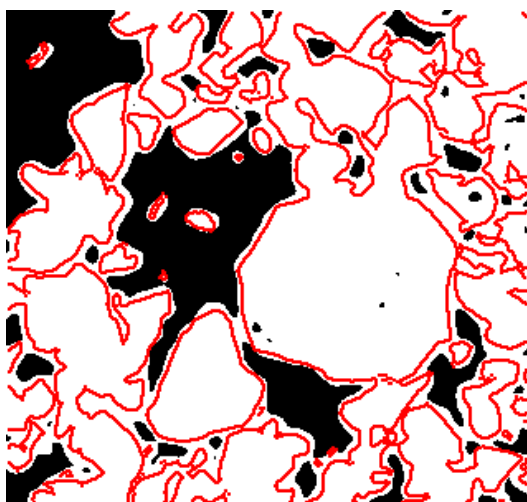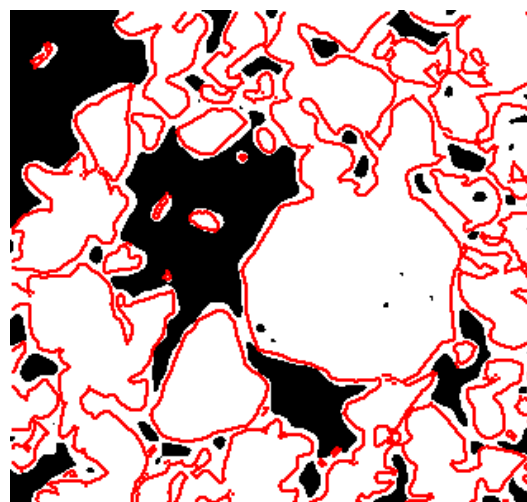
(a) *GLCP* using entropy, contrast, correlation

(b) *GLCP* using entropy and contrast

(c) *WGLCP* using entropy, contrast, correlation

(d) *WGLCP* using entropy and contrast

Figure 5.20: Segmentation of Beaufort Sea image in Figure 5.5, page 54. Red lines represent true boundaries as obtained from the ground truth image.

	Feature Set 1	**Feature Set 2**	**Feature Set 3**	**Feature Set 4**
Overall Accuracy (%)	72.9	77.0	79.1	79.3
Kappa Statistic	0.39	0.49	0.54	0.54

Table 5.9: Comparing segmentation performance of different feature sets for the Beaufort Image.

impact on segmentation accuracy. This is caused by the *WGLCP* features being inherently better at boundary preservation. As a result, fewer misclassifications occur near boundaries and the correlation feature has very little impact in this scenario.

5.3.2 Mould Bay Image

Used in Section 4.1, this test image is from the STAR–1 platform. Land cover and three ice types are included in the image. The ice types are first year smooth (FYS) ice, first year rough (FYR) ice and multi–year ice (MY). A window size of 15×15 is employed for feature extraction and $k = 3$ for the k-means algorithm. The land cover is masked (and omitted) during segmentation because the location of land cover can be obtained from appropriate land maps in a GIS (Geographical information systems) environment.

Figure 5.22 and 5.23 show the results of segmentation using *GLCP* and *WGLCP* feature sets including and omitting the correlation statistic respectively. It is apparent in Figure 5.22 for the *GLCP* feature set, omitting the correlation statistical feature provides better segmentation. When correlation is included, FYS ice is confused with FYR ice. In fact, the pixels classified as FYR ice are actually indicators of the boundary between FYS and MY ice. After removing the correlation statistic from the feature set, the *GLCP* segmentation results are more accurate.

For this image, the *WGLCP* feature set provides better segmentation compared to the *GLCP* feature set. Generally, one can observe that the *WGLCP* method is able to locate different
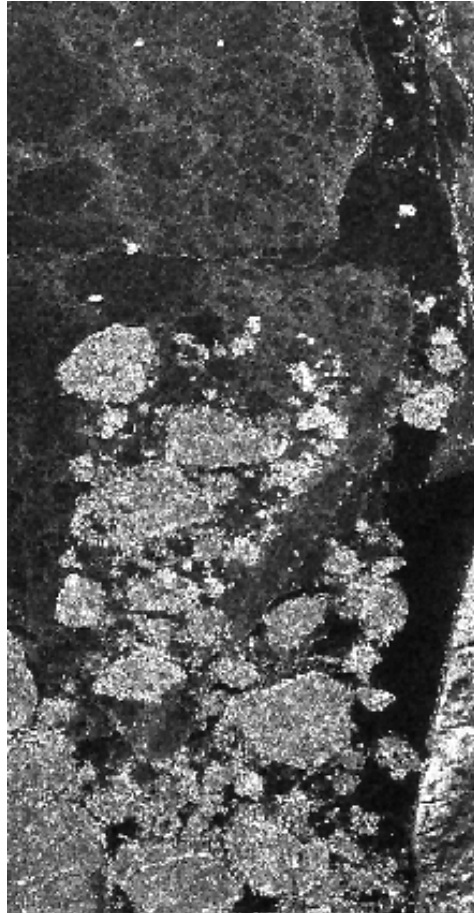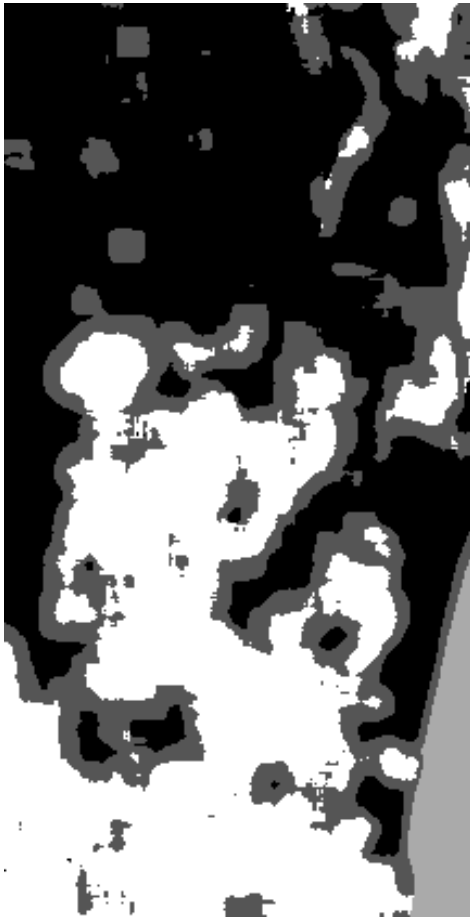
Figure 5.21: STAR–1 image of Mould Bay, NWT (March 1984). Image contains land cover and three ice types: FYS, FYR and MY.
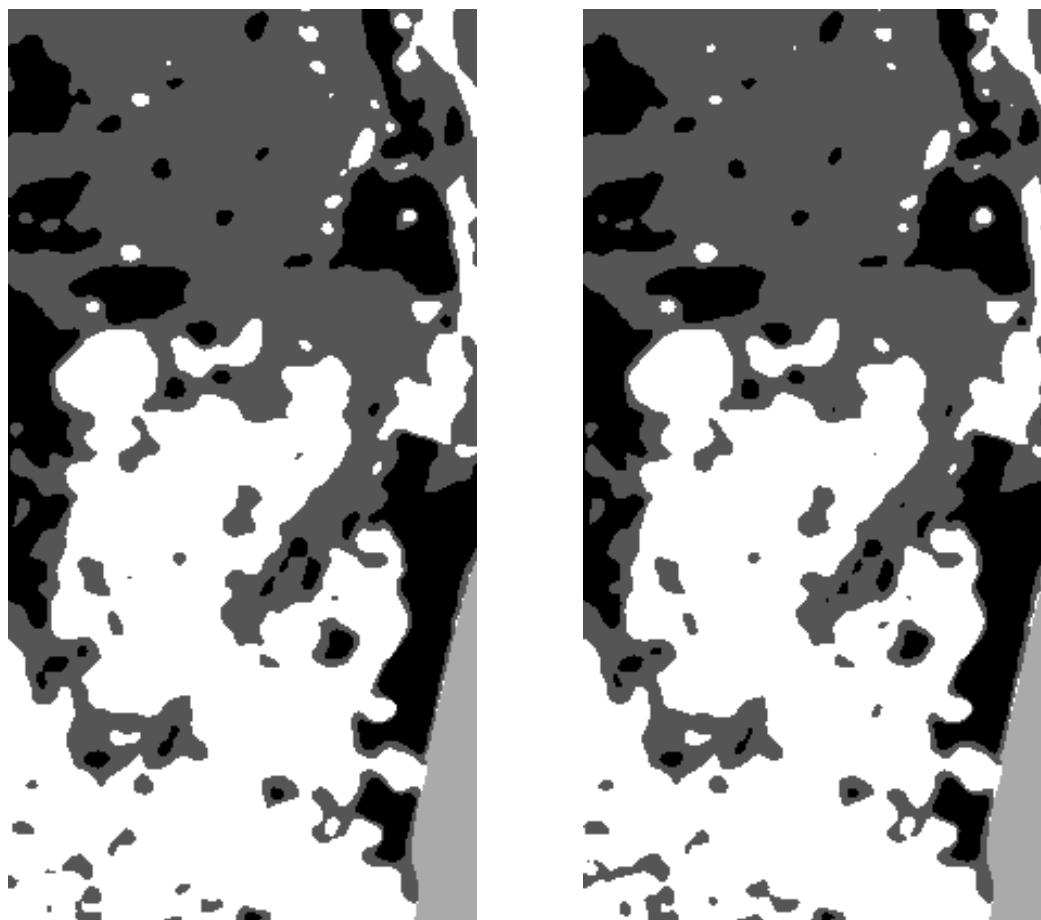
(a) *GLCP* using entropy, contrast, correlation

(b) *GLCP* using entropy and contrast

Figure 5.22: *GLCP* segmentation of STAR–1 image in Figure 5.21. FYS ice labelled black, FYR ice labelled dark grey, MY ice labelled white and land cover labelled light grey.

(a) *WGLCP* using entropy, contrast, correlation

(b) *WGLCP* using entropy and contrast

Figure 5.23: *WGLCP* segmentation of STAR–1 image in Figure 5.21. FYS ice labelled black, FYR ice labelled dark grey, MY ice labelled white and land cover labelled light grey.

ice types that are present within the MY ice flow. For example, by observing the middle–left region of the results, the *WGLCP* method provides a better indication of disjoint regions of MY ice whereas the *GLCP* method incorrectly merges these regions together.

Amongst both *WGLCP* feature sets in Figure 5.23, there is very little variation in the segmentation results when including and omitting the correlation feature. Since the *WGLCP* features provide better boundary preservation, it is expected that the correlation statistical feature influences fewer pixels near texture boundaries, hence, having less impact on segmentation.
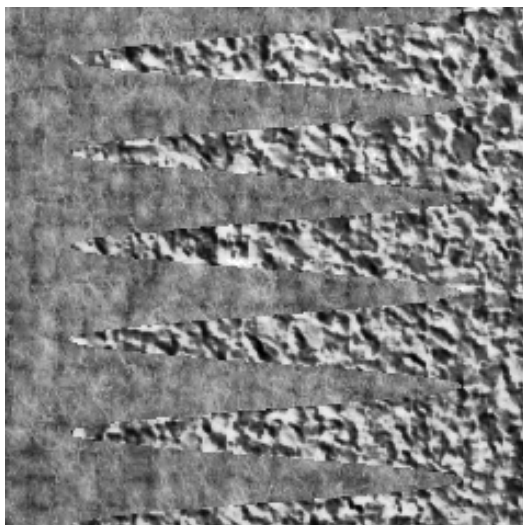
5.3.3   Bi–partite Brodatz Images

Figure 5.24 shows the bi–partite test images and their corresponding ground truth image used in this section. These images contain two textures from the Brodatz photo album and are separated by a high amplitude, high frequency sinusoidal boundary. The first image uses the cork (D4) and wool (D92) textures similar to Section 5.1.3. Both textures were adjusted to have the same mean grey level (same DC gain with no information loss). The second image uses cork (D4) and straw matting (D78) textures. In this image, the straw matting texture has a higher mean grey level (175 for straw matting and 119 for cork) than cork. A window size of 19×19 is employed for feature extraction and $k = 2$ for the k-means algorithm.

Figure 5.25 and 5.26 show the segmentation results for each feature set of the cork–wool and cork–straw matting images respectively. For all images, the true texture boundary is overlayed in red. In Figure 5.25 for the cork–wool image, the difference in segmentation accuracy is not very noticeable when the correlation feature is removed. Although not noticeable, Table 5.10 indicates a slight increase in accuracy when the correlation feature is removed. However, the improvement in accuracy is deemed to be not statistically significant. The reason the effects are subtle is because both textures have a similar mean grey level. As the contrast difference between textures increase, the effects become more apparent. As expected, there is a statistically
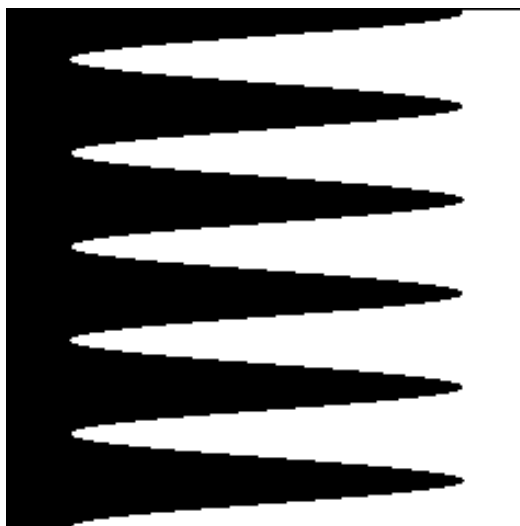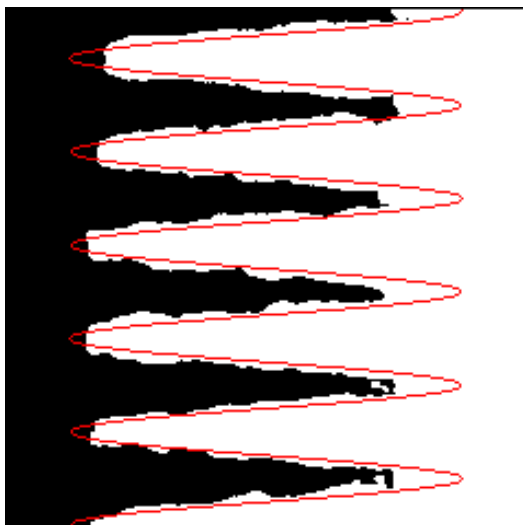
(a) Ground truth image

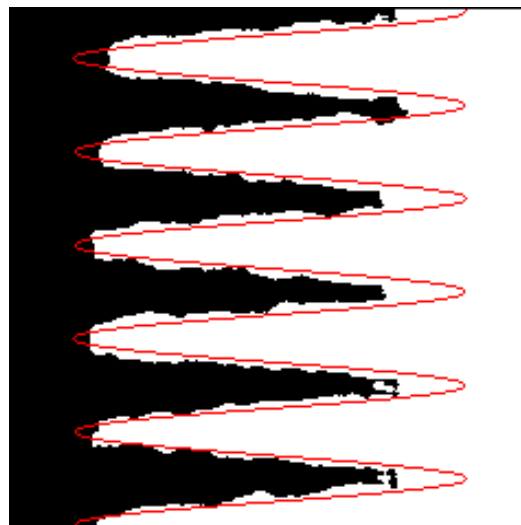(b) Cork–wool bi–partite image
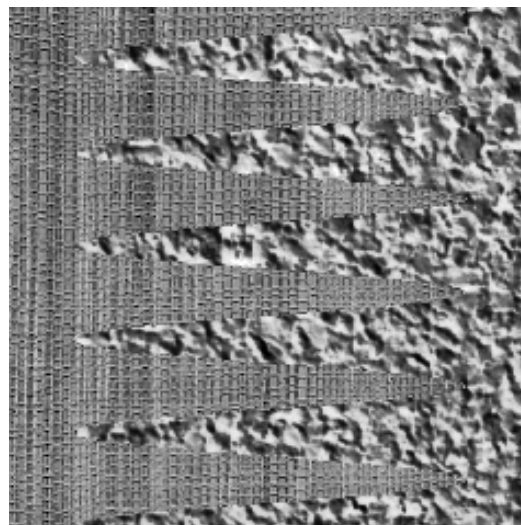
(c) Cork–straw matting bi–partite image

Figure 5.24: Bi–partite Brodatz Images.

(a) *GLCP* using entropy, contrast, correlation

(b) *GLCP* using entropy and contrast

(c) *WGLCP* using entropy, contrast, correlation

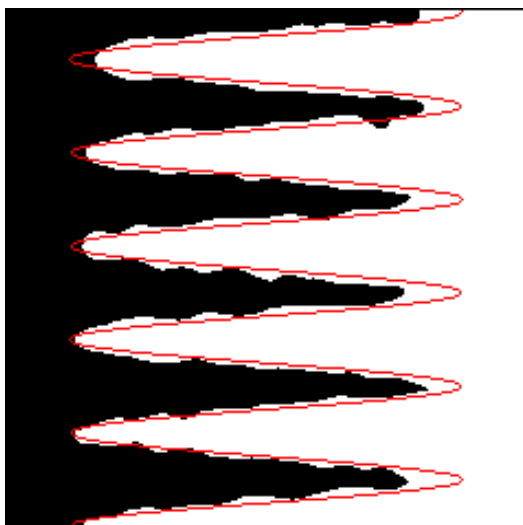(d) *WGLCP* using entropy and contrast

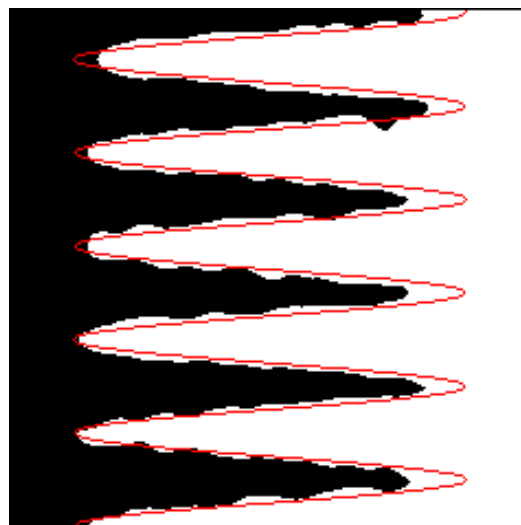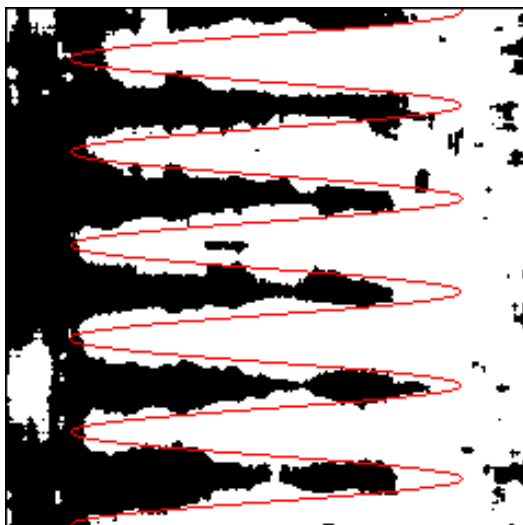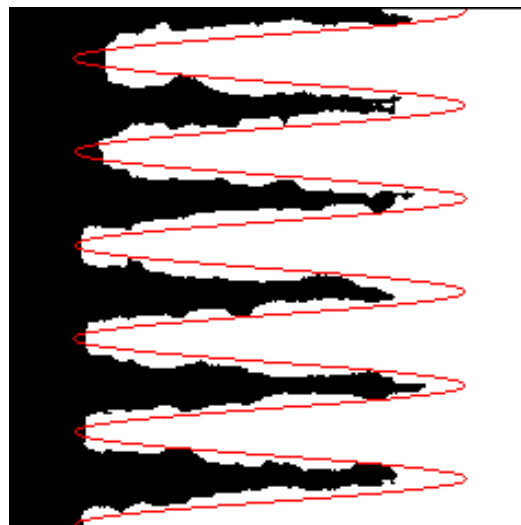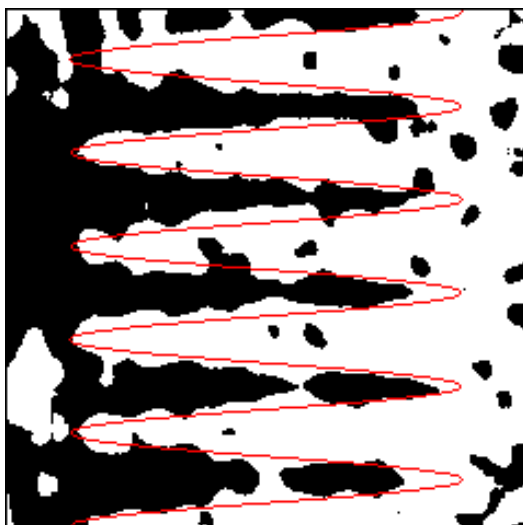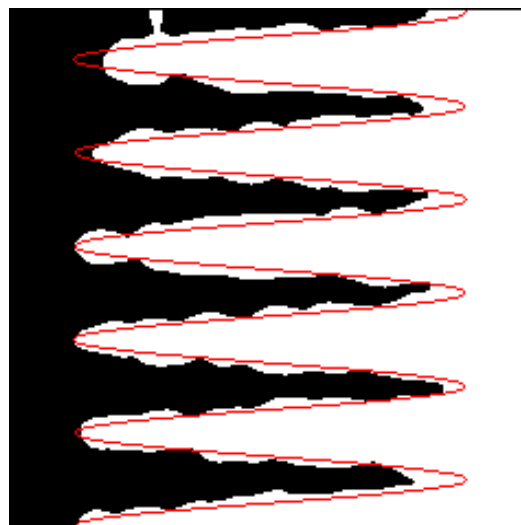Figure 5.25: Segmentation results of the bi–partite cork–wool image.

(a) *GLCP* using entropy, contrast, correlation

(b) *GLCP* using entropy and contrast

(c) *WGLCP* using entropy, contrast, correlation

(d) *WGLCP* using entropy and contrast

Figure 5.26: Segmentation results of the bi–partite cork–straw matting image.

	Cork–Wool Image		Cork–Straw Matting Image	
	Overall Accuracy (%)	**Kappa Statistic**	**Overall Accuracy (%)**	**Kappa Statistic**
Feature Set #1	88.7	0.77	83.2	0.67
Feature Set #2	89.1	0.78	85.4	0.71
Feature Set #3	91.8	0.83	81.3	0.63
Feature Set #4	92.0	0.84	89.9	0.80

Table 5.10: Performance analysis for the Brodatz bi–partite images.

significant improvement when comparing the *WGLCP* results to the *GLCP* results. Overall, feature set #4 provides the highest segmentation accuracy for this image.

Figure 5.26 shows the various segmentation results for the cork–straw matting image. It is apparent for both *GLCP* and *WGLCP* methods that correlation causes a less separable feature space. The segmentation results contain many misclassification artefacts and results in poor segmentation. When correlation is removed, both methods perform much better at segmentation and are a statistically significant improvement. Table 5.10 also outlines the increase in segmentation accuracy when comparing the *WGLCP* and *GLCP* methods. The weighted feature set is also a statistically significant improvement over the non–weighted feature set. Overall, feature set #4 provides the highest segmentation accuracy.

5.3.4 Brodatz Mosaic "Star" Image

Figure 5.27 is a Brodatz mosaic image and its corresponding ground truth image. This image is adapted from [9] and contains four distinct (and labelled) textured regions from the Brodatz photo album [4]. The textures used in this image are cork (D4), cotton canvas (D77), wool (D92) and straw matting (D55). This image is selected for testing as it has many irregularly–shaped
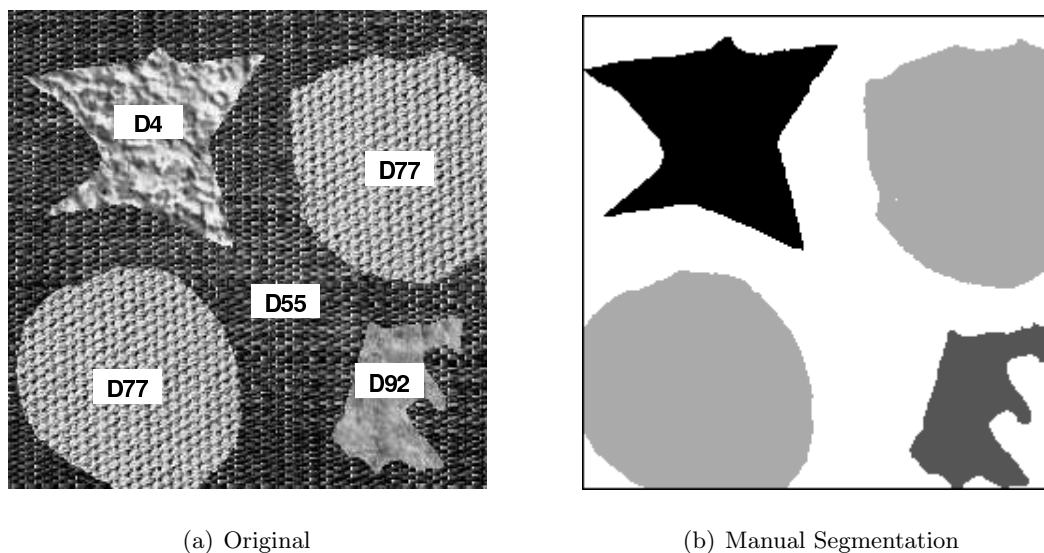
(a) Original

(b) Manual Segmentation

Figure 5.27: Brodatz mosaic "star" image. Contains 4 different textures: cork (D4), cotton canvas (D77), wool (D92) and straw matting (D55).

texture boundaries, which is indicative of SAR sea ice imagery. As well, Brodatz textures are extensively used in the literature. A window size of 19×19 is employed for feature extraction and k is set to 4 for k–means clustering.

Figure 5.28 shows the segmentation results using the four aforementioned feature sets. For both *GLCP* and *WGLCP* methods, it is very apparent that the correlation feature performs poorly. The texture boundaries between the four objects and the background are forming a separate class, which causes the cork and wool textures to be clustered together. Once the correlation feature is removed from the feature space, the boundary errors are mostly resolved. However, one can still observe that the there is some boundary misclassification around the wool texture (lower–right). The boundary transition from wool to straw matting mimics the pattern of the cork texture, resulting in boundary misclassification. As indicated in Table 5.11, the results omitting correlation for the *GLCP* and *WGLCP* methods result in and 14.3% and 12.1%
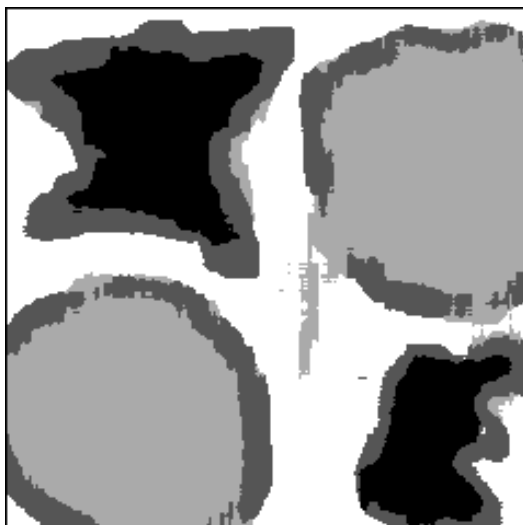
(a) *GLCP* using entropy, contrast, correlation
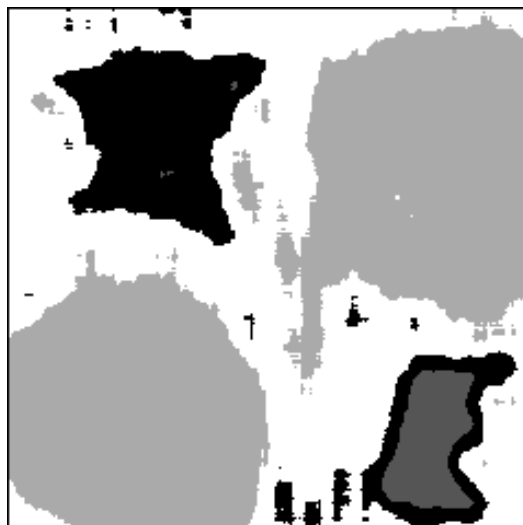
(b) *GLCP* using entropy and contrast
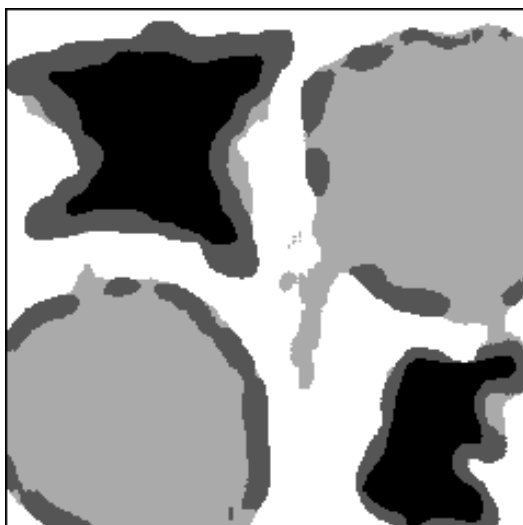
(c) *WGLCP* using entropy, contrast, correlation

(d) *WGLCP* using entropy and contrast

Figure 5.28: Segmentation results of Brodatz mosaic "star" image.

	Feature Set 1	Feature Set 2	Feature Set 3	Feature Set 4
Overall Accuracy (%)	70.9	85.2	74.2	86.3
Kappa Statistic	0.59	0.77	0.63	0.78

Table 5.11: Comparing segmentation performance of different feature sets for the Brodatz "star" image

increase in accuracy respectively. Also, these results are deemed to be a statistically significant improvement. Table 5.11 also indicates that the *WGLCP* method outperforms the *GLCP* method and that the results are statistically significant. This improvement is caused by better boundary preservation and results in better segmentation.

Chapter 6

Conclusions and Future Work

6.1   Conclusions

The topic of this thesis is to improve image texture segmentation with focus on the preservation of texture boundaries for SAR sea ice imagery. Proposed is an advancement to the *GLCP* method which has been demonstrated to preserve texture boundaries during image segmentation. This method exploits the relationship a pixel has with its closest neighbors and weights the texture measurement accordingly. These texture features are referred to as *WGLCP* (weighted *GLCP*) texture features.

A thorough comparative study between the *WGLCP* and *GLCP* feature sets is conducted in terms of boundary preservation, unsupervised segmentation ability, robustness (to increasing boundary density) and computation time. From the study, an inconsistency with the *GLCP* correlation statistic is observed, which motivated an investigative study into using this statistic for image segmentation. As the overall goal of the thesis is to improve SAR sea ice segmentation accuracy, the concepts developed from the study were applied to the image segmentation problem. From these tests, several conclusions can be formulated and are listed below:

- The *WGLCP* features are better at preserving texture boundaries. By observing the transect responses and segmentation results, the *WGLCP* features provide better boundary preservation.

- The *WGLCP* features are more robust than the *GLCP* features, where robustness is defined as segmentation performance with increasing image boundary density. As expected, the segmentation accuracy should decrease with increasing boundary density. However, it was observed that the segmentation produced from the *WGLCP* features deteriorate at a slower rate than the *GLCP* features, indicating that *WGLCP* features are more robust than the *GLCP* features.

- With respect to unsupervised SAR sea ice segmentation, the *WGLCP* features outperform the *GLCP* features. For all test images (with ground truth composites) used in this thesis, the segmentation results indicate that the *WGLCP* features are a statistical improvement over the *GLCP* features.

- The *WGLCP* method is an order of magnitude slower at computation than the *GLCP* method. Recently, there have been many advances to reduce the computation for the *GLCP* method [10, 12]. These changes resulted in computational savings of approximately one–third over using traditional methods. However, none of these advances fit naturally for when calculating the *WGLCP* features. Currently, no other investigations have been done to decrease the computational time required to calculate the *WGLCP* features. Nevertheless, with the advancements of computer hardware architecture, this computational burden will continue to be reduced.

- The *WGLCP* features are more sensitive to regional misclassifications than the *GLCP* features. This was observed from the test in Section 5.1.3 where a flaw in the image texture caused misclassification for the *WGLCP* features but not the *GLCP* features. This problem

can be alleviated by selecting a larger standard deviation for the *WGLCP* method; however, this will also result in a decrease in boundary preservation.

- In images where there is a high contrast difference between classes, the *GLCP* correlation statistical feature is not suitable for segmentation. From the tests, the *GLCP* correlation feature proves better at discriminating boundary versus non–boundary, rather than relevant objects within the image. This property makes correlation a poor choice for the segmentation of SAR sea ice imagery. Typically in SAR images, there is a high contrast difference between open water and multi–year/first year rough ice, making this statistic unsuitable.

- The *GLCP* features have a bias towards brighter, higher frequency textures in SAR sea ice imagery. By observing Fisher measures, segmentation results, feature distributions and feature space plots, there is a bias to over–classify pixels near the SAR ice–water boundary as ice.

- The preferred co–occurrence feature set for unsupervised SAR sea ice segmentation consists of the *WGLCP* features using the entropy and contrast statistics. However due to the time constraints required to calculated the *WGLCP* features, omitting the correlation statistic (use only entropy and contrast) from the *GLCP* method will provide similar results and is also recommended.

- For general image segmentation, this thesis advocates analyzing edge transects across class boundaries prior to performing segmentation. By analyzing the profile of a single feature measurement across a class boundary, the feature suitability is determined. If the feature shows an impulse–like (or under–damped) response across the class boundary, this indicates it will perform poorly at separating classes in the image. For optimal feature separability, a step–like response is desirable across the class boundary. In essence, the extra initial

time required to analyze edge transects will provide a more intelligent method in feature selection and will save time and aid in the segmentation process overall.

6.2 Future Work

To improve on image texture segmentation with focus on preserving texture boundaries, several directions could be explored:

- Explore possible methods to accelerate the *WGLCP* method. Although no optimizations are obvious at this point, efforts can be made to quicken the *GLCP* method. Some possible ideas include implementing the *WGLCP* algorithm in C code, rather than the current implementation in Matlab. As well, the algorithm could be implemented using multi–processors, multi–threading, *etc.* to accelerate the computation time.

- Combine the *WGLCP* features in a fusion methodology as explored in the literature [6]. Using these features in combination with other models can increase SAR sea ice segmentation accuracy, which is the overall goal of this thesis.

- Use the *GLCP* correlation statistical feature as an edge detector for high contrast boundaries SAR sea ice imagery. As there have been no published boundary detectors suitable for SAR sea ice imagery, an effort can be made to use the *GLCP* correlation feature to accomplish this task.

- Develop an *automated* feature selection scheme which uses edge transects to determine the preferred feature set. This method would involve taking row– and column–wise *line* scans (*i.e.* transects) across an image to detect edges/boundaries. Using this information and comparing transects, preferred features can be determined.

Appendix A

Additional Results for Increasing Boundary Set

This appendix contains images showing segmentation results for the increasing boundary set in Section 5.1.3.

Number Re-gions	Boundary Density	Producer's		User's		Overall Accu-racy	Overall Error	Kappa
		Wool	Cork	Wool	Cork			
2	0.004	0.9695	1.0000	1.0000	0.9704	0.9847	0.0153	0.9695
4	0.008	0.9458	0.9999	0.9999	0.9474	0.9725	0.0275	0.9451
9	0.016	0.9074	0.9958	0.9963	0.8965	0.9469	0.0531	0.8936
16	0.024	0.8614	0.996	0.9957	0.8695	0.9261	0.0739	0.8529
25	0.031	0.8355	0.9918	0.9916	0.8392	0.908	0.092	0.8173
36	0.039	0.8099	0.9904	0.9896	0.8207	0.8943	0.1057	0.7903
64	0.054	0.7778	0.9822	0.9812	0.7872	0.8709	0.1291	0.7449
81	0.062	0.7915	0.9704	0.971	0.7884	0.871	0.129	0.7447
144	0.084	0.7655	0.9433	0.9466	0.7539	0.8424	0.1576	0.6882
196	0.098	0.7776	0.9036	0.9189	0.7431	0.8300	0.1700	0.6606
324	0.130	0.7118	0.7949	0.8344	0.6551	0.7457	0.2543	0.4904
441	0.152	0.6099	0.6768	0.7498	0.5222	0.6358	0.3642	0.2719
576	0.172	0.5264	0.5640	0.6766	0.4073	0.5401	0.4599	0.0836

Table A.1: Segmentation analysis using *GLCP* feature set with increasing boundary

Number Re-gions	Boundary Density	Producer's		User's		Overall Accu-racy	Overall Error	Kappa
		Wool	Cork	Wool	Cork			
2	0.004	0.9749	0.9987	0.9987	0.9755	0.9868	0.0132	0.9736
4	0.008	0.9560	0.9984	0.9984	0.9569	0.9770	0.0230	0.9540
9	0.016	0.9277	0.9969	0.9973	0.9174	0.9585	0.0415	0.9168
16	0.024	0.8877	0.9972	0.9970	0.8917	0.9404	0.0596	0.8810
25	0.031	0.8633	0.9925	0.9926	0.8627	0.9233	0.0767	0.8473
36	0.039	0.8395	0.9932	0.9929	0.8447	0.9114	0.0886	0.8239
64	0.054	0.809	0.9875	0.9872	0.8122	0.8903	0.1097	0.7827
81	0.062	0.8008	0.9836	0.9838	0.7981	0.8821	0.1179	0.7666
144	0.084	0.7842	0.9637	0.9659	0.7728	0.8618	0.1382	0.7265
196	0.098	0.7777	0.9444	0.9516	0.7515	0.8470	0.1530	0.6964
324	0.130	0.7487	0.8866	0.9056	0.7083	0.8049	0.1951	0.6113
441	0.152	0.7294	0.8284	0.8709	0.6585	0.7676	0.2324	0.5323
576	0.172	0.6571	0.7648	0.8288	0.5627	0.6965	0.3035	0.3921

Table A.2: Segmentation analysis using *WGLCP* feature set with increasing boundary

(a) Original Image

(b) Ground Truth Image

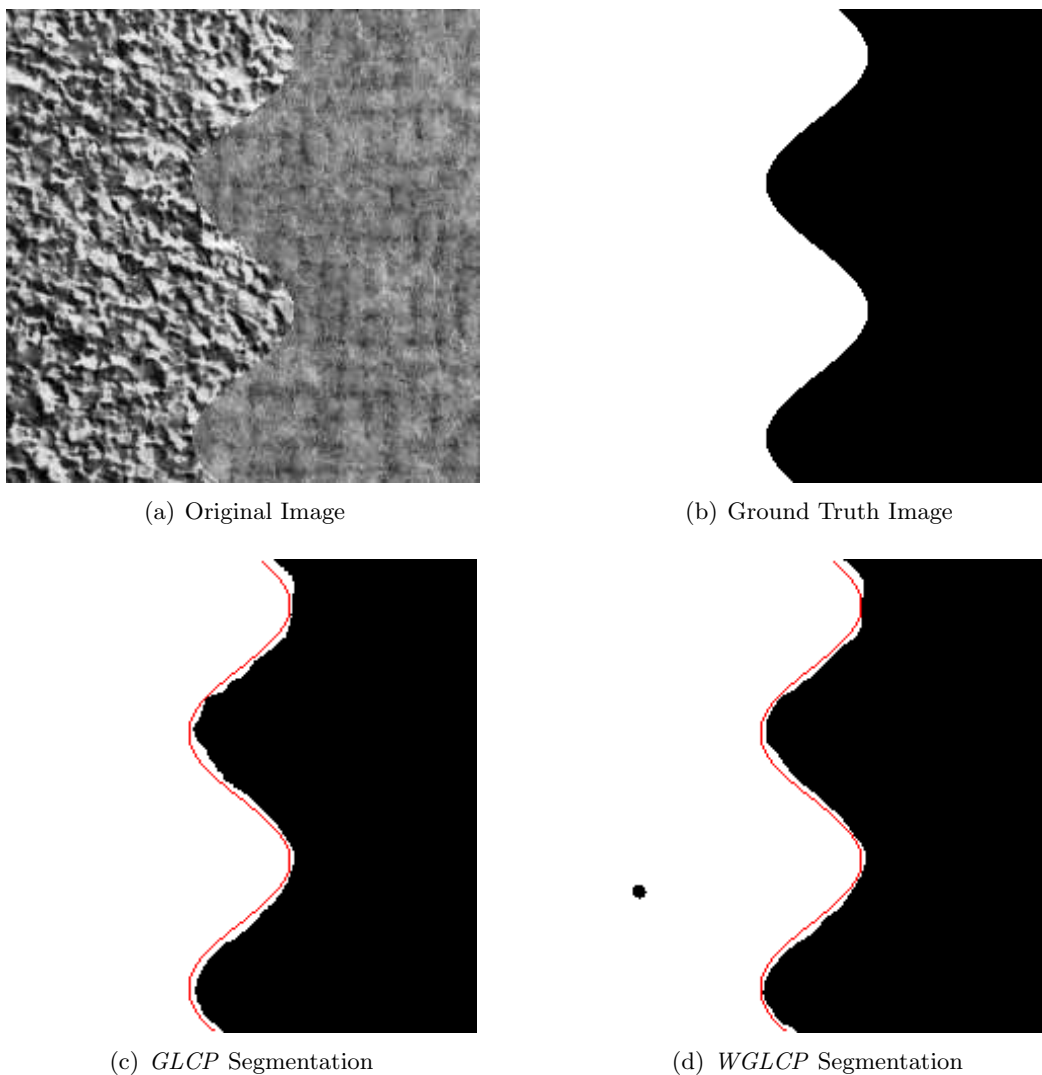(c) *GLCP* Segmentation

(d) *WGLCP* Segmentation

Figure A.1: Graphical segmentation results of the Brodatz cork–wool image. Cork is on the left–hand side, wool is on the right–hand side. There are 2 regions in this image. Included is the (a) original image, the (b) ground truth image, (c) unsupervised segmentation results using *GLCP* features, and (d) unsupervised segmentation results using *WGLCP* features.

(a) Original Image

(b) Ground Truth Image

(c) *GLCP* Segmentation

(d) *WGLCP* Segmentation

Figure A.2: Graphical segmentation results of the Brodatz cork–wool image. There are 4 regions in this image. Included is the (a) original image, the (b) ground truth image, (c) unsupervised segmentation results using *GLCP* features, and (d) unsupervised segmentation results using *WGLCP* features.
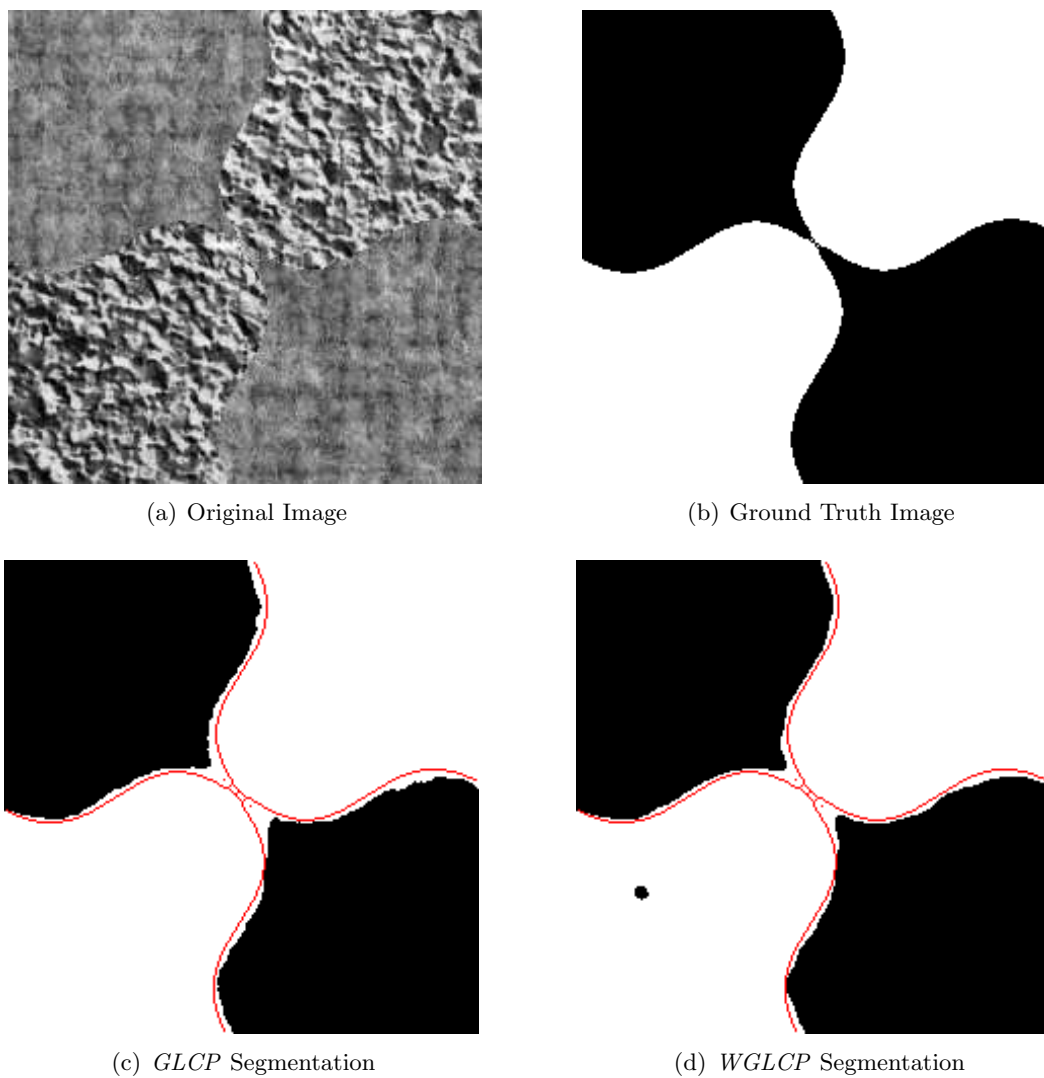
(a) Original Image

(b) Ground Truth Image

(c) *GLCP* Segmentation

(d) *WGLCP* Segmentation

Figure A.3: Graphical segmentation results of the Brodatz cork–wool image. There are 9 regions in this image. Included is the (a) original image, the (b) ground truth image, (c) unsupervised segmentation results using *GLCP* features, and (d) unsupervised segmentation results using *WGLCP* features.
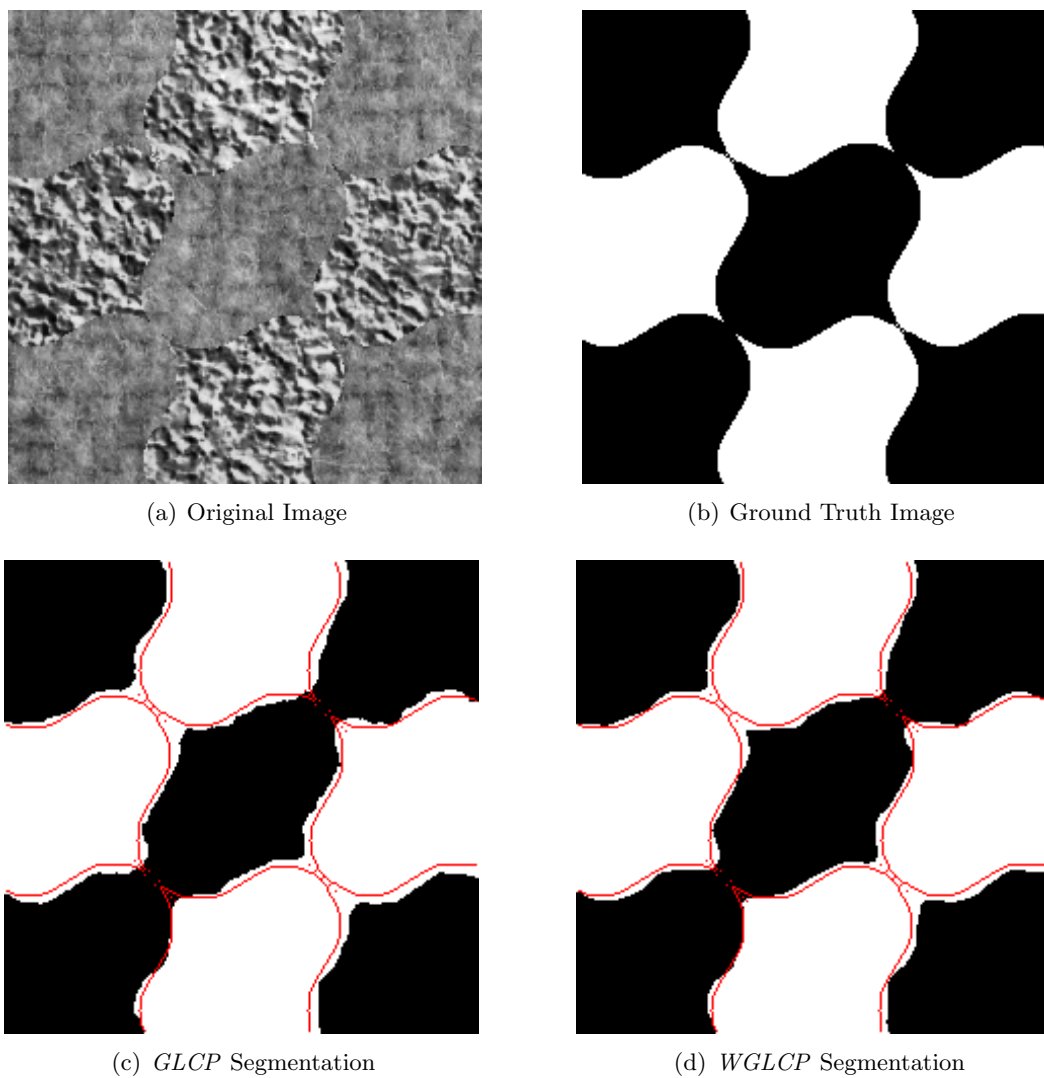
(a) Original Image

(b) Ground Truth Image

(c) *GLCP* Segmentation

(d) *WGLCP* Segmentation

Figure A.4: Graphical segmentation results of the Brodatz cork–wool image. There are 16 regions in this image. Included is the (a) original image, the (b) ground truth image, (c) unsupervised segmentation results using *GLCP* features, and (d) unsupervised segmentation results using *WGLCP* features.
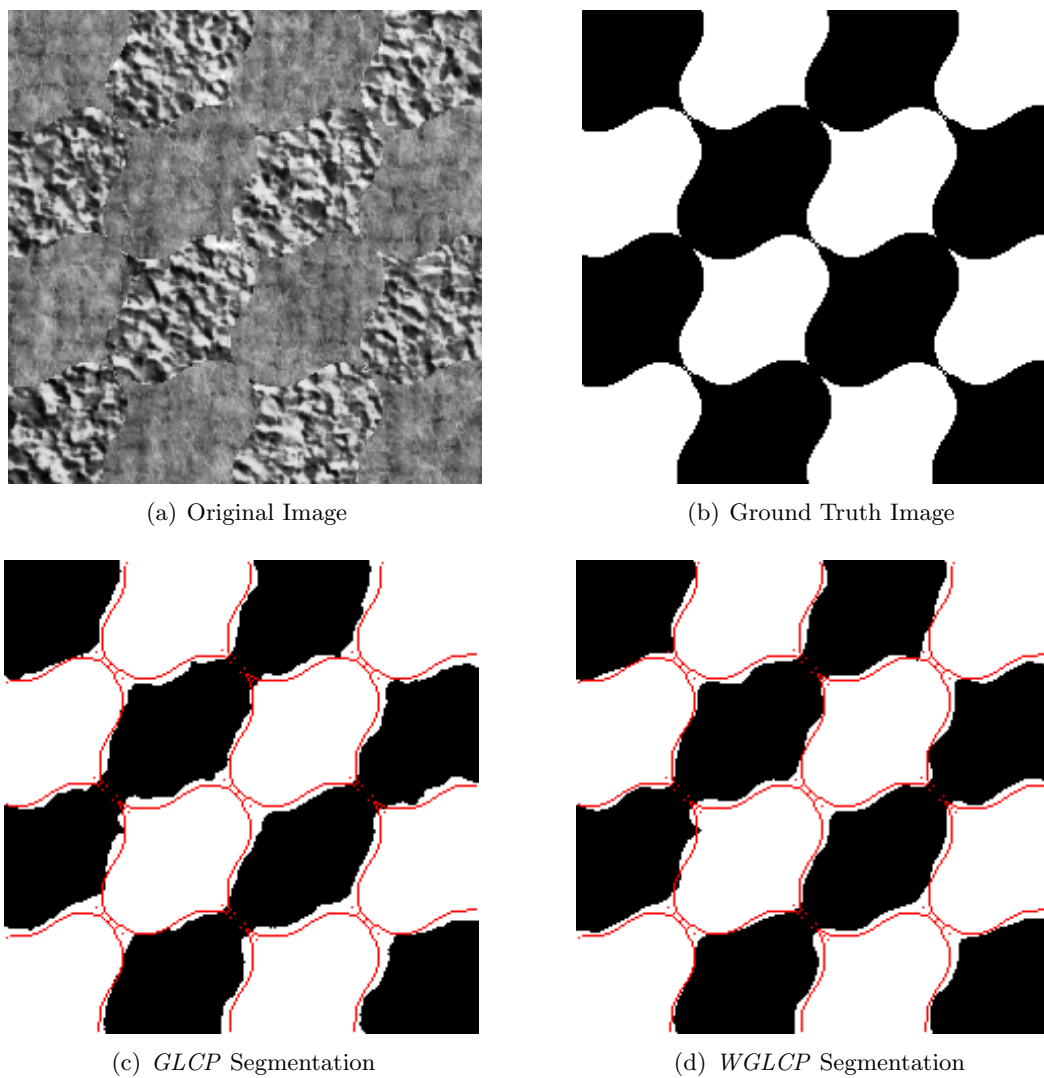
(a) Original Image

(b) Ground Truth Image

(c) *GLCP* Segmentation

(d) *WGLCP* Segmentation

Figure A.5: Graphical segmentation results of the Brodatz cork–wool image. There are 25 regions in this image. Included is the (a) original image, the (b) ground truth image, (c) unsupervised segmentation results using *GLCP* features, and (d) unsupervised segmentation results using *WGLCP* features.
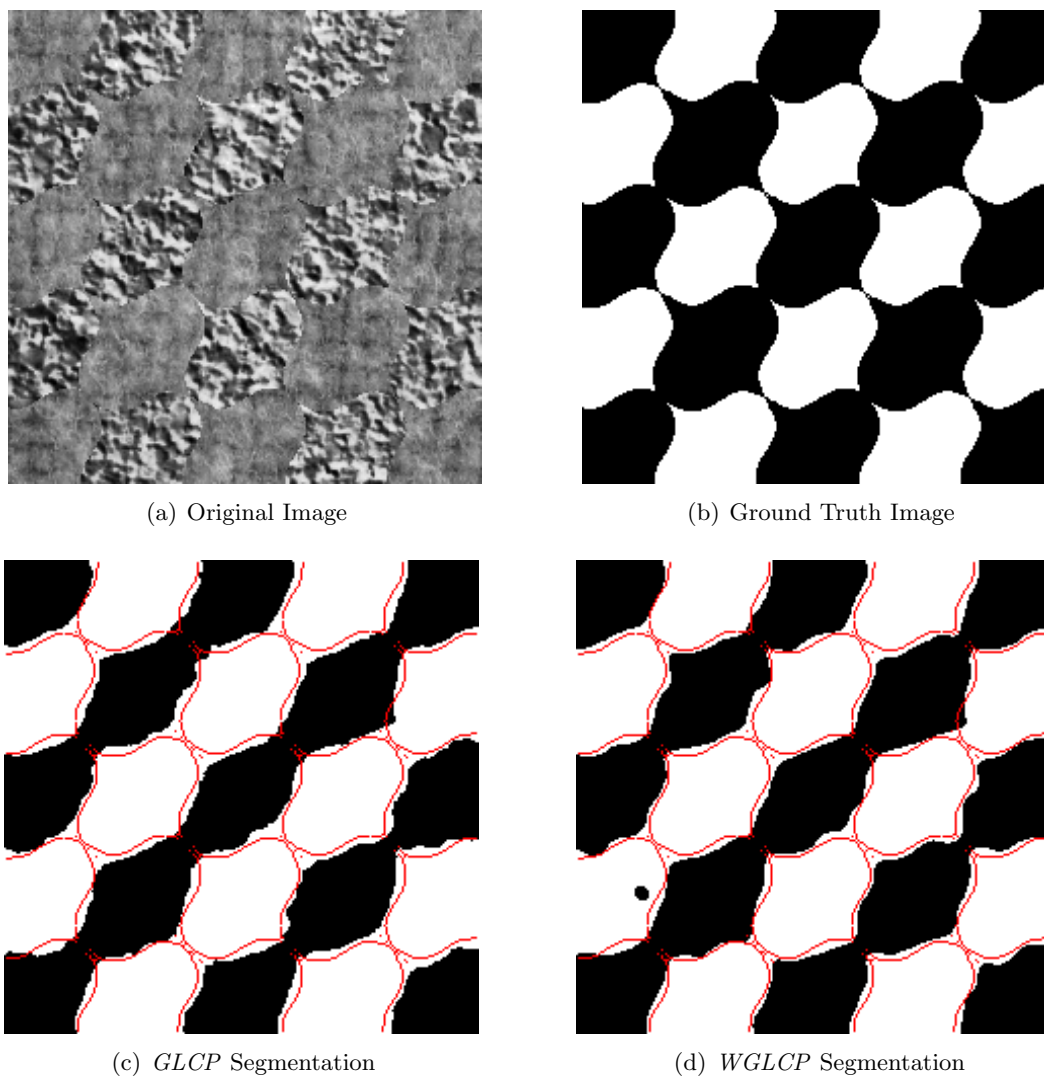
(a) Original Image

(b) Ground Truth Image

(c) *GLCP* Segmentation

(d) *WGLCP* Segmentation

Figure A.6: Graphical segmentation results of the Brodatz cork–wool image. There are 36 regions in this image. Included is the (a) original image, the (b) ground truth image, (c) unsupervised segmentation results using *GLCP* features, and (d) unsupervised segmentation results using *WGLCP* features.
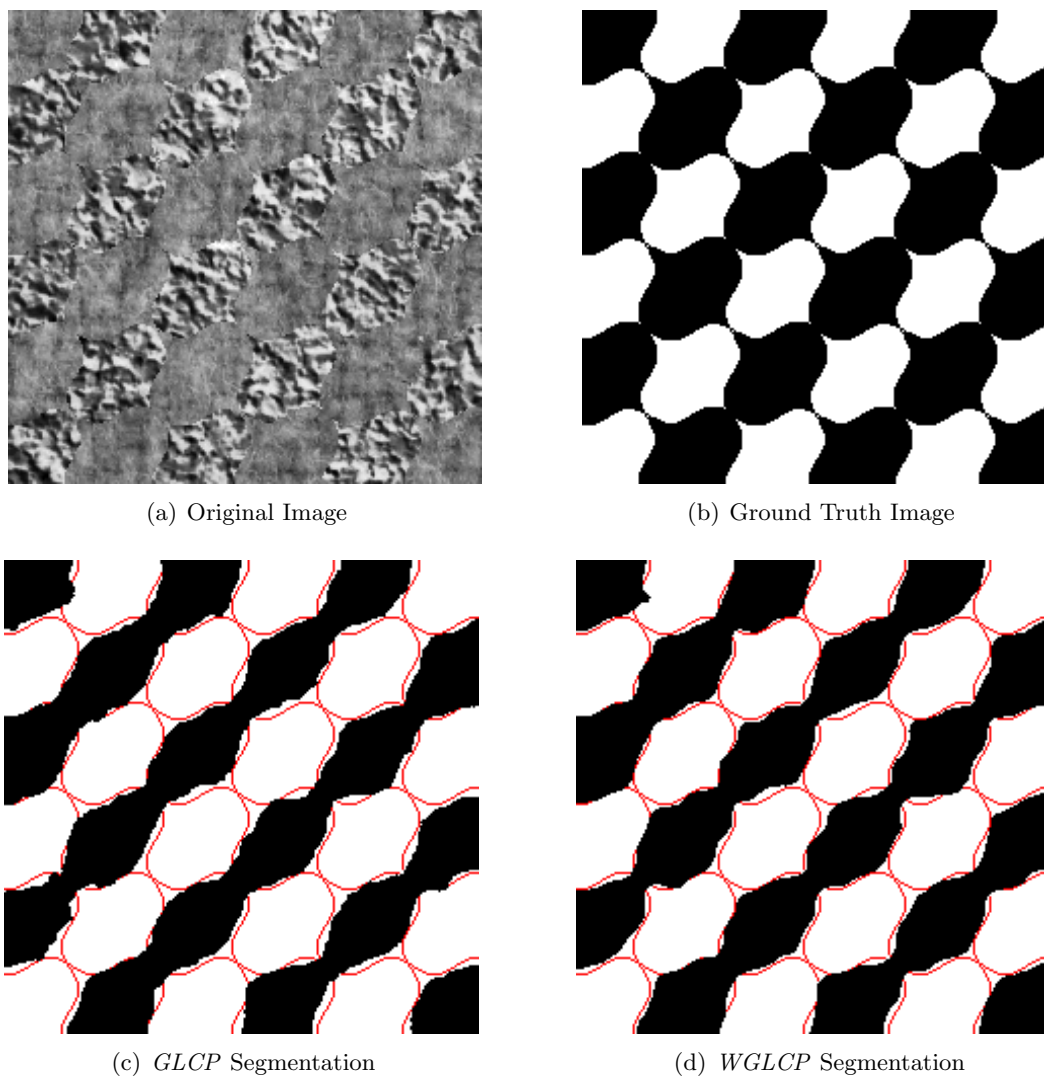
(a) Original Image

(b) Ground Truth Image

(c) *GLCP* Segmentation

(d) *WGLCP* Segmentation

Figure A.7: Graphical segmentation results of the Brodatz cork–wool image. There are 64 regions in this image. Included is the (a) original image, the (b) ground truth image, (c) unsupervised segmentation results using *GLCP* features, and (d) unsupervised segmentation results using *WGLCP* features.
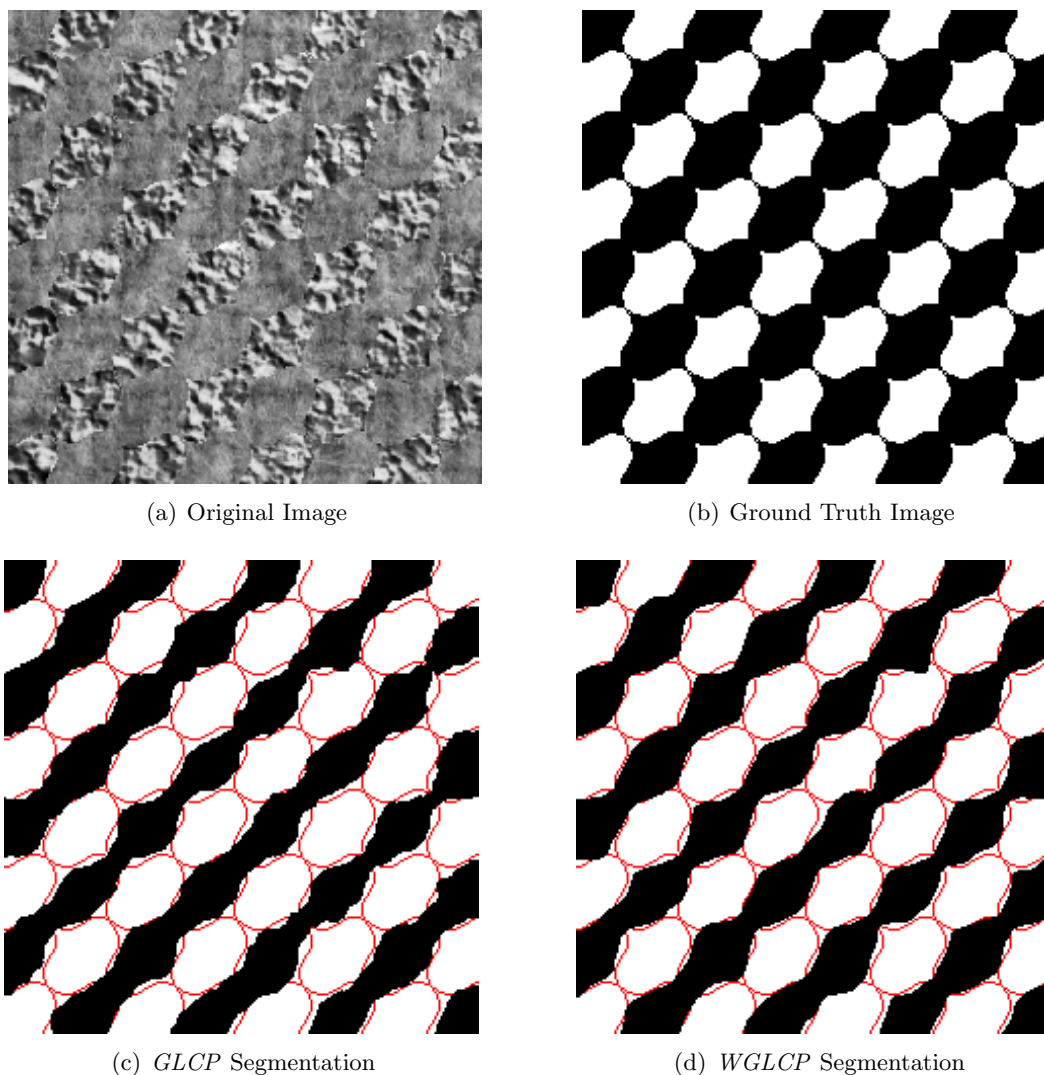
(a) Original Image

(b) Ground Truth Image

(c) *GLCP* Segmentation

(d) *WGLCP* Segmentation

Figure A.8: Graphical segmentation results of the Brodatz cork–wool image. There are 81 regions in this image. Included is the (a) original image, the (b) ground truth image, (c) unsupervised segmentation results using *GLCP* features, and (d) unsupervised segmentation results using *WGLCP* features.
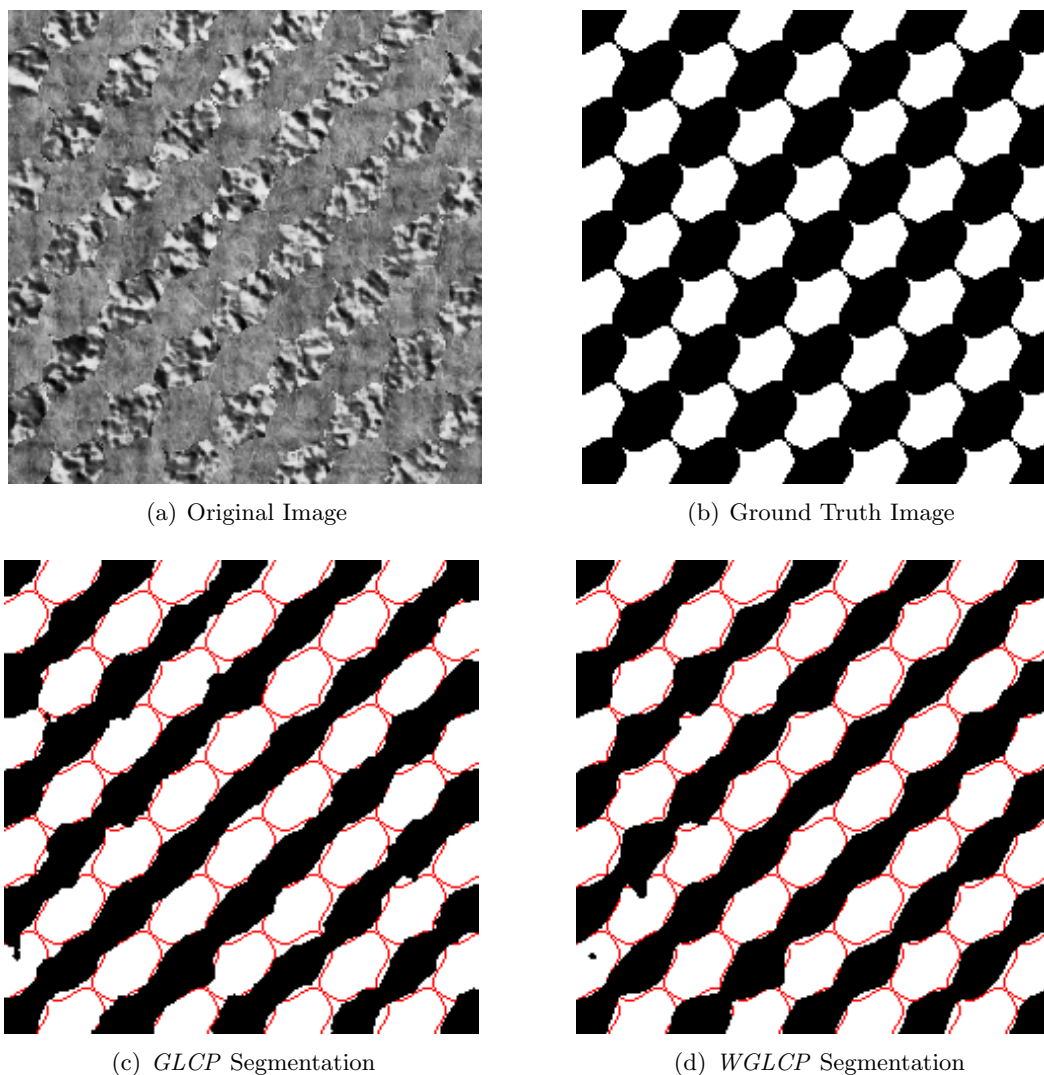
(a) Original Image

(b) Ground Truth Image

(c) *GLCP* Segmentation

(d) *WGLCP* Segmentation

Figure A.9: Graphical segmentation results of the Brodatz cork–wool image. There are 144 regions in this image. Included is the (a) original image, the (b) ground truth image, (c) unsupervised segmentation results using *GLCP* features, and (d) unsupervised segmentation results using *WGLCP* features.
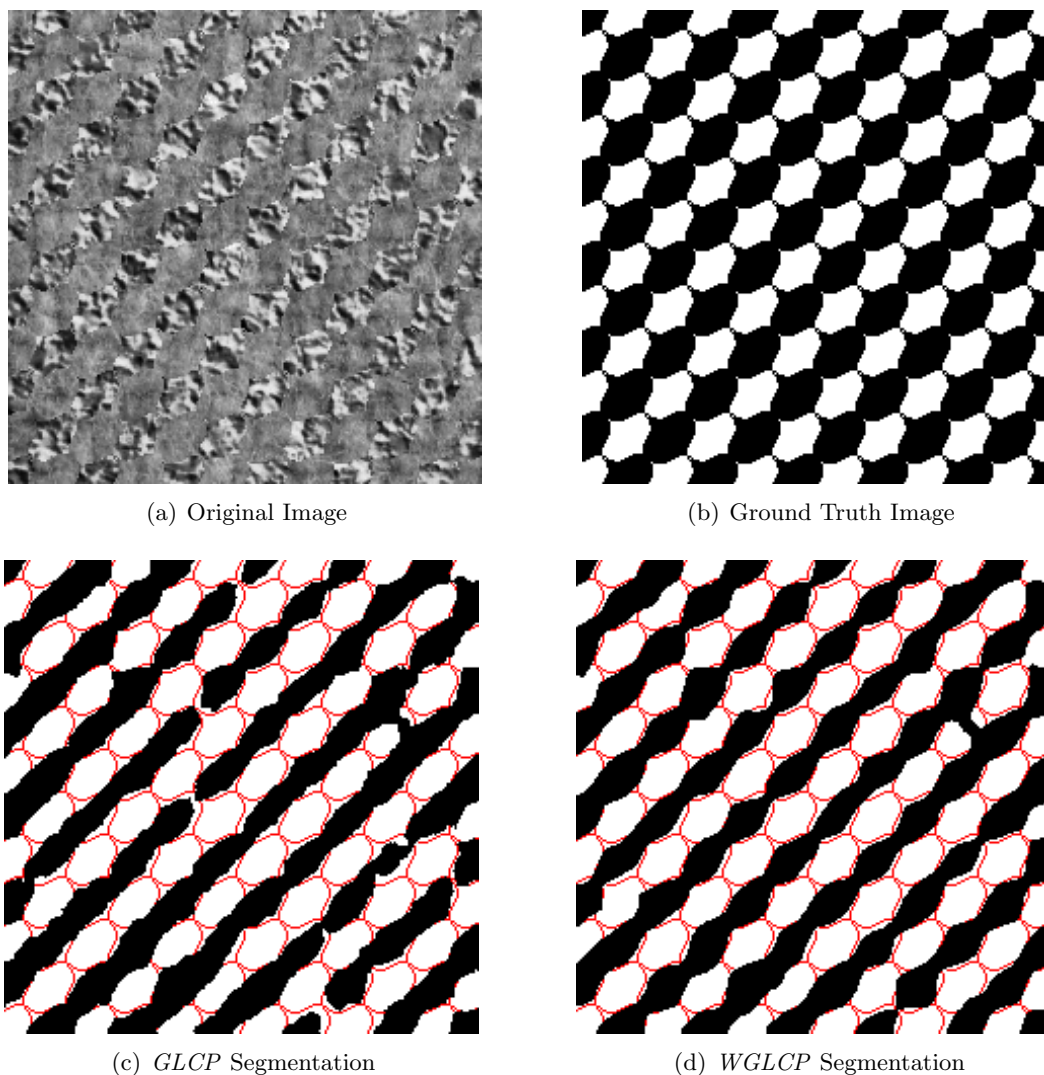
(a) Original Image

(b) Ground Truth Image

(c) *GLCP* Segmentation

(d) *WGLCP* Segmentation

Figure A.10: Graphical segmentation results of the Brodatz cork–wool image. There are 196 regions in this image. Included is the (a) original image, the (b) ground truth image, (c) unsupervised segmentation results using *GLCP* features, and (d) unsupervised segmentation results using *WGLCP* features.
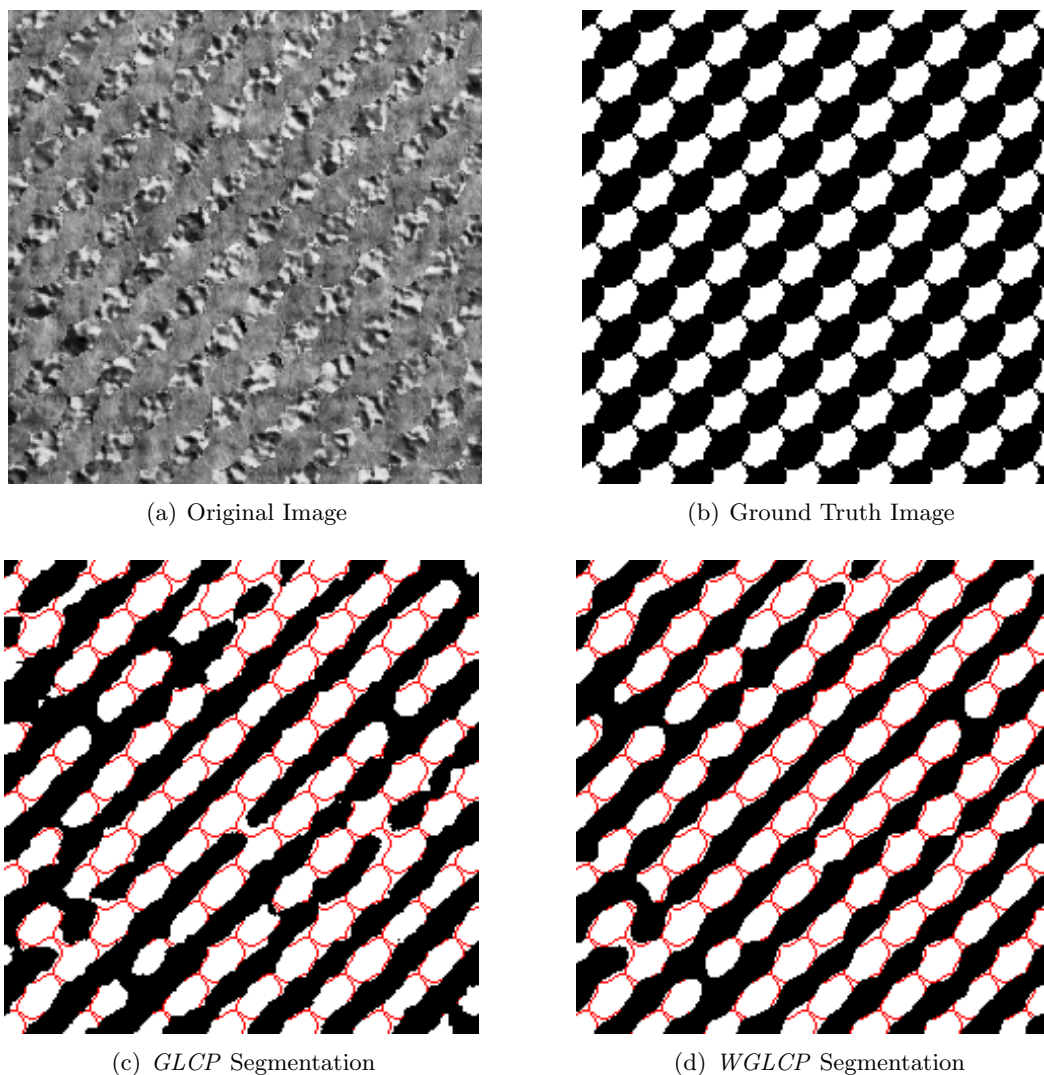
(a) Original Image

(b) Ground Truth Image

(c) *GLCP* Segmentation

(d) *WGLCP* Segmentation

Figure A.11: Graphical segmentation results of the Brodatz cork–wool image. There are 324 regions in this image. Included is the (a) original image, the (b) ground truth image, (c) unsupervised segmentation results using *GLCP* features, and (d) unsupervised segmentation results using *WGLCP* features.

(a) Original Image

(b) Ground Truth Image

(c) *GLCP* Segmentation

(d) *WGLCP* Segmentation
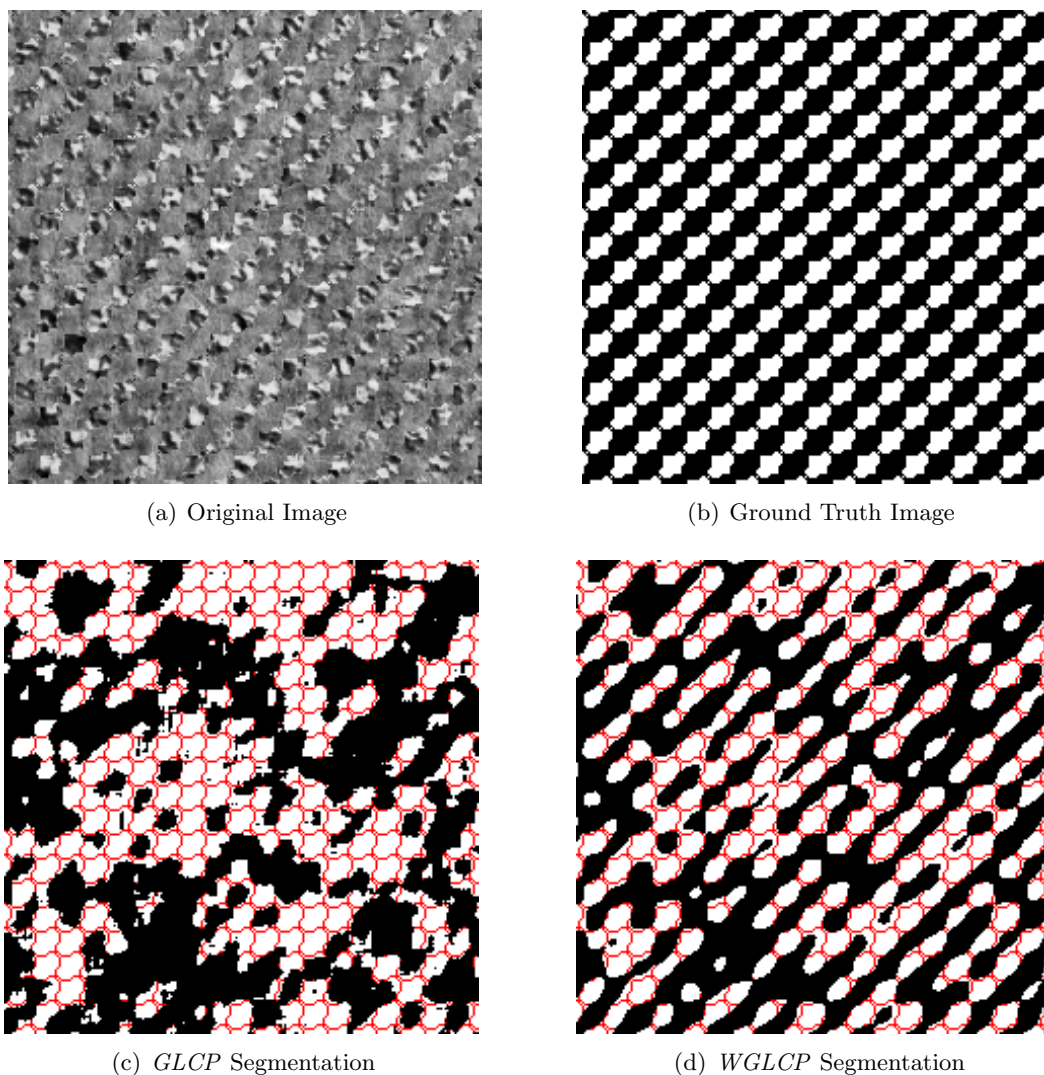
Figure A.12: Graphical segmentation results of the Brodatz cork–wool image. There are 441 regions in this image. Included is the (a) original image, the (b) ground truth image, (c) unsupervised segmentation results using *GLCP* features, and (d) unsupervised segmentation results using *WGLCP* features.
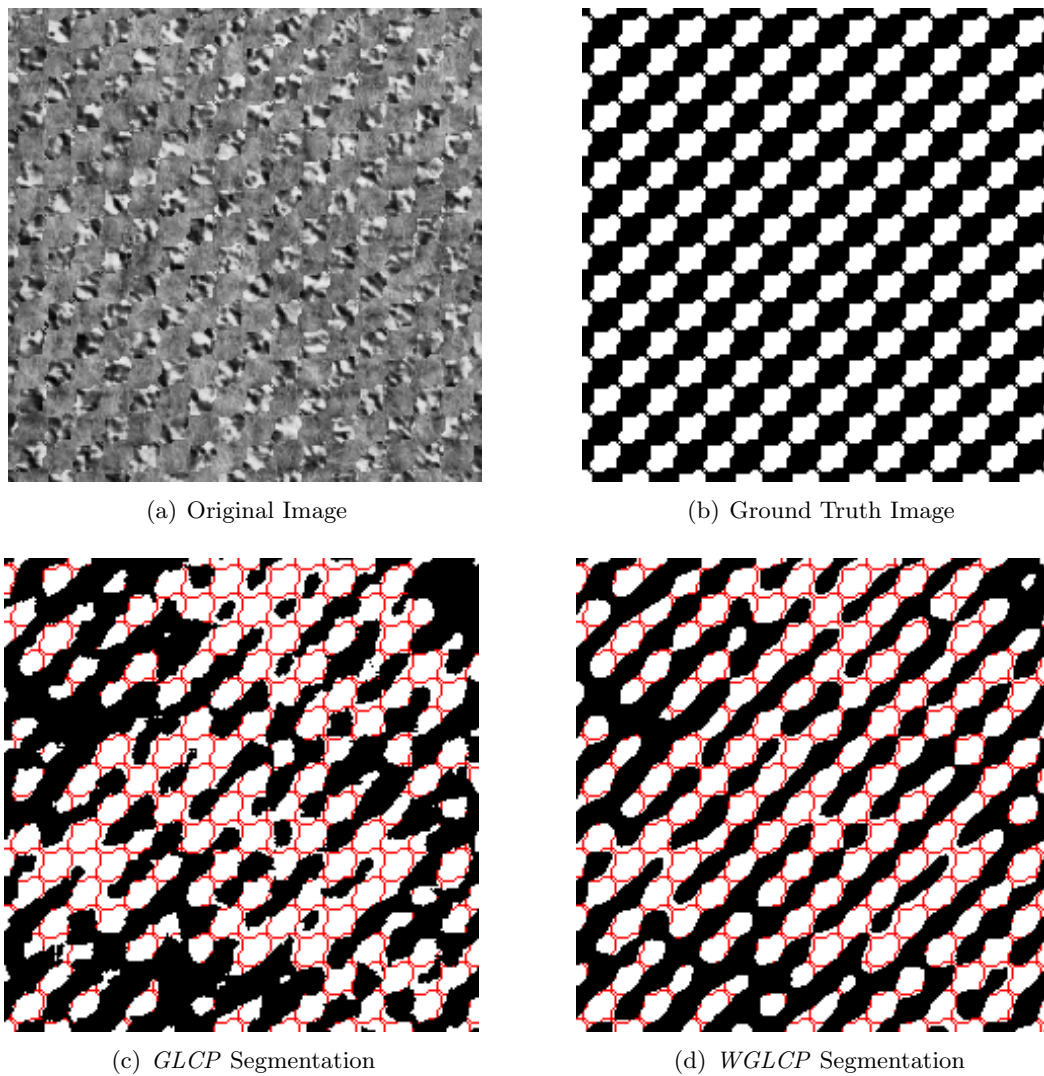
(a) Original Image

(b) Ground Truth Image

(c) *GLCP* Segmentation

(d) *WGLCP* Segmentation

Figure A.13: Graphical segmentation results of the Brodatz cork–wool image. There are 576 regions in this image. Included is the (a) original image, the (b) ground truth image, (c) unsupervised segmentation results using *GLCP* features, and (d) unsupervised segmentation results using *WGLCP* features.
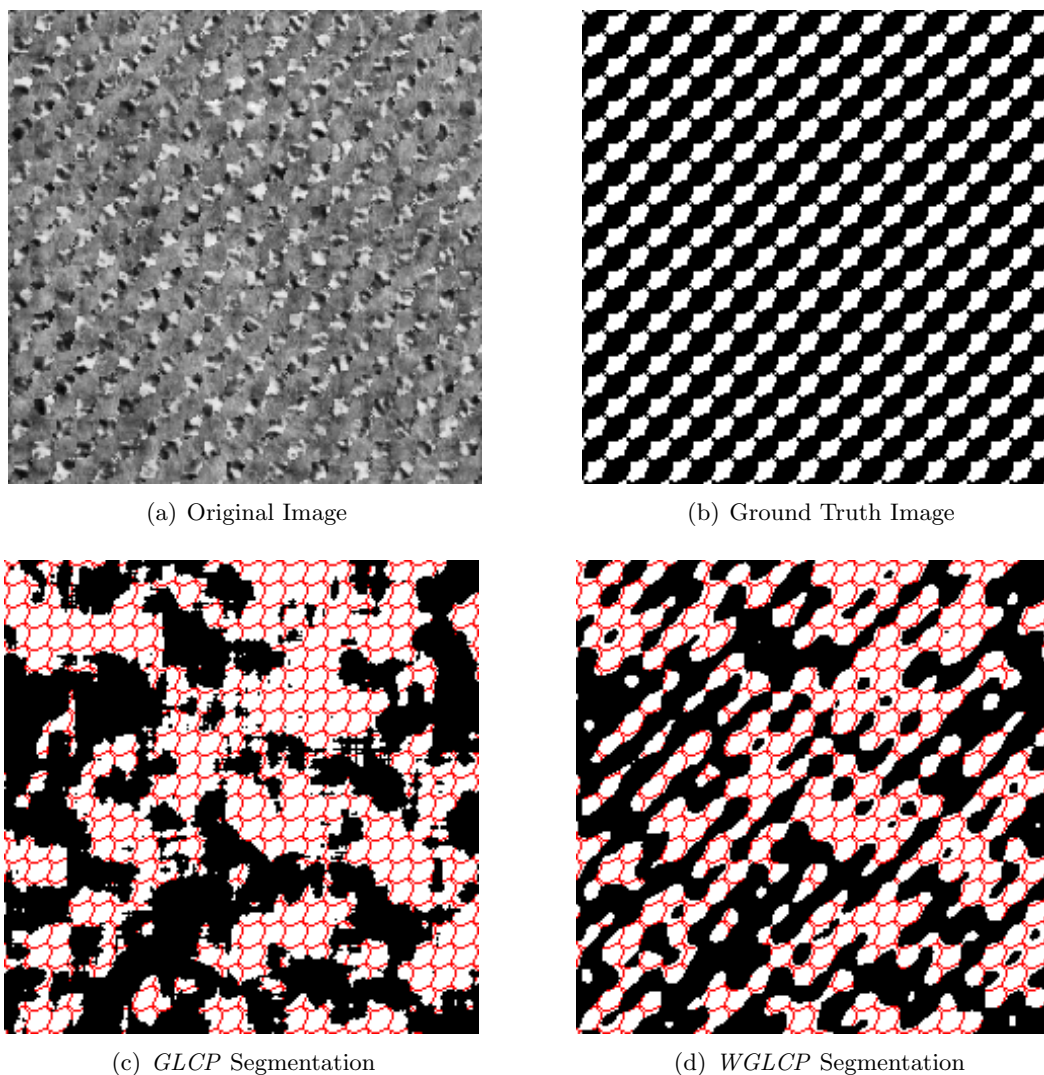
References

[1] A. Baraldi and F. Parmiggiani. An investigation of the textural characteristics associated with gray level cooccurrence matrix statistical parameters. *IEEE Trans. Geosci. Remote Sensing*, 33(2):293–303, March 1995.

[2] D. G. Barber and E. F. LeDrew. SAR sea ice discrimination using texture statistics: a multivariate approach. *Photgrammetric Engineering Engineering and Remote Sensing*, 57(4):385–395, 1991.

[3] Y. M. Bishop, S. E. Fienberg, and P. W. Holland. *Discrete Multivariate Analysis: Theory and Practise*. The MIT Press, 1977.

[4] P. Brodatz. Textures: A photographic album for artists and designers. *Dover*, 1966.

[5] D. A. Clausi. *Texture segmentation of SAR sea ice imagery*. PhD thesis, University of Waterloo, Waterloo, Ontario, Canada N2L 3G1, 1996.

[6] D. A. Clausi. Comparison and fusion of co-occurrence, Gabor, and MRF texture features for classification of SAR sea ice imagery. *Atmosphere and Oceans*, 39(4):183–194, 2001.

[7] D. A. Clausi. An analysis of co-occurrence texture statistics as a function of grey level quantization. *Can. J. Remote Sensing*, 28(1):45–62, 2002.

[8] D. A. Clausi and H. Deng. Unsupervised segmentation of texture images through optimal fusion of gabor and co-occurrence texture features. In *16th International Conference on Vision Interface (VI 03)*, pages 237–242, Halifax, NS, Canada, June 11-13 2003.

[9] D. A. Clausi and H. Deng. Design-based fusion of gabor filter and co-occurrence probability features for texture recognition. *IEEE Trans. Image Processing*, April 2004. under 2nd review.

[10] D. A. Clausi and M. E. Jernigan. A fast method to determine co-occurrence texture features. *IEEE Trans. Geosci. Remote Sensing*, 36(1):298–300, 1998.

[11] D. A. Clausi and B. Yue. Comparing cooccurrence probabilities and Markov random fields for texture analysis of SAR sea ice imagery. *IEEE Trans. Geosci. Remote Sensing*, 42(1):215–228, 2004.

[12] D. A. Clausi and Y. Zhao. Rapid extraction of image texture by co-occurrence using a hybrid data structure. *Computers and Geosciences*, 28:763–774, 2002.

[13] R. C. Dorf and R. H. Bishop. *Modern Control Systems*. Prentice Hall, 9th edition, 2001.

[14] R. O. Duda, P. E. Hart, and D. G. Stork. *Pattern Classification*. John Wiley and Sons, 2nd edition, 2001.

[15] C. Elachi. *Introduction to the Physics and Techniques of Remote Sensing*. John Wiley and Sons, 1st edition, 1987.

[16] M. Fily and A. Rothrock. Extracting sea ice data from satellite SAR imagery. *IEEE Trans. Geosci. Remote Sensing*, 6(GE-24):849–854, Nov 1986.

[17] K. Fukunaga. *Introduction to Statistical Pattern Recognition*. Academic Press, 1990.

[18] M. M. Galloway. Texture classification using grey-level run lengths. *Computer Graphics and Image Processing*, 4:172–179, 1975.

[19] R. M. Haralick, K. Shanmugam, and I. Dinstein. Textural features for image classification. *IEEE Trans. Sys. Man Cyber.*, 3(6):610–621, Nov 1973.

[20] C. A. Harlow and R. W. Conners. Theoretical comparison of texture algorithms. *IEEE Trans. Pat. Anal. Mach. Intel.*, 2(3):204–222, May 1980.

[21] F. M. Henderson and A. J. Lewis. *Principles and Applications of Imaging Radar: Manual of Remote Sensing*, volume 2. John Wiley and Sons Inc., 1998.

[22] Q. A. Holmes, D. R. Nuesch, and R. A. Shuchman. Texture analysis and real-time classification of sea-ice types using digital SAR data. *IEEE Trans. Geosci. Remote Sensing*, 22(2):113–120, 1984.

[23] J. R. Jensen. *Introductory Digital Image Processing: A Remote Sensing Perspective*. Prentice Hall Inc., 1986.

[24] B. Julesz, E. N. Gilbert, and J. D. Victor. Visual discrimination of textures with identical third-order statistics. *Biological Cybernetics*, 31:137–140, 1981.

[25] R. Kwok, E. Rignot, and B. Holt. Identification of sea ice types in spaceborne synthetic aperture radar data. *J. Geophys. Res.*, 97(C2):2391–2402, Feb 1992.

[26] M. D. Levine. *Vision in Man and Machine*. McGraw–Hill, 1985.

[27] B. B. Mandelbrot. *The Fractal Geometry of Nature*. Freeman, 1984.

[28] J.A. Nystuen and F.W. Garcia Jr. Sea ice classification using SAR backscatter statistics. *IEEE Trans. Geosci. Remote Sensing*, 30(3):50–509, 1992.

[29] A. Pentland. Fractal-based description of natural scenes. *IEEE Trans. Pattern Anal. Mach. Intell.*, 9:661–674, 1984.

[30] J. A. Richards and X. Jia. *Remote Sensing Digital Image Analysis*. Springer, 3rd edition, 1999.

[31] F. F. Sabins. *Remote Sensing Principles and Interpretation*. W. H. Freeman and Company, 1987.

[32] M. E. Shokr. On sea-ice texture characterization from SAR images. *IEEE Trans. Geosci. Remote Sensing*, 28(4):737–740, July 1990.

[33] M. E. Shokr. Evaluation of second-order texture parameters for sea ice classification from radar images. *J. Geophysical Research*, 96(C6):625–640, 1991.

[34] Web site of CRYSYS: CRYosphere SYStem in Canada. Why study the cryosphere? *http://www.msc.ec.gc.ca/crysys/education/crysys–education–e.cfm*, Access Date: April 05/05 2003.

[35] L. K. Soh and C. Tsatsoulis. Texture analysis of SAR sea ice imagery using gray level co-occurence matrices. *IEEE Trans. Geosci. Remote Sensing*, 37(2):780–794, March 1999.

[36] M. Tuceryan and A. K. Jain. Texture segmentation using Voronoi polygons. *IEEE Trans. Pattern Anal. Mach. Intell*, 12:211–216, 1990.

[37] M. Tuceryan and A. K. Jain. *Handbook of Pattern Recognition and Computer Vision, Chapter 2: Texture Analysis*. Singapore: World Scientific, 1993.

[38] J. S. Weszka, C. R. Dyer, and A. Rosenfeld. A comparitive study of texture measures for terrain classification. *IEEE Trans. Sys. Man. Cyber.*, 6(4):269–285, 1976.

[39] J. J. Yackel, D. G. Barber, and J. M. Hanesiak. Melt ponds on sea ice in the Canadian Archipelago. *Journal of Geophysical Research*, 105(C9):22049–22060, September 2000.

[40] B. Yue. SAR sea ice recognition using texture methods. Masters thesis, University of Waterloo, Waterloo, Ontario, Canada N2L 3G1, 2001.